Instituut voor
Kern- en Stralingsfysica
Departement Natuurkunde en Sterrenkunde
Faculteit Wetenschappen

KATHOLIEKE UNIVERSITEIT
LEUVEN

Nuclear g-factors of neutron rich $^{31-34}$Al and ^{35}Si: probes for changing shell structure.

Promotor:
Prof. Dr. G. Neyens

Proefschrift ingediend tot
het behalen van de graad van
doctor in de wetenschappen
door

Pieter Himpe

2006

– Dankwoord –

Men zegt wel eens dat het dankwoord vaak het enige deel van een doctoraatsthesis is dat men leest, zeker indien men geen specialist is in het onderzochte onderwerp. De tekst die dus nu komt, moet zeer goed, speels, origineel,... zijn en ik mag daarbij niemand vergeten. Hm, alleen de gedachte al om zoiets uit mijn mouw te schudden, doet mijn hartslag stijgen en zweetproductie verhogen.

Daarnaast zijn er op een doctoraatsverdediging geregeld mensen aanwezig die naar iets op zoek zijn om zich te vermaken, want ze vinden de uiteenzetting te moeilijk, of niet interessant, of ... Ik neem dit niemand kwalijk, ik ben ook zo een aantal keer 'fysisch maar niet psychisch' aanwezig geweest op een lezing.

Dus, ik dacht, ik ga 2 vliegen in 1 klap slaan. Ik maak een origineel dankwoord en ik geef de mogelijkheid aan de aanwezigen om zich in stilte bezig te houden: op de volgende bladzijde vindt u een raster waarin u alle (groeps)namen van de mensen die ik wil bedanken moet zetten. Veel plezier!

Toch vind ik dat ik nog 3 mensen extra in de bloemetjes moet zetten voor hun toewijding, elk op hun gebied. Gerda zou ik willen bedanken voor de kans die ik heb gekregen om op dit onderwerp een doctoraat te maken. Bedankt om in mij het potentiëel te zien om doctor te worden. Mijn zus bedank ik voor de gezellige babbels die me vaak terug tot de realiteit lieten komen. Maar voornamelijk mijn moeder zou ik willen bedanken voor 1001 dingen, waaronder al haar zorgen, toewijding en liefde voor mij. Bedankt moe voor alles!

Onderzoek gefinancieerd met een specialisatiebeurs van het Instituut voor Aanmoediging van Innovatie door Wetenschap en Technologie in Vlaanderen (IWT-Vlaanderen).

GEORGI – ELECTRONICA – RIET – CLAUDE
ZUS – PCP – CHRISTELLE – CAROLINE
IOLANDA – MAGDA – DEYAN – MECHANICA
JEANMICHEL – DANA – FRANCOIS – KETEL
NELE – STEPHEN – VEERLE – MARIEKE
GERDA – JOSEE – MOE – VA – KATIA –SALLY
ROBERT – INGE – JOHAN - STIJN

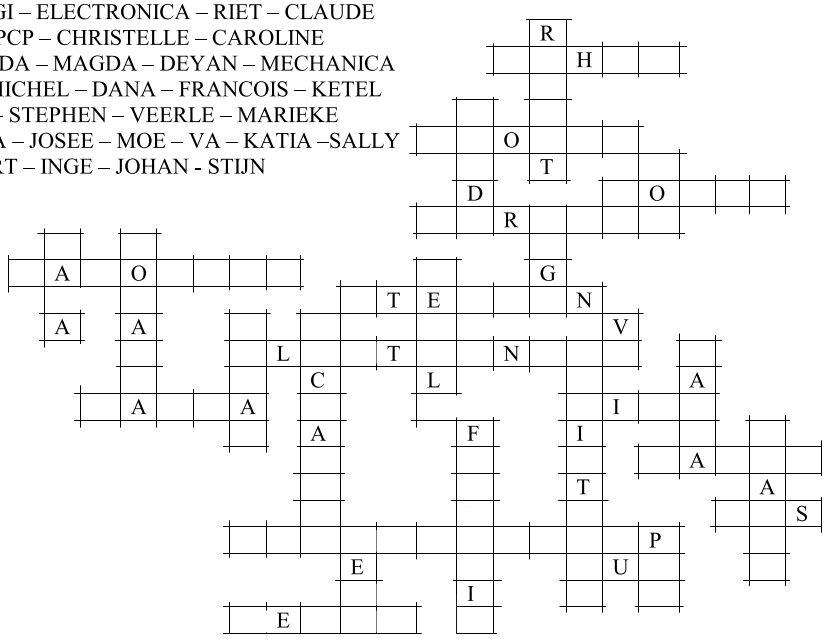

Contents

Chapter 1

Introduction

Gravity, the electromagnetic force, the weak force and the strong force are the four fundamental forces in nature. This work concentrates on experiments that aim to investigate properties of the strong force, which is responsible for the binding protons and neutrons together in the atomic nucleus. In contrast to for instance gravity, no exact explicit mathematical form for the nuclear force has been found up to now.

Working with models, such as the 'ideal gas theory' and 'the atomic shell model' is one way to solve this problem. A model is defined as a hypothetical description of a complex entity or process. Thus certain hypotheses are posed in trying to explain a certain feature, behavior, ... A good model balances between being general (only having a few restrictions and hypotheses) and still being treatable (having a few, easy to change and physically interpretable parameters). A model is often developed in order to explain some already known data. A serious test for the model is then to predict the behavior of an observable if a certain parameter is changed. In this way the reliability and generality can be tested.

Also in nuclear physics certain models each with their own restrictions are posed and tested. One of them is the nuclear shell model (NSM), introduced in the fifties and described in the first chapter of this thesis. In the NSM, the shells are filled with nucleons in order of increasing energy, consistent with the requirement of the Pauli principle (=only one particle can take the place of one quantum state). In a natural way, certain numbers, called 'magic numbers' arise for which a major shell is full. This induces certain physical properties: large two-neutron separation energy, high energy of the first excited state,...

The parameters for this model were originally chosen such that the nuclear physics properties known in the fifties could be explained. More than half a century later, the model is still used, but problems arise when trying to explain new data with the old parameters. One of the regions on the nuclear chart where the original or standard nuclear shell model (SNSM) seems to fail is the area of Z = 9-12 nuclei around N = 20. According to the SNSM N = 20 is a magic number. But from measurements of nuclear properties such as mass, spin, g-factors and quadrupole moments this was contradicted for certain Mg (Z = 12) and Na (Z = 11) isotopes. In order to explain these findings, sub-shells above N = 20 need to be taken into account, indicating that N = 20 is not a magic number for these nuclei. The region of the nuclear chart around N = 20 for which the ground state properties can only be explained when taking into account excitations to the shells above N = 20, is called the island of inversion. Even 30 years after the first abnormality was observed, the borders of this island of inversion can't be pinned down and several theoretical models predict the borders differently. At present, it is clear that some Ne (Z=10), Na (Z=11) and Mg (Z=12) isotopes do belong to the island, while no evidence is found that the ground state of any Si (Z=14) isotope is drastically influenced by higher lying sub-shells. The Al (Z=13) isotopes are in between these two regions and thus form a very interesting case, as will be explained in Chapter 2.

A very precise way of determining the components of the ground state wave function, is by measuring the magnetic moment, as explained in the third chapter of this thesis work. The g-factor, which, through the spin, is related to the magnetic moment, is extremely sensitive to

the shell-occupancy of the valence nucleon(s). This makes the g-factor a unique tool to probe the borders of the island of inversion. The results of the g-factor measurements of the ground state of ^{31,32,33,34}Al and ^{35}Si are extensively described in Chapter 5.

A necessary condition to measure g-factors is the presence of 'polarisation' in the observed ensemble of nuclei. Polarisation, a special orientation of the spin substates, can be obtained in different ways. In the fourth chapter, two mechanisms are described to successfully produce and maintain polarisation.

By measuring g-factors of Al nuclei in this region, the work described in this thesis aims to get indications for components in the ground state wave function of (unexpected) excitations to higher lying sub-shells at the edge of the island of inversion. In this way we should understand better how to change or tune the SNSM to fit these and other new and old experimental results in this region of the nuclear chart. This discussion is held in the last chapter.

Chapter 2

The Nuclear Shell Model

In this chapter we will first explain the basic ideas of the extreme independent single particle model. This simple model only works nicely for nuclei with one single nucleon outside a closed major shell. That is why the more general multiparticle nuclear shell model is introduced. Comparison between theory and experiment for several regions of the nuclear chart close to the line of stability, suggests this model to explain nuclear properties of certain nuclei in a correct way. Going away from the line of stability and from major shell closures, we will show some discrepancies and discuss the importance of the research of this work. Minor changes of the standard nuclear shell model are needed to explain these aberrations. Some of these theoretical developments are dealt with in this chapter as well.

2.1 The independent single particle model

We first start with a deliberately oversimplified shell model, but one that is mathematically tractable and rich in physical insight. That theory (the independent single particle model) is fairly successful in accounting for at least a few nuclear properties of some nuclei. Later on we can then improve it by adding additional terms and come to the more general nuclear shell model.

Atomic theory based on the shell model has provided remarkable clarification of the complicated details of atomic structure. In the atomic

shell model, the shells are filled with electrons in order of increasing energy, consistent with the requirement of the Pauli principle. When we do so, we obtain an inert core of filled shells and some number of valence electrons. The model then assumes that the atomic properties are determined primarily by the valence electrons. Nuclear physicists therefore attempted to use a similar theory to attack the problem of nuclear structure, in the hope of similar success in clarifying the properties of nuclei.

When we try to carry this model over to nuclear realm, we immediately encounter two objections:

1. In the case of atoms, the potential is supplied by an external agent, the Coulomb field of the nucleus. From this potential, the Schrödinger equation can be solved, resulting in the energies of the shells into which the electrons are placed. In the nucleus, there is no such external agent, the nucleons move in a potential that they create themselves.

The existence of a nuclear potential is dealt with by the fundamental assumption of the shell model: the motion of a single nucleon is governed by a potential caused by all other nucleons. If we treat each individual nucleon as moving in such a potential, we can allow the nucleons in turn to occupy the energy levels of a series of sub-shells, determined by this potential.

2. Electrons can move in spatial orbits relatively free of collisions with other electrons. Since the nucleus is of the order of 10.000 times smaller than the radii of the orbits the electrons move in and $m_{nucleon} \sim 2000 m_{electron}$, the density of the nucleus is $10^{15} g/cm^3$. How can we regard the nucleons as moving in well defined orbits when a single nucleon can make many collisions during each orbit, due to this large density?

This 'collision problem' is solved by the Pauli principle. When nucleons near the bottom of the potential well collide, they will transfer energy to one another. Because all levels are filled up to the level of the valence nucleons, such a nucleon can only gain energy by moving to a valence level, which requires more energy than the nucleons are likely to transfer in such collisions.

Once these problems are solved, the next step in developing a nuclear shell model is the choice of the potential. The harmonic oscillator potential is particularly popular in nuclear physics because it provides a remarkably good first approximate solution to many nuclear problems and it is easy to handle mathematically.

Because only the three smallest experimental magic numbers (2, 8 and 20) are in agreement with the results from the harmonic oscillator potential, some modifications are needed. An extra l^2 term takes into account the short range character of the strong force. A last modification needed is an extra spin-orbit component proportional to $\vec{\mathbf{l}}.\vec{\mathbf{s}}$, because the force felt by a given particle differs according to whether its spin and orbital angular momenta are aligned parallel or antiparallel. The single-particle energies resulting from this potential are shown on the right hand side of Figure 2.1

Notice that for a harmonic oscillator potential, the energies go as $E\sim 1/d^2$ where d is the size of the well. For heavier nuclei, the well will be broader, the wavelength of the lowest energy wave longer, thus the energy lower. In the shell model, we will therefore have approximately, $E_{sub-shell}\sim 1/r^2\sim A^{-2/3}$. This generic scaling will be slightly different for low and high angular momentum orbits since the particles orbit at different radii. Figure 2.2 shows the change of orbit energies as a function of the mass number for several sub-shells.

Starting from this figure we can explain the 'extreme independent particle model'. Its basic assumption is that all nucleons but one are paired, and the nuclear properties arise solely from the motion of the single unpaired nucleon. When, for instance, energy is added to the nucleus, the core remains inert and the odd particle absorbs the energy and moves to higher shell-model levels.

This model works good for nuclei with a magic proton (neutron) number and one neutron (proton) particle or hole outside a closed shell. An example is the level structure of ^{41}Ca, shown in Figure 2.3.

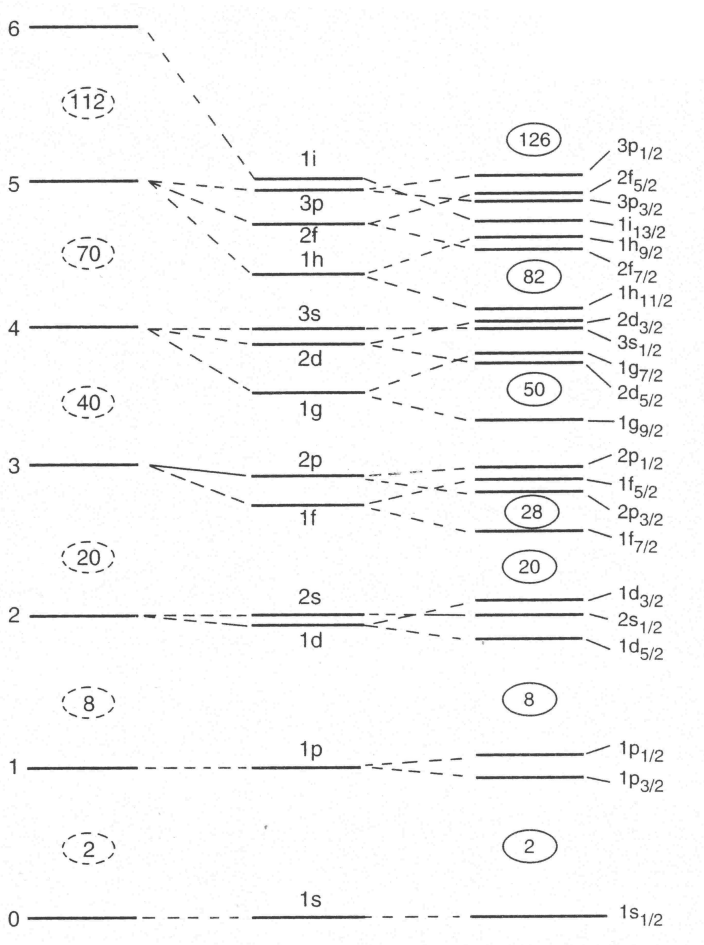

Figure 2.1: Energy levels using the harmonic oscillator potential (left), including l^2-term (middle) and including spin-orbit interaction (right). Picture taken from [1]

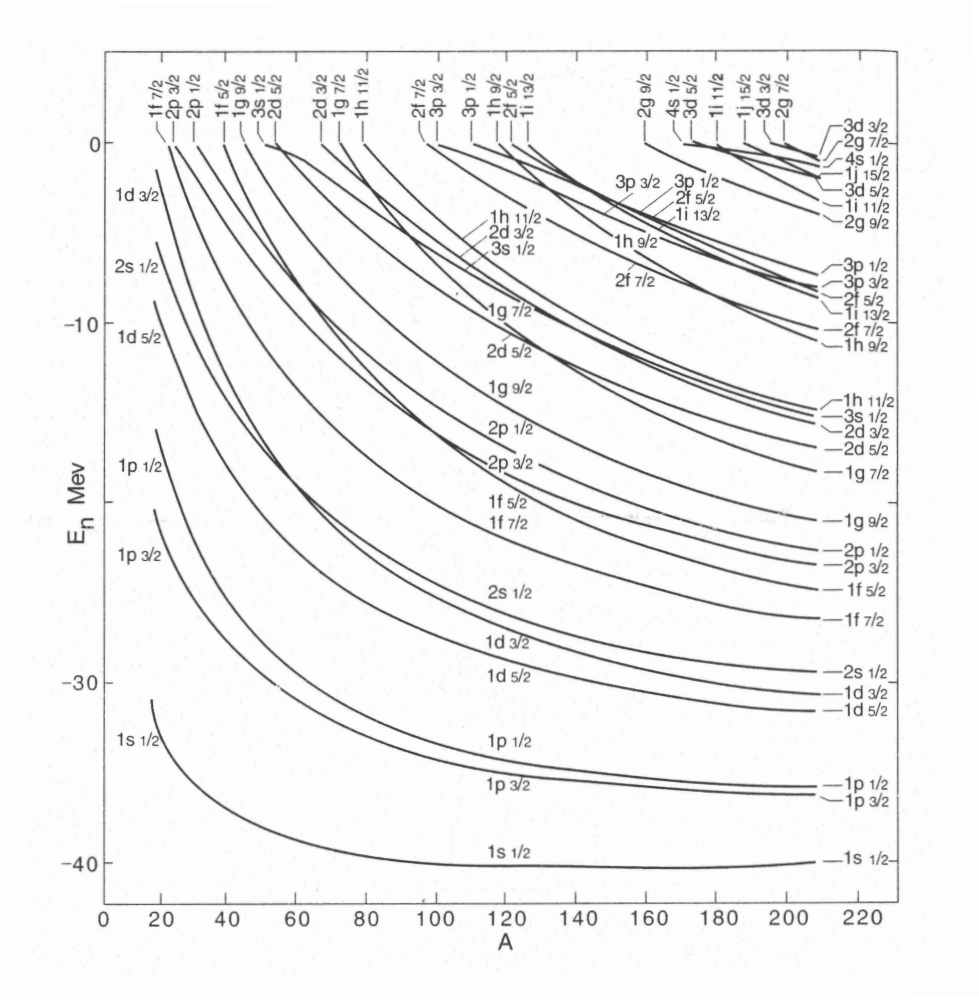

Figure 2.2: Changes of single particle energies with nucleon number, reflecting the dependence of the energies of confined particles on the size of the containment volume. Picture taken from [2]

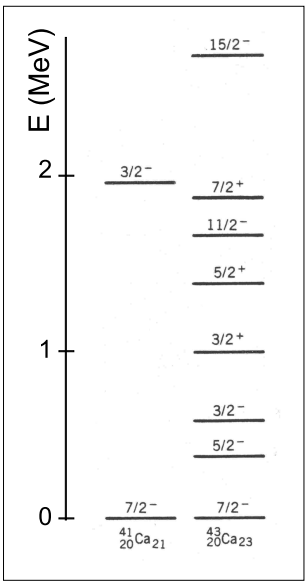

Figure 2.3: Experimental low energy levels of ^{41}Ca and ^{43}Ca

The spin and parity of the ground state are $7/2^-$ as expected for the $1f_{7/2}$ shell-model state of the 21^{th} neutron. The $3/2^-$ excited state around 2 MeV corresponds to the $2p_{3/2}$ level.

Thus far, the extreme independent single particle model can explain some features of the ^{41}Ca nucleus, but it can not reproduce the much richer spectrum of states in ^{43}Ca, which should have the same level scheme as ^{41}Ca according to this model. In order to understand these levels, one has to extend the extreme independent single particle model to a more complicated but still transparent more general shell model: the many particle nuclear shell model.

2.2 The many particle nuclear shell model

In the many particle nuclear shell model, more than just the last unpaired nucleon is used to describe the properties of nuclei. In the single particle model, all nucleon pairs with spin I are supposed to couple to a 0^+ state, but in reality they can couple to any integer value between 0 and 2I. Taking this into account, together with some residual interaction between the nucleons, a much richer spectrum is proposed theoretically for ^{43}Ca as explained below.

We use the shorthand notation $(f_{7/2})^n$ to indicate a configuration with n particles in the $f_{7/2}$ shell, and we consider the possible resultant values for I for the configuration $(f_{7/2})^3$ in order to explain the ^{43}Ca spectrum. Due to the Pauli principle only I = 15/2, 11/2, 9/2, 7/2, 5/2 and 3/2 can be formed with $(f_{7/2})^3$ [1]. Because each of the three particles has negative parity, the resulting parity is negative.

Indeed, ^{43}Ca shows all these low lying states with expected spin (and also the expected absences - no low lying $1/2^-$ or $13/2^-$ states appear). Although this analysis is reasonably successful, it is incomplete. If we treat all valence particles as independent and equivalent, the energy of a level should be independent of the orientation of the different z-components of the spin - that is, all of the resultant I's should have the same energy. Since this is not true, the observed energy splitting must be analyzed in terms of residual interactions between the nucleons.

Going from one or several independent particles determining the whole fan of nuclear properties, to interacting particles, does complicate the model severely.

The most significant effect on relative shell model energies and other properties is due to residual interactions between the nucleons. This is for instance shown experimentally and understood theoretically for nuclei in the Sn region [3], the Pb region [4] [5] [6] and for nuclei around the so-called 'island of inversion' [7] [8] [9] [11]. This last region of the nuclear chart is discussed both theoretically and experimentally in the next part of this chapter.

2.3 The island of inversion: a first approach

For the even-even $^{32}_{12}Mg_{20}$ isotope, according to Figure 2.1, the neutrons do not play a role in the low energy excitation scheme, because 7 MeV energy is needed to excite two neutrons from the $1d_{3/2}$ sub-shell to the $1f_{7/2}$ in this region. Nevertheless, ground states and low energy states with a non negligible contribution in the wavefunction of neutrons in the $1f_{7/2}$-$2p_{3/2}$ orbitals are observed experimentally. Such excitations of n particles to levels above the magic number (in this case N = 20) are called n particle - n hole intruder states.

Along a chain of isotones: changing Z

Heyde et al. [10] explained this special behavior as function of Z for N = 20 and even Z nuclei in a simplistic way as follows. In the unperturbed system, thus without residual interactions, the energy of the 0^+ 2p-2h configuration is $E_{intr}(0^+) = 2(\epsilon_{j\nu}\text{-}\epsilon'_{j\nu})$ where $\epsilon_{j\nu}$ and $\epsilon'_{j\nu}$ denote the neutron single particle energies in the two major shells. $E_{intr}(0^+)$ is equal to 7 MeV, which is an average of all even Z nuclei with $12 \leq Z \leq 20$ and N = 20 [11] [12] [13] as shown in Figure 2.4(a). It can be calculated via the difference of the neutron separation energy of the N = 20 and N = 21 nuclei and the monopole term of the residual interaction. (This latter term will be explained shortly.):

$$2(S_n(Z, N = 20) - S_n(Z, N = 21)) = 2(\epsilon_{j\nu} - \epsilon'_{j\nu}) + \Delta E_m \qquad (2.1)$$

Three modifications have to be incorporated to this formula for calculating the intruder energy when taking into account the residual interactions:

$$E_{intr}(0^+) = 2(\epsilon_{j\nu} - \epsilon'_{j\nu}) + \Delta E_m + \Delta E_q - \Delta E_{pairing} \qquad (2.2)$$

where the first extra term is the monopole part of the proton-neutron residual interaction, the second term the quadrupole component and the third part is a pairing term. Each term will be discussed.

1. The monopole term can be calculated as follows

$$\Delta E_m = 2\sum_{j_\pi}(2j_\pi+1)\nu^2_{j\pi}[\bar{E}(1f_{7/2}(\nu)j_\pi) - \bar{E}(1d_{3/2}(\nu)j_\pi)] \tag{2.3}$$

with $\bar{E}$ the spin averaged proton-neutron matrix element, which is negative and equal to

$$\bar{E}(j_\pi j_\nu) = \frac{\sum_J(2J+1) < j_\pi j_\nu; J|V_{\pi\nu}|j_\pi j_\nu; J >}{\sum_J(2J+1)} \tag{2.4}$$

and $\nu^2_{j\pi}$ the proton occupation probabilities.

The more overlap between the two wave-functions, the larger the absolute value of this term will be. This monopole term takes into account the relative gain in binding energy for promoting two neutrons from the $d_{3/2}$ into the $f_{7/2}$ orbital. We suppose an attractive delta interaction as the p-n interaction. Because the three proton wavefunctions considered here ($d_{5/2}$, $s_{1/2}$ and $d_{3/2}$) all have more overlap with the $\nu(d_{3/2})$ wavefunction than with the $\nu(f_{7/2})$, the monopole term is positive and increases for this case as function of Z (see Figure 2.4(b)). The unperturbed system plus this term gives the effective single particle energies (ESPE), which represent mean effects from the other nucleons on a nucleon in a specified single-particle orbit.

2. The proton-neutron interaction, for which up to now only the monopole part was considered, has an even larger effect via the quadrupole component. This component can be calculated

$$\Delta E_q = 1.02 N_\pi(\Omega_\pi - N_\pi)^{1/2}(\Omega_\nu - N_\nu)^{1/2} \tag{2.5}$$

with N_π (N_ν) the number of valence proton (neutron) pairs/holes in the defined model space. Ω_π and Ω_ν are the proton and neutron orbital degeneracies, equal to $j_\pi + 1/2$ and $j_\nu + 1/2$. The value of Ω_ν is not uniquely defined since the hole pair occurs in the $8 < N \leq 20$ shell and the particle pair in the $20 < N \leq 28$: we take the average of the $1d_{3/2}$ and $1f_{7/2}$ subshells with one pair of neutrons in each shell. In that case $\Omega_\nu = \frac{((3/2+1/2)-1)+((7/2+1/2)-1)}{2} = 2$.

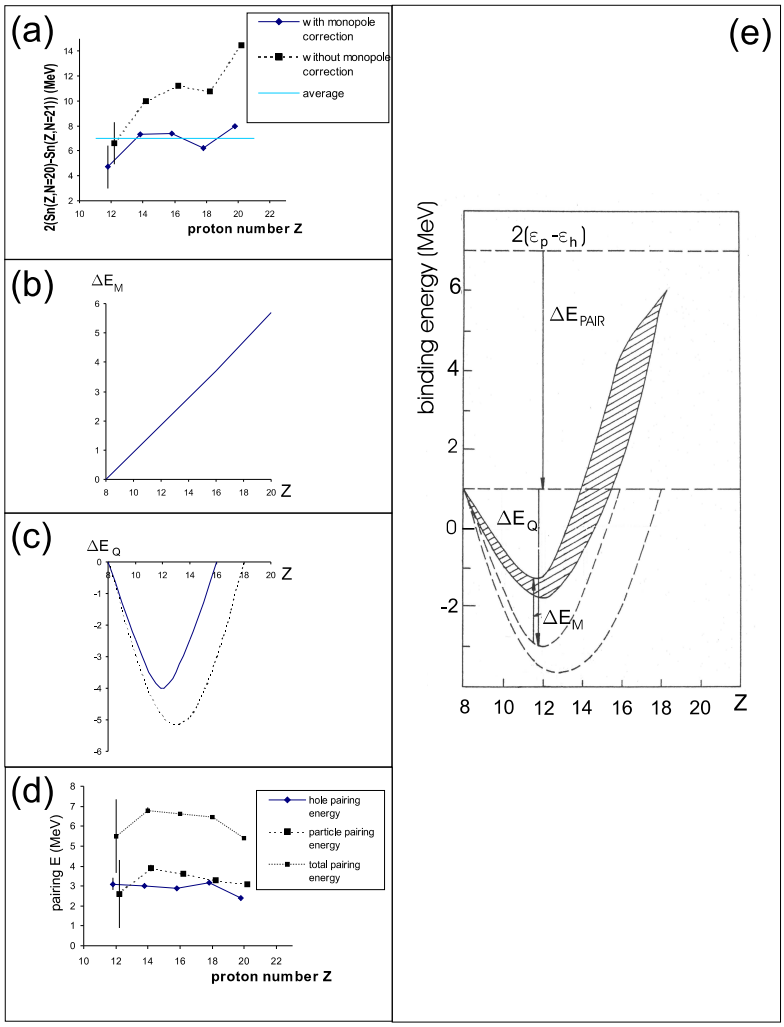

Figure 2.4: (a) Neutron single particle energies of N = 20 isotopes. They are calculated by subtracting the monopole term of the difference in neutron separation energy between N = 20 and N = 21 nuclei. (b) Estimate of the monopole energy for N = 20 nuclei. (c) Estimate of the quadrupole energy for N = 20 nuclei. (d) Estimate of the pairing energy for N = 20 nuclei. The total pairing energy is the sum of the particle and hole energy. (e) Estimated energy of the ν 2p-2h 0^+ intruder state for the N = 20 isotones, relative to the 0p-0h 0^+ state.

Note that this is a very crude estimation, since the $\nu(2p_{3/2})$, $\nu(2s_{1/2})$ and $\nu(1d_{5/2})$ subshells are not taken into account. In explaining the features of Z = 8 - 16 nuclei, we consider the protons to be mainly contributing from the $2s_{1/2}$ and $1d_{5/2}$ subshells since the relative energy spacing between $1s_{1/2}$ and $1d_{3/2}$ is 4.60 MeV. Using these sub-shells, $\Omega_\pi = (1/2 + 1/2) + (5/2 + 1/2) = 4$. Taking into account half of the $1d_{3/2}$ orbit , $\Omega_\pi = (1/2 + 1/2) + (5/2 + 1/2) + 1/2(3/2 + 1/2) = 5$.

This quadrupole term is the part of the p-n force that induces J = 0 to J = 2 pair breaking for both protons and neutrons. It will admix configurations where both proton and neutron 0^+ coupled pairs are changed into 2^+ pairs, which couple to a final 0^+ state. This shows that the quadrupole term favors intruder configurations. This effect is largest at Z = 12 - 14 i.e. at midshell and gradually decreases when going to the shell closures Z = 8 and Z = 20 (see Figure 2.4(c)).

3. The last term is the pairing term. This term gives a large binding energy gain due to the 0^+ coupled particle and hole pairs that are formed in creating 2p-2h configurations. It is derived from experiments as follows:

$$\Delta E_{pairing}(hole) = 2S_{1n}(Z, N = 20) - S_{2n}(Z, N = 20) \tag{2.6}$$

$$\Delta E_{pairing}(particle) = S_{2n}(Z, N = 22) - 2S_{1n}(Z, N = 21) \tag{2.7}$$

with S_{xn} the x neutron separation energy. The average of this term for all even proton nuclei with $12 \leq Z \leq 20$ and N = 20 is 6 MeV, as shown in Figure 2.4(d).

Figure 2.4(e) represents the sum of all these contributions. The expected energy of the 2p-2h states are presented relative to the 0p-0h state energy. From this figure we conclude that the 2p-2h intruder state is predicted as ground state for ^{32}Mg, since its binding energy is predicted below 0 relative to the 0p-0h state. ^{30}Ne and ^{34}Si are on the limit. (note that the full (dotted) line in Figure 2.4(c) and the top (bottom) part of the shaded region in Figure 2.4(e) is obtained with Ω_π=4 (Ω_π=5))

Because the intruder 0^+ state is a combination of several configurations, its occupation of m states is unequal, resulting in a nonspherical shape in contrast to the (almost) spherical normal states. This effect is enhanced due to the fact that the $f_{7/2}$ and $p_{3/2}$ subshells are very close in energy in this region of the nuclear chart and thus induces a large amount of degeneracy of the single particle orbits in the major shell.

In the following, some examples will be given of nuclei with $N \neq 20$ from which the ground state is also dominated by intruder states. The basic idea for explaining the intruder behavior along an isotopic chain is the same as above: in general, an intruder state can be the ground state, if the energy gain due to dynamical correlations including deformation (the quadrupole and pairing term from above) overcomes the energy loss in transcending nucleons across the shell gap. The shell gap is nothing but the difference between ESPE's of the relevant orbits.

Along a chain of isotopes: changing N

In contrast to fixing $N = 20$ and looking along Z, the neutron ESPE changes rather gradually as a function of the neutron number, since the monopole interaction for $T = 1$ is weak. Namely, the neutron shell gap is rather constant as a function of neutron number. This implies that what is crucial in the transition from a normal to an intruder ground state within an isotopic chain is primarily the neutron-number dependence of the correlation energy ($\sim$ quadrupole and pairing term) and its relative magnitude to the shell gap ($\sim$ monopole term). In Figure 2.5, the sources of correlation energy are sketched schematically. Since a normal state of a (neutron) semi-magic nucleus consists of configurations shown in Fig 2.5a, only the proton rearrangement is relevant to the correlation energy, which is generally small. On the other hand, the correlation energy is very large in the case of an intruder composed of configurations like Fig 2.5b, due to the large number of particles and holes in the active orbits. We note that the proton-neutron interaction produces much larger correlation energies than the interactions between like nucleons. This makes the correlation energy in Fig 2.5b much larger than that of Fig 2.5a, favoring the normal-intruder inversion even with a large shell gap.

Note that, as mentioned before, from this figure it is clear that for N = 20 nuclei, the correlation energy difference between normal and intruder states is largest for half filled proton shells, mainly because the more free protons in the sd-shell interact strongly with the extra holes(particles) in the sd(pf)-shells of the intruder configuration the more the correlation energy of the latter configuration increases.

In the cases like Figure 2.5c and d, a normal state of an open shell nucleus has a neutron hole already. The neutron rearrangement is then possible, and strong proton-neutron two-body matrix elements contribute to the correlation energy already in the normal state. The intruder configurations of Figure 2.5d gain correlation energy similarly to the case of Figure 2.5b. However, the difference of correlation energy between Figure 2.5a and b is larger than that between Figure 2.5c and d, because of the saturation of the correlation energy with many particles and many holes as is the case in Figure 2.5d. A specific example from [14] is the following: a semi-magic ^{31}Na gains correlation energy only by 1.7 MeV within the sd-shell, whereas it increases to 3.7 MeV for ^{30}Na and further to 7.2 MeV for ^{29}Na. The correlation energy of intruder states increases more slowly due to the saturation as mentioned just above. This implies that the intruder dominance in N $\leq$ 20 nuclei becomes less favored as N goes down from 20.

2.4 Shell model codes

2.4.1 USD-interaction

The above mentioned intuitive models only give an idea why ground states of some nuclei can be dominated by 2p-2h configurations. To get quantitative information on the contribution of intruder states to the ground state (and excited states) and on the predicted values of other nuclear properties such as g-factors, one needs to make large-scale shell model calculations.

A program of shell model research involves selecting the active nucleon orbits, along with their allowed configurations and couplings, which should encompass the nuclear phenomena of interest (= defining the

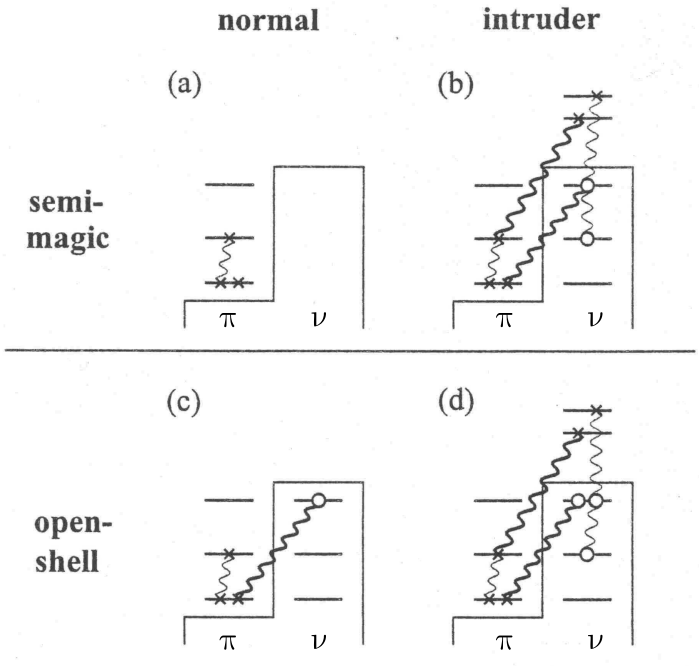

Figure 2.5: Schematic sketch of the sources of the correlation energy of the intruder and the normal states of semi-magic and open-shell nuclei. The proton-neutron interaction is illustrated by thick wavy lines, while the proton-proton and neutron-neutron interactions are drawn by thin wavy lines. This picture is taken from [14]

model space). Then the effective single-particle potential for, and the effective two-body interaction between, the nucleons considered in the model, has to be determined.

For heavier nuclei, the problem of defining a model space that adequately describes the phenomena of interest in 1 nucleus is already a major problem by itself. Defining a space that can describe a range of several nuclei with internal consistency is even more daunting. But, theoretical techniques and computer technology have evolved to the level that sd-shell studies uniformly can use the untruncated sd-shell space (and even more). Hence, these studies offer a view of the inherent powers of the shell model because intrashell truncation problems are eliminated and attention can be focused solely upon the issue of the effective interaction.

Ideally, an appropriate effective Hamiltonian operator could be specified directly by considering experimental nucleon-nucleon scattering data and fundamental theoretical ideas. The free space nucleon-nucleon interaction would have to be modified for the effects of excluded configurations if it were to be used in finite model spaces. Much progress has been made in formally deriving such 'theoretical' effective interactions from first principles, and they have been qualitatively successful [15] [16], however, there are severe shortcomings to this approach when increasing the number of active particles [17].

As an alternative, phenomenological and empirical considerations can be applied to parameterize an interaction that yields a closer correspondence to experiment. There are many ways of making such a parameterization, ranging from those that depend strongly on a model for the interaction to those that are essentially independent of such assumptions. The choice of a delta-function interaction is an example of the former class, and the use of the two-body matrix elements themselves as parameters is an example of the latter.

The essence of the 'model independent' approach is to treat the two-body matrix elements as parameters in a least-squares fit to the experimental binding energies and excitation energies. This technique has

been applied to the 63 two-body matrix elements in the sd shell and is called the 'USD-interaction'. A fit to 447 binding and excitation energies of the sd-shell nuclei yielded for instance a root mean square deviation of only 185 keV [18]. The USD predictions and experimental two neutron separation energy of most of the nuclei in this region are shown in Figure 2.6. The deviations between experiment and theory are indicated by the sizes of the circles at each N value. Most of the circles are quite small, but a few large deviations occur for the most neutron rich Na- and Mg isotopes. These atypical deviations suggest clearly the disappearance of the N = 20 shell closure for this region of the N-Z chart. It is due to the fact that the USD interaction is based on properties of nuclei close to stability, that it reproduces the features of the Standard Nuclear Shell Model, such as the magicity of N = 20, and thus fails in understanding the island of inversion.

Warburton, Becker, Millener and Brown extended the USD interaction in 1990 to nuclei with nucleons in the pf shell. It contains the USD interaction for the sd-part, a combination of a realistic and an empirical model independent interaction for the fp-part and an empirical model dependent part to describe the interaction between the sd and pf part. This interaction is called WBMB throughout the text [19] and has a general good predictive power for ground state binding energies. When excitations across N=20 are forbidden (= 0p0h calculations), the difference between experiment and these calculations is a measure of the importance of intruder states states in this region.

At present, much more data is collected of nuclei around the island of inversion. The main goal of theoretical models now is to explain these data on exotic nuclei together with the data of more stable nuclei, with the same interaction. The difference between the predictions of these new interactions and 0p-0h WBMB calculations for each nucleus, will show the degree of failure of the Standard Nuclear Shell Model for this nucleus. The two most common interactions, based on the shell model, trying to explain the full $8 < Z < 20$ and $8 < N < 32$ region, are discussed in the next paragraph.

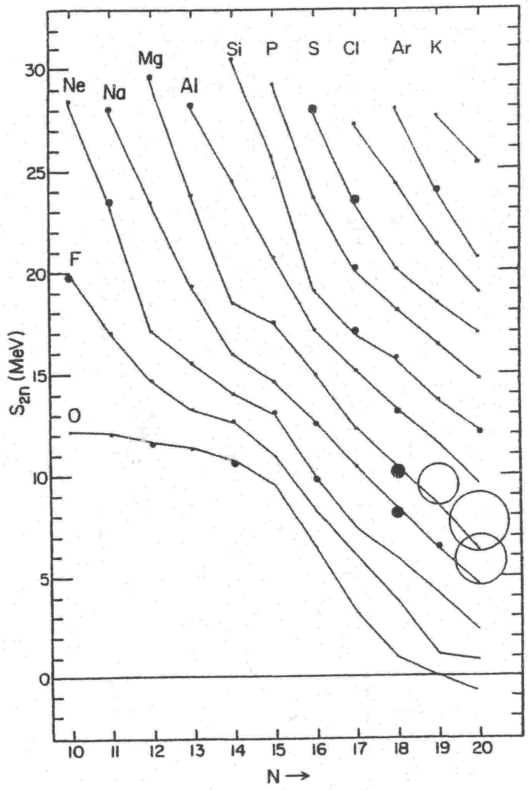

Figure 2.6: Two-neutron separation energies as a function of the neutron number N. The lines are the theoretical values, using the USD-interaction, and the circles are a visualisation of the difference between the theoretical value and the experimental value. This figure is taken from [18].

2.4.2 ANTOINE versus Monte Carlo Shell Model calculations

At present, several codes based on the shell model, each with its own interaction, are used to make extended shell-model calculations in the region of the island of inversion: the ANTOINE code, the MCSM code, the OXBASH code,...

In this work calculations are performed with the ANTOINE code [20] using the USD-interaction, sdpf interaction (described by Retamosa et al. in 1999 [21]) and the sdpf-sm interaction (due to the measurement of the structure of the ground-state and first excited states of ^{35}Si, the sdpf interaction was slightly altered and renamed as sdpf-sm in 2001 [24]) and the Monte Carlo Shell Model [22] code using the SDPF-M interaction (described by Utsuno et al. in 2001 [23]).

One major advantage of the MCSM to the ANTOINE code is the mathematical procedure to obtain the wave functions from the interaction Hamiltonian. The MCSM makes use of the Quantum Monte Carlo Diagonalisation method [25], in which only the basis states important to the eigenstate to be obtained are selected. This gives the MCSM the feasibility of handling many valence particles. The maximum number of valence particles is rather limited in the conventional ANTOINE calculations, where all basis states are used in order to obtain the eigenstates. In exotic nuclei in general and around the island of inversion in particular, two major shells (sd and pf shells) are mixed rather often and states of various character arise at low energy. In such large valence spaces the advantage of the Quantum Monte Carlo Diagonalisation plays a crucial role in clarifying the structure of exotic nuclei far from the β-stability line.

In comparing both interactions, it is of importance to note that A. Zuker [26] has shown that the multipole part of the interaction, responsible for the mixing and correlations (terms 2 and 3 in formula 2.2), is nearly universal. Whereas it has been demonstrated that one can obtain a fully reliable multipole hamiltonian from fundamental theoretical ideas, the monopole term is usually incorrect. The success of the large scale shell model calculations depends crucially on the correctness of

the monopole hamiltonian. This is why the experimental information on some 'simple' singly (closed shells plus or minus one nucleon) exotic nuclei is invaluable.

In the discussion of the experimentally obtained g-factors, the difference in the monopole term between the SDPF-M and sdpf-sm interaction will be of most importance. The effective neutron single particle energies are compared for N = 20 nuclei in Figure 2.7.

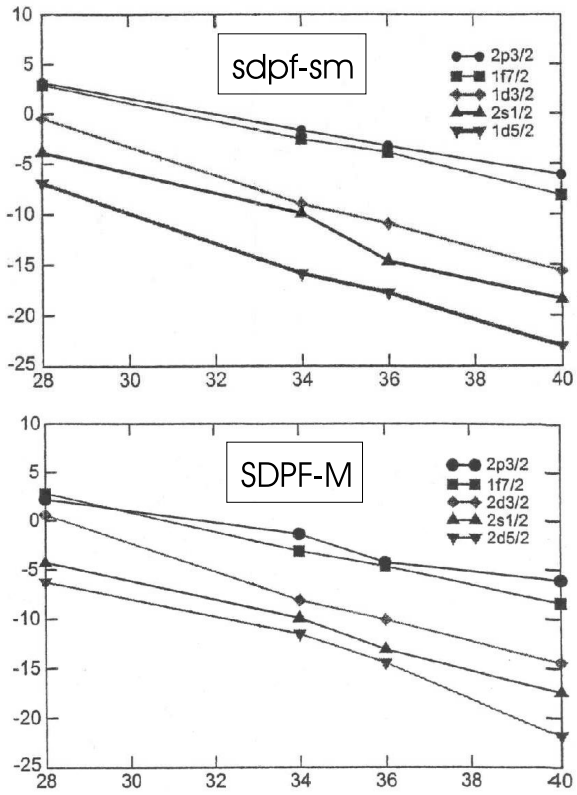

Figure 2.7: Effective neutron single particle energies at N = 20 with the sdpf-sm interaction (top) and the SDPF.M interaction (bottom). This picture is taken from [27]

In going from right to left on this figure, the observed nuclei become more exotic: ^{40}Ca is stable and ^{28}O is not even bound. ^{40}Ca is a normal doubly magic nucleus with a 0^+ ground state and a first excited state at reasonably high energy. The same can be said for ^{36}S: a large N = 20 gap restricts neutrons to occupy the fp-orbits. But the $2d_{3/2}$-$1f_{7/2}$ gap diminishes from 7 MeV in ^{40}Ca to only about 3 MeV in ^{28}O. By reducing the number of protons, a breakpoint will be reached when twice the $2d_{3/2}$-$1f_{7/2}$-gap is as small as the gain in energy from the quadrupole and pairing terms of the 2p-2h intruder states.

In comparing the interaction used in the ANTOINE code and the MCSM interaction, some similarities but also a few major differences are noted. Both interactions are similar between Z = 20 and Z = 16. From there on, they diverge: at Z = 8 the SDPF-M interaction produces a negative $2p_{3/2}$-$1f_{7/2}$ gap, while the $2p_{3/2}$-$1f_{7/2}$ gap is small but positive for the sdpf-sm interaction. Also the $2d_{3/2}$-$1f_{7/2}$ gap is halved in the SDPF.M interaction, mainly due to the upwards shift of the $2d_{3/2}$ orbit, resulting in an increased N = 16 neutron gap. This $2d_{3/2}$-$1f_{7/2}$ gap is only slightly decreased in the interaction used by the ANTOINE code. Notice that the precise definition of the limits of the island of inversion, as well as the actual amount of mixing between normal and intruder states, depends critically on the values of the $2d_{3/2}$-$1f_{7/2}$ and the $1f_{7/2}$-$2p_{3/2}$ gap. Evidently the SDPF-M interaction will produce an enlarged island of inversion and enlarged correlations.

We conclude that the existence of the island of inversion can be explained by the nuclear shell model, when taking into account residual interactions. The precise borders depend crucially on the values of certain parameters used in this model, such as the single particle energies. In the next chapter, we will compare calculations, based on the nuclear shell model, with measured nuclear properties, such as binding energies, spin and parity, g-factors,...

Chapter 3

The island of inversion: experiments

In this chapter an overview is given of most of the experimental measurements in and around the island of inversion. The described region is denoted as the circle in Figure 3.1.

In general, one of the first properties of a nucleus that is measured and can give an indication for a nucleus to be not in agreement with Standard Nuclear Shell Model predictions, is the neutron separation energy. The anomalous experimental neutron separation energy of some neutron rich Na-isotopes was the start for a detailed investigation of this region of the nuclear chart. The measurements of other observables such as the spins and excitation energies of the low energy spectrum, showed that these nuclei are influenced by intruder states and that the ground state has almost pure intruder character, in some cases.

The electromagnetic moments of some neutron rich nuclei around N = 20 are measured as well. These measurements confirm the intruder characteristics and shed more light on the occupation of the valence nucleons and the deformation of the nucleus. All these measured nuclear properties are discussed from low N and low Z to high N and high Z.

Comparison with the theoretical models described above is made in as many details as possible. Some of the ANTOINE calculations, using

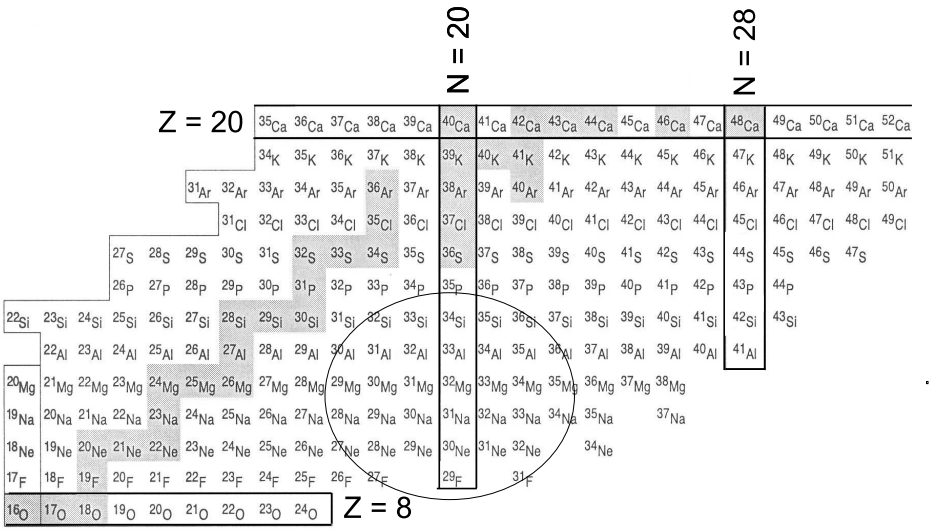

Figure 3.1: A part of the nuclear chart. The circle denotes the region of nuclei that will be discussed in this chapter.

the USD and sdpf-sm interactions, are made by the author. The results from the SDPF-M interaction using the MCSM code, are taken from several articles. The neutron model space used for the MCSM calculations is $sd - p_{3/2}f_{7/2}$, without restrictions on the number of neutrons excited to the pf-shells. In case of ANTOINE calculations, the model space is the same unless otherwise mentioned. In some cases ANTOINE calculations are made with a fixed amount of neutrons in the pf shell. These calculations are referred to as pure np-nh states.

3.1 F-isotopes (Z = 9)

The existence of a particular nucleus, that means a particular combination of protons and neutrons, is one of the basic questions nuclear physics must answer. A puzzling problem related to this, concerns the large jump in the neutron drip line from O (Z=8) to F (Z=9) isotopes. After 53 hours of bombarding a Ta target with a ^{36}S beam at 800enA, no

^{26}O or ^{28}O nuclei were detected (Figure 3.2a) [28]. Figure 3.2b shows the expected production rate as function of the number of removed nucleons from the target, showing that the cross section to make ^{28}O is at least a factor 10 lower than predicted. This means that the life time of ^{28}O is smaller than the flight time which is a good indication that ^{28}O is unbound.

Since ^{31}F is a bound nucleus, at least six more neutrons can be contained in F isotopes, whereas there is just one more proton in comparison with O.

Unbound ^{26,28}O most likely indicate an unbound $\nu(1d_{3/2})$ orbit. Although the energy of the $\nu(1d_{3/2})$ orbit may be lower in ^{29}F due to the strong attractive interaction between $\pi(1\mathrm{d}_{5/2})$ and $\nu(1d_{3/2})$, this alone can not explain the fact that ^{29}F is bound.

Calculations with the MCSM method and the SDPF-M interaction, without taking into account the fp shell, predict ^{29}F to be unbound for 1.6 MeV. According to these calculations, it are the 4p-4h intruder configurations that are the main reason for ^{29}F to be bound. Utsuno shows in Figure 3.3 that only 10% of the ground state wave function of ^{29}F is normal, while the rest are 2p-2h and 4p-4h contributions. This gives a strong indication that ^{29}F belongs to the island of inversion.

Calculations with the ANTOINE code using the sdpf interaction, predict correctly that ^{24}O is the last bound O-isotope, while it incorrectly predicts ^{29}F to be unbound by (only) 250 keV.

^{27}F has two valence neutron holes, that causes this isotope to be bound, because of the correlations of these holes with the one proton in $\mathrm{d}_{5/2}$. Thus, in order to explain the fact that ^{27}F is bound, no intruder components are needed to be taken into account, in contrast to ^{29}F.

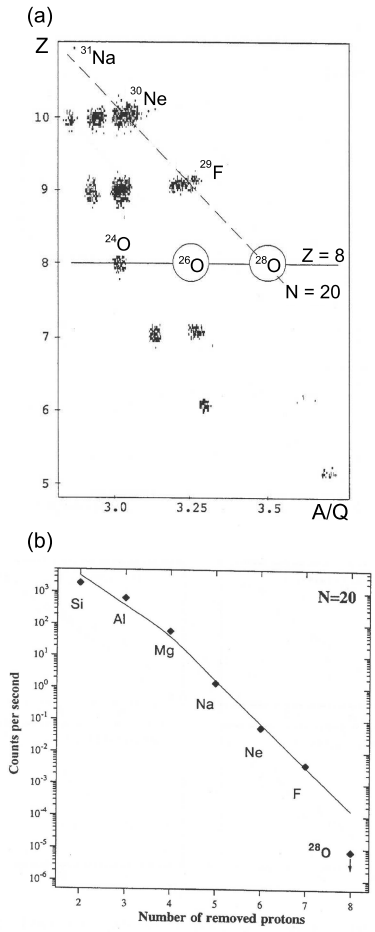

Figure 3.2: (a) Two dimensional identification plot Z versus A/Q, with Q the charge of the nucleus. No counts were observed corresponding to ^{26}O and ^{28}O. (b) Measured yields of the N = 20 nuclei. The solid line represents yields calculated with the modified formula of Summerer et al. [29]. The point with arrow for ^{28}O corresponds to the upper limit of 1 event. Picture taken from [28].

The large jump in the neutron drip-line from O to F suggests that N = 16 is a magic number for the O-isotopes. Figure 3.4 shows S_n as function of N. A magic number appears as a decrease of S_n along with an increase of N. The traditional magic numbers N = 8, 20 are clearly seen close to the stable nuclei as breaks in the small isospin numbers lines. However, the break at N = 8 (N = 20) disappears at neutron rich $T_z = 3/2$ ($T_z = 4$). On the other hand, a break in the S_n line appears at N = 16 for O (for $T_z = 7/2$ and $T_z = 9/2$), which is less pronounced for F (for $T_z = 3$ and $T_z = 4$) [30].

Even though the first 2^+ state of ^{24}O has not been directly observed, its energy has been shown to lie above 3.8 MeV, indicating again the N = 16 shell closure [31].

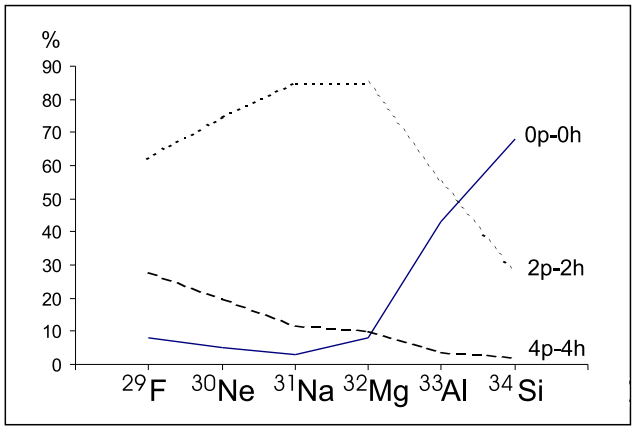

Figure 3.3: With the SDPF-M interaction calculated probabilities of 0p-0h, 2p-2h, and 4p-4h configurations in the ground state of N = 20 isotones, indicated by dotted, solid and dashed lines, respectively.

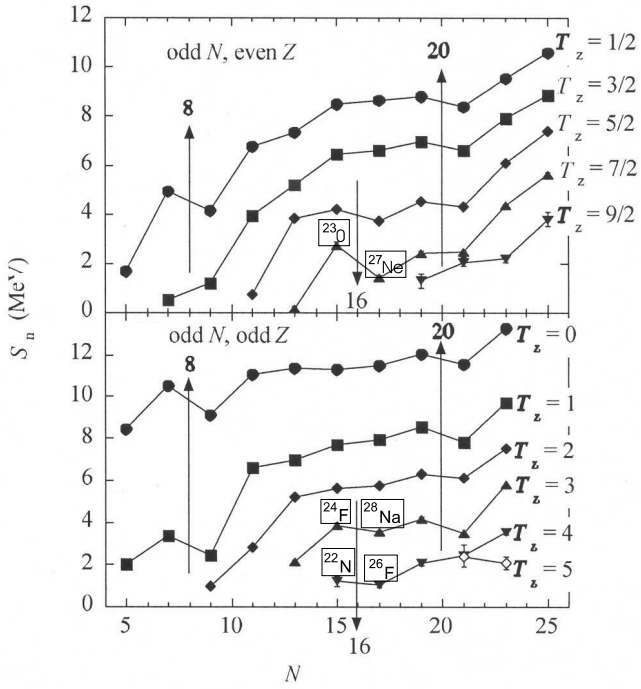

Figure 3.4: Neutron number (N) dependence for experimentally observed neutron separation energies (S_n).

3.2 Ne-isotopes (Z = 10)

$^{28}_{10}\mathbf{Ne}_{18}$

The excitation energy of the 2^+ state in ^{28}Ne is measured and found to be 0.5 MeV too low (1.81 MeV according to USD and 1.32 MeV experimentally) [32]. The measured B(E2) does not provide more evidence about a possible admixture of intruder components into the wave function, because its large error does not distinguish a low mixing scenario (Figure 3.5). The MCSM predicts on average 50% even particle - even hole excitations from the normal filling, suggesting that ^{28}Ne belongs to the island of inversion.

$^{29}_{10}\mathbf{Ne}_{19}$

For ^{29}Ne only the life-time was pinned down and this value was not in disagreement with the sd-model [34]. More nuclear properties need to be measured in order to draw conclusions on ^{29}Ne.

$^{30}_{10}\mathbf{Ne}_{20}$

According to the binding energies ^{30}Ne is the only Ne-isotope of which the measured value is in profound disagreement with the WBMB interaction (see Figure 3.6).

Also the energy of the first 2^+ state is at variance with the WBMB calculations: approaching a magic number, the energy of the first 2^+ state should increase, while the value of B(E2) should decrease, because of less collectivity and deformation. This is not the case for ^{30}Ne: the 2^+ state is at 791 keV [35], 1 MeV lower than expected from the USD interaction (Figure 3.5). The recently measured B(E2) value of ^{30}Ne also indicates the necessity of the fp shells in order to explain the properties of this isotope, although the measurement was not conclusive due to the imprecision $(460(270)e^2fm^4)$.

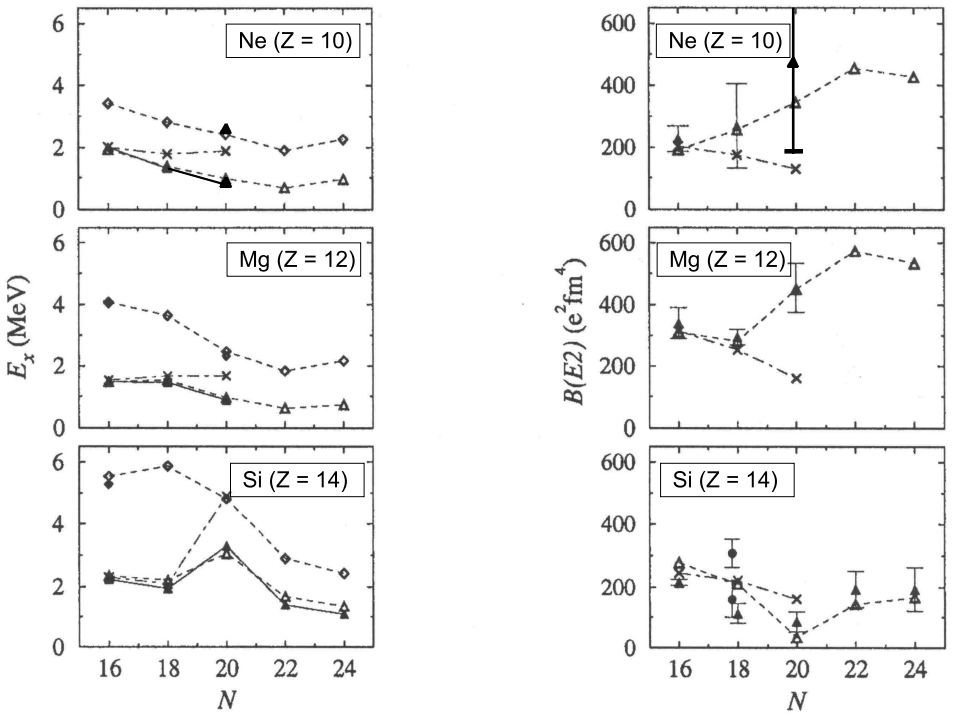

Figure 3.5: (*left*) Energy levels of Ne, Mg and Si isotopes. The filled (open) triangles, diamonds denote the experimental (calculated - using the SDPF-M interaction) first 2^+ and 4^+ levels, respectively. The crosses are the energies of the first 2^+ state calculated with USD. – (*right*) B(E2) values of Ne, Mg and Si isotopes. Part of picture taken from [33]

Figure 3.3 shows that the MCSM also claims the ground state to be largely dominated by 2p-2h and 4p-4h intruder components. The same general prediction was made using the sdpf interaction of the ANTOINE code: the energy of the pure 2p-2h state with the full fp shell as model space is predicted 321 keV lower than the pure 0p-0h state. ^{30}Ne does thus belong to the island of inversion.

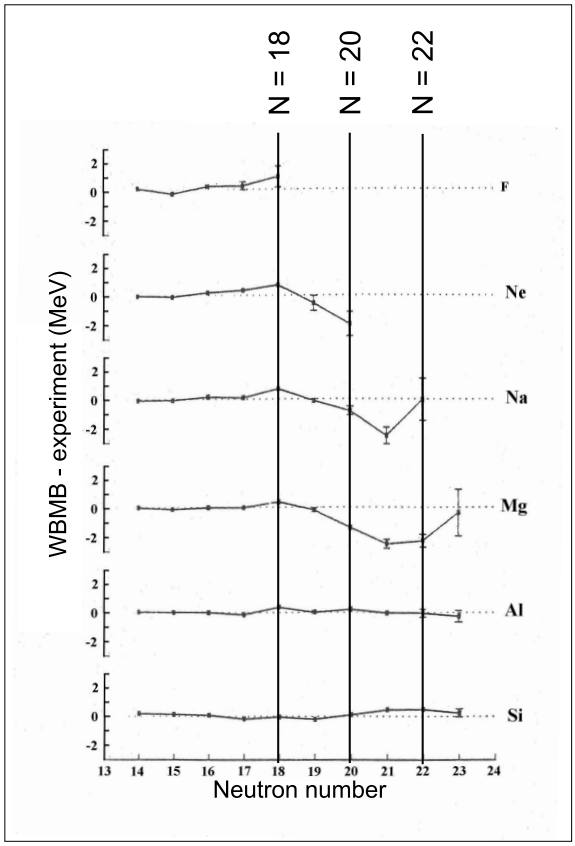

Figure 3.6: Difference between experiment and theory (using the 0p-0h WBMB interaction) for binding energies of nuclei with Z between 8 and 14. Picture taken from [40]

3.3 Na-isotopes (Z = 11)

Looking at the whole Na-chain, it is immediately clear from Figure 3.6 that the binding energies of very neutron rich Na isotopes can not be explained with the 0p-0h WBMB interaction [36]. In this subsection we will go into more detail on several other nuclear properties of some Na-isotopes around the island of inversion.

$^{27}_{11}\mathbf{Na}_{16}$

As shown in Figure 3.7, the USD interaction and the SDPF-M interaction give similar energy levels. In the first MeV of excitation energies a state substantially affected by intruder components does not appear. The calculated energy levels are in good agreement with the experimental ones [37] except for the absence of the 1.725 MeV state in the theoretical spectra, tentatively assigned as a $1/2^-$ and explained by a single particle excitation from the Z = 8 closed shell.

The g-factor measured by Keim et al. [38] resulting in a magnetic moment $\mu_{measured} = 3.894(3)\mu_N$ is in reasonable agreement with the free g-factor result from the USD interaction ($\mu_{USD} = 3.711\mu_N$).

The experimental quadrupole moment ($Q_{exp} = -0.72(3)efm^2$) [39] is somewhat larger than the calculated USD value ($Q_{theoretical} = -0.46efm^2$), using the free nucleon charges. The reason for this is the well-known effect of the core polarization of the core protons by the valence protons and neutrons. This polarisation represents a part of the actual wave functions which are left out of the truncation to the sd shell. Empirically it can be accounted for by replacing the free-nucleon charges with effective charges. Using $e_p = 1.3$ and $e_n = 0.5$ in the USD interaction, a quadrupole moment equal to -1.10 efm^2 is calculated. Using the same effective charges in the SDPF-M interaction, very good agreement between theory and experiment is observed as well (Figure 3.8) [14].

Note that the quadrupole moment of ^{27}Na is rather small because the main part of the wavefunction consists of protons in the middle of the $d_{5/2}$ shell and the neutrons fill up the $2s_{1/2}$ sub-shell [41].

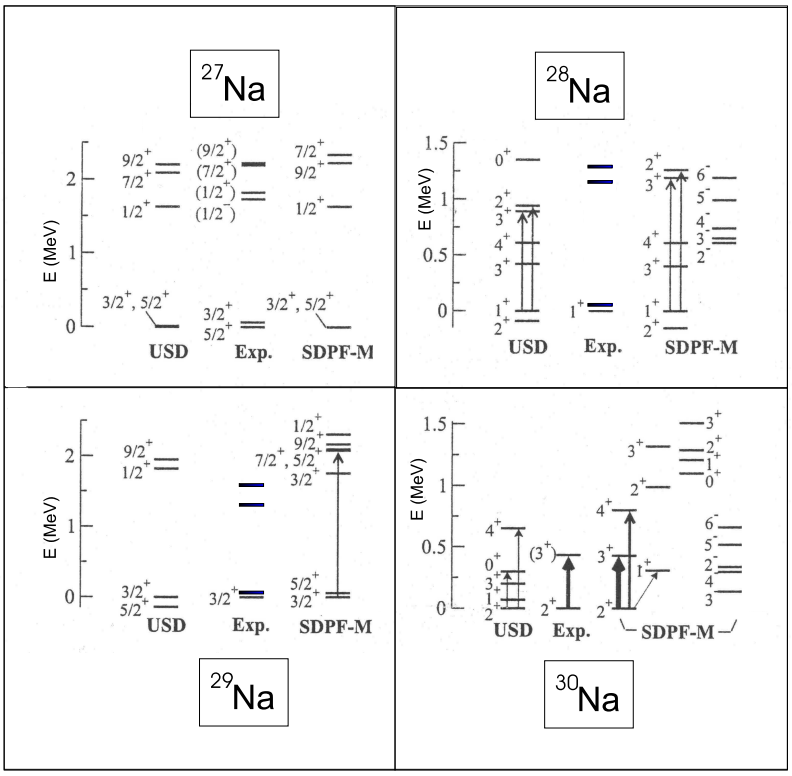

Figure 3.7: Comparison of the energy levels of $^{27-30}$Na relative to the experimental ground state among the experiment and the shell-model calculations by the SDPF-M and the USD interactions, using the MCSM approach. [14]

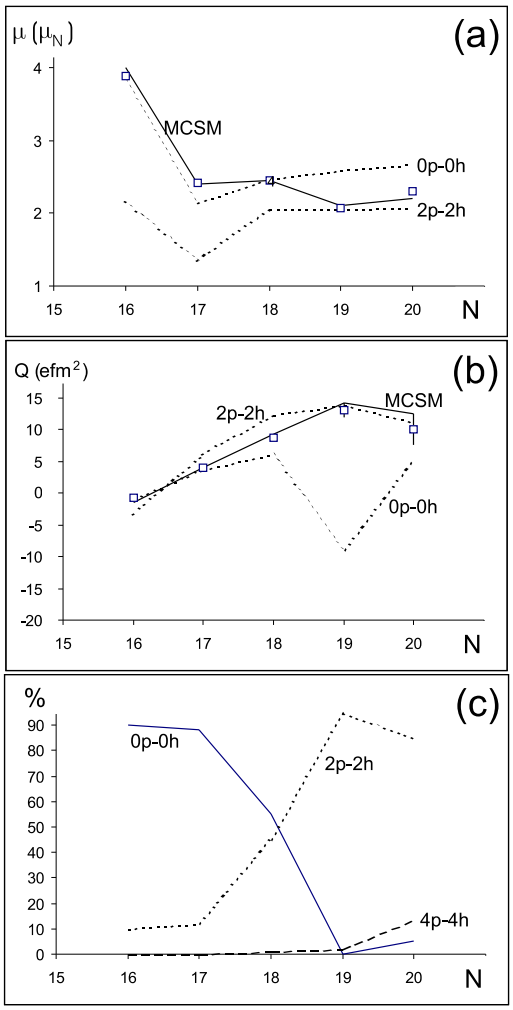

Figure 3.8: (a) Magnetic dipole moments, (b) electric quadrupole moments, and (c) np-nh (n = 0,2,4) probabilities of the ground states of neutron-rich Na-isotopes, as function of neutron number, N, calculated with the SDPF-M interaction. In (a) and (b) the squares denote the experimental values, while the solid and the dashed line represent, respectively, the MCSM calculation with the SDPF-M interaction and sdpf-sm interaction without particles excited to the pf-shell (0p-0h) and with two neutrons fixed in the $f_{7/2}p_{3/2}$ shell. [14]

$^{28}_{11}\mathbf{Na}_{17}$

The experimental ground state spin of ^{28}Na is I=1 [42] while in the calculations (USD and SDPF-M) the 1^+ is located a little higher than the 2^+ (Figure 3.7). The recent Coulomb excitation experiment by Pritychenko et al. [43] shows a gamma ray at 1.24 MeV with B(E2)=$54(26)e^2fm^4$.

This energy level and the according B(E2) are not in contradiction with the USD model nor with the SDPF-M interaction. A slight preference for the SDPF-M interaction comes from the fact that the 2^+ and 3^+ states are predicted a little higher in energy, and consequently a little closer to the experimentally observed level. As the gap between the $\nu(2s_{1/2})$ and $\nu(1d_{3/2})$ orbit is larger for the SDPF-M interaction, those states are pushed up. As for ^{27}Na, the magnetic and quadrupole moment are in good agreement with the USD interaction, the sdpf-sm interaction without excitations across N = 20 (= sdpf-sm 0p-0h) and the SDPF-M interaction (Figure 3.8), thus supporting the conclusion from these calculations that almost no intruder components are present in the ground state wave function.

$^{29}_{11}\mathbf{Na}_{18}$

The experimental ground state of ^{29}Na is I = 3/2 [42]. The calculations show very close 3/2 and 5/2 levels, but the USD interaction puts the 5/2 as ground state while SDPF-M predicts the correct ground state spin of 3/2. This difference arises from the fact that the 3/2 state contains a larger mixing of the intruder configuration than the 5/2.

Tripathi et al. [44] measured the β-decay of ^{29}Ne to ^{29}Na. They observe large β-decay branching ratios to levels at 1249 keV and 1588 keV, implying spin assignments of $1/2^+, 3/2^+$ or $5/2^+$ for these levels, since the ground state spin of ^{29}Ne is supposed to be $3/2^+$.

However, the USD calculations predict only one state in this spin range below 2.8 MeV. Also within the USD shell model the almost degenerate states of the ground state doublet are expected to be equally

populated via Gamow-Teller β^--decay transition. This contradicts the observation of 33% decay to the first $5/2^+$ state and almost no decay to the $3/2^+$ ground state.

The MCSM calculations predicts four more states within the spin range $1/2^+ - 5/2^+$, below 2.5MeV with large probability of 2p2h excitations. The large β-decay branch to the first excited state of ^{29}Na at 72 keV makes it a likely candidate for the $5/2^+$ state predicted as a member of the ground state doublet. The $3/2^+_2$ (65% of 2p2h contribution) and $5/2^+_2$ (78% of 2p2h contribution) are good candidates for the 1249 and 1588 keV experimental levels. These β-decay results also support a $3/2^+$ assignment to the ground state of ^{29}Ne with strong 2p2h intruder mixing.

At N = 18, the calculations with the sdpf-sm 0p-0h and the SDPF-M interaction give similar magnetic moments in good agreement with the experiment. On the other hand, the quadrupole moment is 30% larger with the SDPF-M interaction than with the sdpf-sm 0p-0h interaction. A very precise measurement of the quadrupole moments of the Na isotopes has been carried out by Keim et al. [38]. The measured quadrupole moment of ^{29}Na is 8.6(3)efm^2, in good agreement with the SDPF-M prediction. The MCSM calculation shows a large mixing of intruder configurations (42%), and this effect is clearly visible in the quadrupole moment. Notice that the experimental quadrupole moment is in between the 0p-0h and pure 2p-2h prediction of the sdpf-sm interaction, indicating the presence of intruder components according to the sdpf-sm interaction (Figure 3.8).

Utsuno et al. [108] claim that the difference between the SDPF-M and USD interaction is solely due to the monopole part of the interaction. This is shown by calculating nuclear properties while varying the N=20 shell gap from the value that is given by the SDPF-M interaction. This can be done by changing the T = 0 (T = 1) part of the monopole interaction between the $0d_{5/2}$ and the $0d_{3/2}$ by 0.7x MeV (-0.3x MeV).

The parameter x controls the ESPE: x = 0 represents the situation with the SDPF-M interaction as a starting point, while x = 1, reproduces the gap of the USD interaction (4.3 MeV), in which the

property of the monopole interaction causing the disappearance of the magic number [45] still remains but may not be enough. A larger x means primarily a lower neutron $d_{3/2}$ level, i.e., a wider N = 20 gap.

In Figure 3.9 (bottom panel) we clearly see that the quadrupole moment of ^{29}Na can best be explained with x = 0. According to Figure 3.8 this corresponds to a partly mixed ^{29}Na ground state.

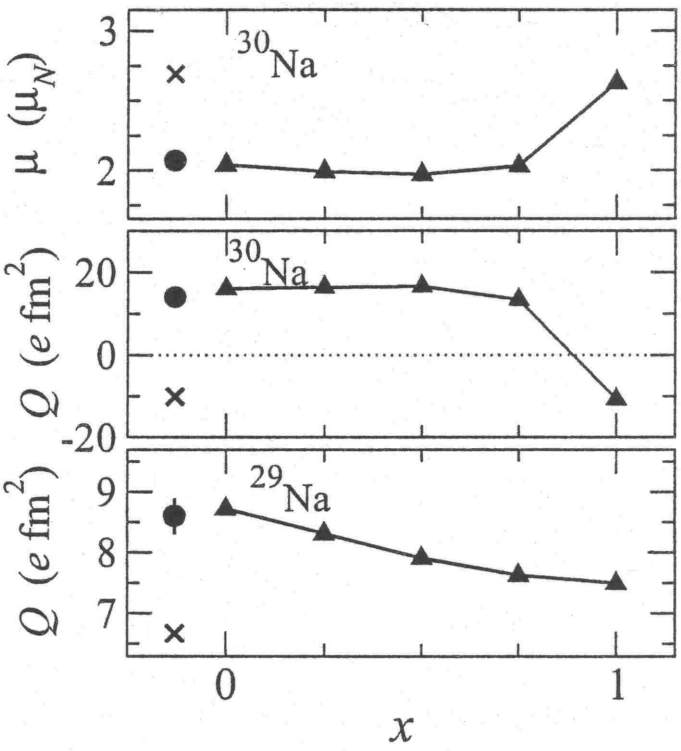

Figure 3.9: Magnetic moment of ^{30}Na and quadrupole moment of ^{29}Na and ^{30}Na as a function of x. x = 1 (x = 0) corresponds to the gap of the USD-interaction (SDPF-M interaction). The circles, crosses and triangles show experimental values, USD model values and SDPF-M values, respectively. Picture taken from [108].

$^{30}_{11}\mathbf{Na}_{19}$

The measured binding energy and the spin of the ground state of ^{30}Na are both in very good agreement with the USD model (Figure 3.7). In this model, the low-lying states are composed mainly of the configurations with a neutron hole $\nu(\mathrm{d}_{3/2})^{-1}$ coupled weakly to the proton I = 3/2 or 5/2 states.

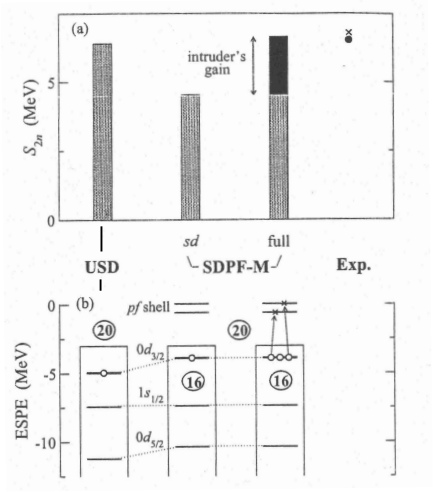

Figure 3.10: (a) Comparison of calculations and experimental S_{2n} values of ^{30}Na. For the SDPF-M interaction, a truncated calculation within the sd shell and the full calculation are compared. The circle and the cross are experimental data. (b) Corresponding dominant neutron configurations of the ground state and the ESPE's obtained from each interaction. Picture taken from [108].

When looking at the g-factor and the quadrupole moment (Figure 3.8) it is evident that the sdpf-sm 0p-0h interaction does not reproduce the experimental values. The pure 2p-2h intruder state, on the other hand, is in almost perfect agreement with the experimental quadrupole moment. This shows that the ground state wave function of ^{30}Na is most likely almost fully determined by intruder components.

This idea is enforced by the MCSM calculations. They predict the quadrupole moment equally well and suggest an almost pure intruder ground state, which is strongly deformed. A rotational band connected with a strong E2 transition is obtained. This transition is recently measured [43] and corresponds well with the MCSM calculation (MCSM: 168 e^2fm^4 and experiment: 130 $^{+90}_{-65}e^2fm^4$), but not with the spherical prediction of the USD interaction (USD: 5 e^2fm^4).

Although the ground state of ^{30}Na is almost fully determined by the 2p-2h intruder states, the two neutron separation energy can be reproduced reasonably well both by the USD and SDPF-M models. The reason for this is illustrated in Figure 3.10, where the experimental S_{2n} of ^{30}Na with the calculated values using the USD interaction and the SPDF-M interaction is compared. With the SDPF-M interaction, two calculations are carried out, i.e., a truncated shell model calculation within the sd shell and the full calculation. The results from the USD and the SDPF-M calculation within the sd shell show rather different S_{2n} values, despite the same model space used. In order to understand this, the ESPE is shown in Figure 3.10. In the SDPF-M interaction, the ESPE of the $\nu(0d_{3/2})$ level for small Z is higher than in the USD interaction. On the other hand the intruder configurations dominate the ground state in the full SDPF-M calculation, increasing the binding energy and making S_{2n} larger to the same extent as the USD calculation in the sd shell. Thus, almost the same separation energies can be obtained from a different mechanism. One has to combine other physical observables to draw definite conclusions.

$^{31}_{11}\mathbf{Na}_{20}$

The measured binding energy of this N = 20 isotope was the first indication that the N = 20 shell closure is disappearing for neutron rich nuclei in this region, because this nucleus is 2 MeV more bound than the USD calculations predict (see Figure 3.6).

Experimentally, the ground state spin is proven to be $3/2^+$, while the USD interaction predicts a spin $5/2^+$, due to the odd proton in the $\pi(d_{5/2})$. The sdpf-sm interaction was used to calculate the energies of the pure normal and pure intruder states with the ANTOINE code. The pure 2p-2h intruders are expected to lie 1.6 MeV below the normal states. The $3/2^+$ ground state and low lying $5/2^+$ state is predicted correctly.

Again the g-factor and quadrupole moment are not in agreement with the sdpf-sm 0p-0h interaction. The pure 2p-2h predictions show evidence of strong intruder mixing into the ground state (Figure 3.8).

The MCSM calculation is nicely in agreement with the experiments for the obtained spin, magnetic- and quadrupole moment (Figure 3.7 and 3.8). This study shows that while the ground state is dominated by 2p-2h excitations, it is pulled down 700 keV due to mixing with higher laying np-nh levels with $n > 2$, giving rise to good agreement with experiment. The observed first excited state at 350(20) keV is predicted at 310 keV.

Recently Pritychenko et al. [52] measured the deformation parameter of ^{31}Na by populating the excited $5/2^+$ state via intermediate energy heavy-ion scattering. The state appears to be the first rotational excitation built on the I = 3/2 ground-state. Using a rotational model, a deformation parameter $\beta_2 = 0.59(10)$ was derived in reasonable agreement with the MCSM (0.53).

$^{32}_{11}\mathbf{Na}_{21}$

From the root-mean-square matter radii, combined with the isotope-shift data of a series of Na isotopes, a monotonic increase in neutron skin (up to 0.2 or 0.4 fm for ^{32}Na depending on the model) was observed as the neutron number increases [42] [47]. Together with the difference of ~ 2 MeV between the measured binding energy and the calculations using the WBMB interaction, these experimental data can be considered as evidence for the intruder character of the ground state of ^{32}Na.

$^{33}_{11}\mathbf{Na}_{22}$

Although the error is large, the binding energy of ^{33}Na is in agreement with the WBMB calculations.

ANTOINE calculations using the sdpf-sm interaction with the full $\nu(sd-pf)$ shells as valence space, predict the pure 2p-2h (1p-1h) intruder state at 1 MeV (1.5 MeV). Assuming a normal configuration for the ground state of ^{33}Na, β-decay branches to a 1p-1h ^{33}Mg ground state, to the first 1p-1h $5/2^+$ state at 811 keV and to a multiplet of states located around 4 MeV, are expected from these calculations. This is in agreement with the experimental results exhibiting the strong β branches deduced from the delayed neutron measurement [48]. The agreement between the measured half life of ^{33}Na (8.0(3)ms) [49] and these calculations (2.7ms), without excitations across N = 20, can be considered fair.

3.4 Mg-isotopes (Z = 12)

Figure 3.6 shows that the binding energies of very neutron rich Mg isotopes can't be explained without taking into account intruder configurations. ^{32,33,34}Mg are several MeV more strongly bound than expected.

From the interaction cross section of Mg isotopes with C, Suzuki et al. [47] confirmed that next to the Na isotopes, also the Mg isotopes form a neutron skin when going more exotic. A thickness of 0.4 fm for the neutron skin of ^{32}Mg is predicted.

We mention that our group recently measured the g-factor and quadrupole moment of ^{29}Mg which are both in good agreement with the free g-factor and quadrupole moment calculated with the USD interaction and using $e_p = 1.3$ $e_n = 0.5$: $\mu_{USD} = 0.96$ - $\mu_{exp} = 0.980(2)$ and Q_{USD} = -95mbarn - Q_{exp} = -107(25)mbarn [50]. Concerning β decay, spin and parity of the ground state, ^{30}Mg is the first Mg isotope to be discussed in detail.

$^{30}_{12}\mathbf{Mg}_{18}$

Figure 3.11 shows the results of several B(E2) measurements in the Mg chain. The B(E2) value of ^{30}Mg is measured up to three times: once at GANIL [51], once at MSU [52] and the last time at CERN [53]. Because only the MSU and CERN data agree with each other and the CERN data are quoted as the most reliable result, we omit the GANIL data. Comparing these results with the ANTOINE calculations using the sdpf-sm interaction without pf-shell excitations, a good agreement is found with experiment. Note that the MCSM is in agreement with the experiment as well and predicts only 0.3 as average number of neutrons excited to the $N > 20$ subshells [54].

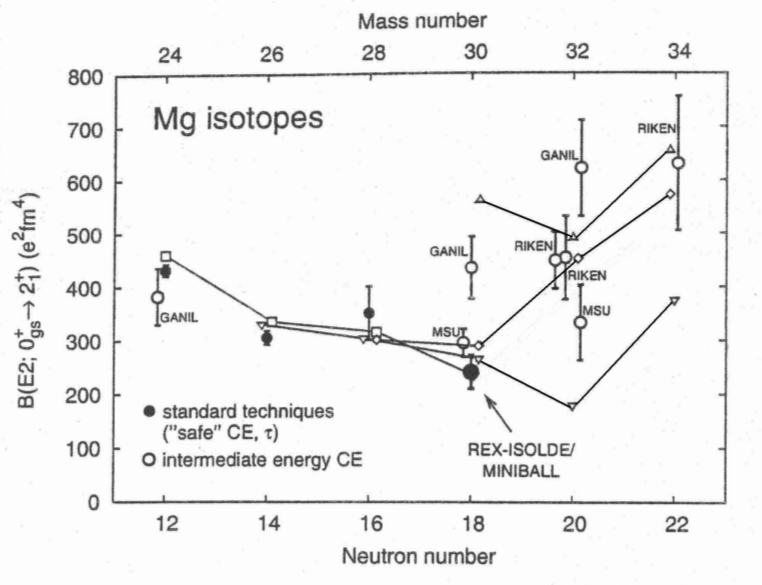

Figure 3.11: Experimental (open and filled circles) and theoretical B(E2) values (connected by thin lines to guide the eye) for the even Mg isotopes. ♢=SDPF-M ∇=sdpf-sm 0p-0h Δ=sdpf-sm pure 2p-2h. Picture taken from [53].

A level at 1789 keV is proposed to be the 2p-2h intruder 0^+ state in ^{30}Mg. The 306 keV transition from this level to the first excited (normal) 2^+ level is slow as would be expected for a transition between intruder collective and normal spherical states $B(E2; 0_2^+ \rightarrow 2_1^+) = 10.8(1.1)e^2fm^4$ [55]; (for a comparison $B(E2; 2_1^+ \rightarrow 0_1^+) \sim 40e^2fm^4$).

$^{31}_{12}\mathbf{Mg}_{19}$

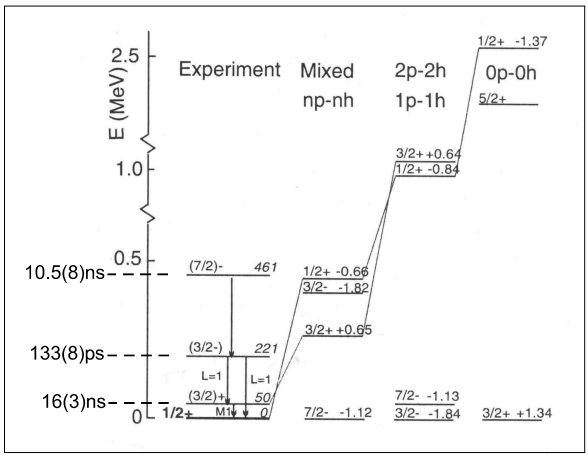

Figure 3.12: Partial experimental level scheme of ^{31}Mg (left) compared to various shell model calculations (from left to right: SDPF-M – pure 1p-1h and pure 2p-2h values from sdpf-sm – 0p-0h values from sdpf-sm). The magnetic moments of the theoretical levels are mentioned on the right (units μ_N) and should be compared with $\mu_{exp} = -0.88355$

Due to the measured β decay of ^{31}Na to ^{31}Mg and ^{31}Mg to ^{31}Al, it was concluded by Klotz et al. [56] that the ground state of ^{31}Mg has spin and parity $3/2^+$. They noticed that the very rich low energy spectrum of ^{31}Mg can only be explained by taking into account the pf levels and they suggested that the ^{31}Mg ground state has 50% mixing of normal and intruder components. Still, their own calculations of the β decay of ^{31}Mg put too much β intensity into the ground state of ^{31}Al (72% in comparison with only 13% experimentally observed).

Neyens et al. [57] recently measured unambiguously the spin, parity and magnetic moment of the ^{31}Mg ground state by combining the results of a hyperfine-structure measurement and a β-NMR measurement, both performed with an optically polarized ion beam at ISOLDE (CERN). The unexpected $1/2^+$ ground state with μ_{exp} = -0.88355 can only be explained as an almost pure 2p-2h configuration, of which the sdpf-sm interaction predicts a magnetic moment of -0.84 in reasonably good agreement with experiment. As is shown on Figure 3.12 both the ANTOINE and MCSM code predict the 1p1h state, with negative parity, to be below the 2p2h $1/2^+$ state. The MCSM puts the first $1/2^+$ state even higher than the first 3/2 state, but does reproduce better the high level density below 500 keV.

The spin-parity assignment proposed by Neyens et al. was further supported by the measurement of the lifetime of the 461keV and 221 keV state [55] (see Figure 3.12). The 461 keV state was measured to be 10.5(8)ns and the 221 keV state 133(8)ps in agreement with a collective E2 and an E1 transition respectively, as expected from the spin assignment of Neyens et al. The $B(E2; 3/2^- \rightarrow 7/2^-)$ value of 67(6)e^{2}fm^4 compares very closely to the value for the 2p-2h intruder in ^{32}Mg (67(14)e^{2}fm^4).

The 2p-2h intruder dominated ^{31}Mg ground state will more easily decay to an other 2p-2h intruder state in ^{31}Al than to the normal ground state, which explains the discrepancy in the ground state feeding mentioned above. Note that Marechal et al. [58] remeasured the β decay of ^{31}Mg and found a ground state feeding even less than Klotz et al. ($< 1\%$), in correspondence with the expected hindered intruder to normal decay.

$^{32}_{12}\mathbf{Mg}_{20}$

This N = 20 nucleus does not behave as a semi-magic nucleus at all. Next to the non-normal binding energy, the half-live of ^{32}Mg should be around 26 ms according to the USD interaction, while this nucleus is at least five times longer lived. The first excited 2^+ state is at 890 keV, 800 keV lower than expected. The B(E2) value was measured several times. Not all results are in agreement with each other, but they are all appreciable higher than the USD value as shown in Figure 3.11 [51] [52] [59]. The MCSM gives a B(E2) value close to most of the measured values and claims 2.0 as an average number of neutrons excited to $N > 20$ subshells.

A second excited state at 2315 keV is populated by inelastic nuclear scattering of a ^{36}S beam on a ^{28}Si target [60]. It is highly possible that this level at 2315 keV is a 4^+ state [61]. If so, $E(4^+)/E(2^+) = 2.6$, in between the value for a rotational (3.3) and a vibrational nucleus (2.0). If rotational, the interpretation of a high B(E2) as corresponding to a highly deformed nucleus may be right.

But Mittig et al. [60] believe this state is a 1p1h 3^-: a strongly observed gamma line of 1.47(5) MeV can correspond to the decay of this state to the 2^+ state at 890 keV. The state at 2315 keV is highly populated by the (probably) 3^- or 4^- ^{32}Na β decay, suggesting indeed a negative parity. Mittig et al. claim that a spin parity assignment of 4^+ is wrong, since in that case the inelastic nuclear cross section measured for this state should be much lower.

$^{33}_{12}\mathbf{Mg}_{21}$

Also ^{33}Mg is one of the Mg isotopes of which the binding energy is much larger than expected from the standard nuclear shell model. Theoreticians and experimentalists all agree that this nucleus has a rich low energy spectrum, containing normal, 1p-1h and 2p-2h states. Nummella et al. [49] measured the logft value of the β-decay of the ^{33}Na ground state to the ground state of ^{33}Mg to be 5.27(27). This value indicates an allowed transition with no change in parity and either no change in spin or 1 unit. Assuming that the ground state of ^{33}Na is $3/2^+$, the

ground state parity of ^{33}Mg should be positive and it's spin 1/2, 3/2 or 5/2, according to this logft value. Pritychenko et al. [62] measured the transition strength from the 485 keV excited level to the ground state. This measurement can not be explained with a $1/2^+$ or $3/2^+$ ground state of ^{33}Mg, but can be in agreement with a $5/2^+$ ground state and a $7/2^+$ rotational excitation as the 485 keV level.

In the near future, as for ^{31}Mg, Neyens et al. will attempt to measure the spin, parity and magnetic moment of the ^{33}Mg ground state by combining the results of a hyperfine-structure measurement and a β-NMR measurement. These results will be discussed in the thesis work of D. Yordanov.

$^{34}_{12}\mathbf{Mg}_{22}$

The strong binding energy, together with an even lower 2^+ state than ^{32}Mg (660keV) [63] already denotes the influence of intruder states in the low energy spectrum of this nucleus. Recently the measurement of the very large B(E2) value by Iwasaki (631(126)e^{2}fm^4) [64], made them conclude that ^{34}Mg has a similar deformation parameter as the very deformed ^{32}Mg nucleus. Notice that ^{34}Mg is expected to be more deformed than ^{32}Mg also due to the 2 extra neutrons in the fp-shell. This is shown in the calculation of the B(E2) value using the sdpf-sm interaction without excitations across N = 20: $B(E2)$ of $^{32}Mg \simeq 170e^2fm^4$ and $B(E2)$ of $^{34}Mg \simeq 380e^2fm^4$ (see Figure 3.11).

Sakurai et al. [65] claim that the energy of the first 4^+ state is 2120 keV, 3.2 times higher than the first 2^+ state, which makes the E(4^+)/E(2^+) ratio close to the limit for rotational nuclei, 10/3. The MCSM gives 1.8 as an average number of neutrons excited from the normal configuration, very similar to the number for ^{32}Mg.

3.5 Al-isotopes (Z = 13)

Looking at the binding energies, the whole Al-chain looks normal. But several other nuclear properties, such as g-factors, spins and parities of low lying states were measured and not all of them are fully explainable within the sd-model. Starting from the stable ^{27}Al nucleus and going more exotic, the first intriguing Al-isotope is ^{32}Al.

The magnetic moments of the less exotic isotopes (^{25,26,27,28,30,31}Al) are all within a few percent in agreement with the USD value. Also the excitation spectrum of ^{31}Al can be very well explained without taking into account intruder states [66]. Further, the recent β-decay study of $^{31}Mg \rightarrow^{31} Al$, showing a very weak feeding to the first excited $1/2^+$ level from the $1/2^+$ 2p-2h intruder ground state of ^{31}Mg, supports the 'normal' character of this level [67].

$^{32}_{13}\mathbf{Al}_{19}$

Just filling the sub-shells derived from the standard nuclear shell model, gives a $\pi(\mathrm{d}_{5/2})^{-1}\nu(\mathrm{d}_{3/2})^{-1}$ configuration for the ground state of ^{32}Al. Coupling a $5/2^+$ proton hole to a $3/2^+$ neutron hole results in four different J states from 1^+ up to 4^+. Using the parabolic rule, the 1^+ level is predicted to form the ground state while the 4^+, 2^+, 3^+ are respectively the first, second and third excited state. If one does not take into account the fp-shells, no negative parity states can occur in the ^{32}Al spectrum.

The 4 lowest levels have also been observed in deep-inelastic and fragmentation experiments, establishing the 4^+ state as isomeric:

- Robinson et al. [68] discovered an isomeric state at 956 keV in ^{32}Al with a lifetime of 200(20) ns. They have strong arguments, based on the life time of this isomer, that it is a 4^+ state decaying to a 2^+ state at 735 keV. This level ordering is in contrast with the parabolic rule.

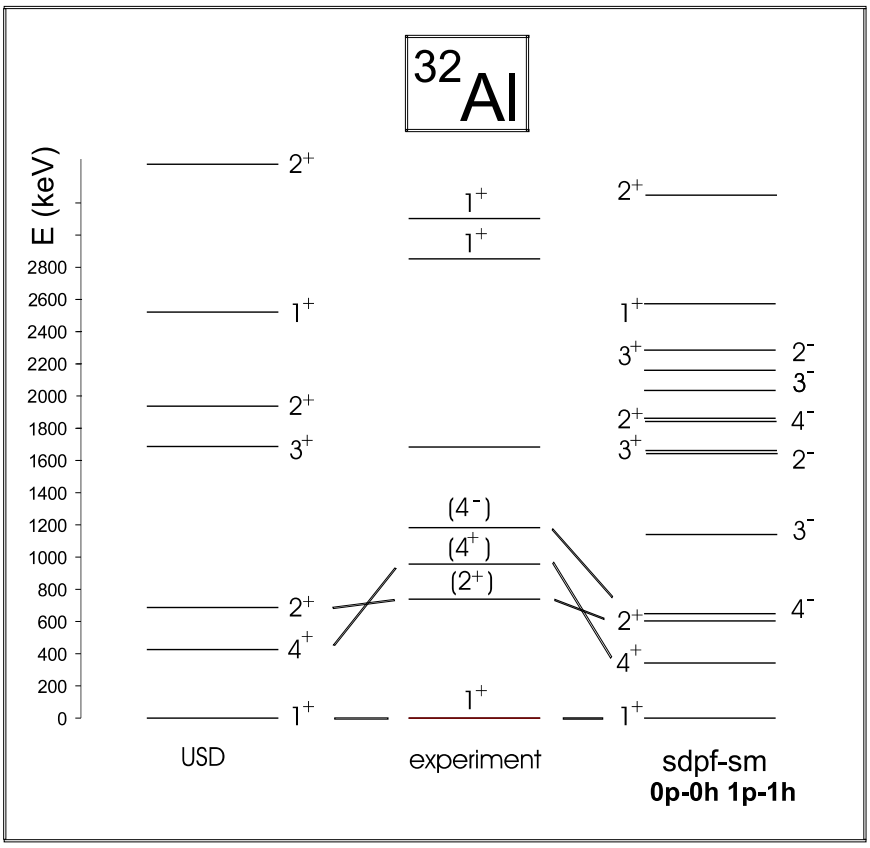

Figure 3.13: Proposed level scheme in ^{32}Al obtained from the β-decay of ^{32}Mg together with theoretical predictions using the USD and the sdpf-sm interaction, with only 1 excitation across N = 20 allowed.

- In deep-inelastic processes during collision of ^{37}Cl ions on a thick ^{208}Pb target, another excited level in ^{32}Al was discovered, at 1178 keV [69]. The 3^+ from the parabolic rule would be the ideal candidate for this level, but if so, a strong 443 keV decay branch to the 735 keV state would be expected to compete with the 222 keV transition, which was not observed. Therefore, it is very likely that this state at 1179 keV is a 4^- excitation and thus a 1p1h configuration.

Grevy et al. [70] studied the β decay of ^{32}Mg. They suggested spin parity assignments of some of the first excited levels. The proposed experimental level scheme as well as theoretical predictions, using the USD and sdpf-sm interaction, are shown in Figure 3.13. Besides underlining the abnormality concerning the sequence of the 2^+ and 4^+ levels, the authors indicate that at 2765 and 3202 keV two 1^+ states are found, while the USD model only predicts one such state around this energy. It is possible that mixing with even particle - even hole states brings down higher lying 1^+ states to this energy. Notice that the calculations using the sdpf-sm interaction show the same abnormality concerning the first 2^+ and 4^+ state. The energy of the 1p-1h 4^- intruder level is in reasonable agreement with the proposed level scheme.

The β-decay of ^{32}Al to ^{32}Si does not show any special features (see Figure 3.14). The main decay branch is to the 0^+ ground state of ^{32}Si, which indicates that it is an allowed transition. The other 15% decays to other 0^+ and 2^+ states.

From all these measurements one can conclude that the low energy spectrum of ^{32}Al is not in agreement with the shell model calculations and no evidence is found that the intruder states influence the ground state.

$^{33}_{13}\mathbf{Al}_{20}$

For a normal N = 20 nucleus, no levels are expected to show up at low energies. The USD interaction predicts the first excited state around 3 MeV, namely the $1/2^+$ dominated by $\pi(s_{1/2})$. Still, Mittig et al. [71] discovered a level at 730(50) keV by studying the inelastic nuclear scat-

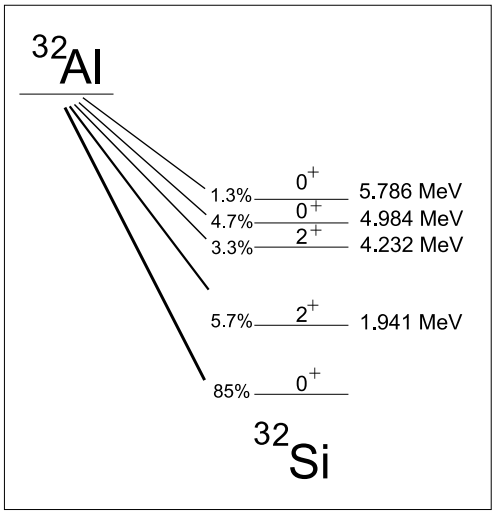

Figure 3.14: ^{32}Al β-decay

tering of ^{33}Al. This is clear evidence that even at low energy ^{33}Al is to some extent influenced by intruder components.

The lifetime and β-decay of ^{33}Al were studied by Morton et al. [72]. A measured life-time of 41.7(2) ms and 89% decay to the ground state are not in disagreement with the theoretical USD prediction of 34.8 ms and 87.7%.

It seems that no clear evidence was found yet to believe that the ground state of ^{33}Al is severely influenced by fp-shell contributions. Still, the MCSM predicts 50% intruder components in the ground state of ^{33}Al. The ANTOINE code with the sdpf-sm interaction claims the pure 0p-0h state to be 647 keV lower than the pure 2p-2h state using the full $\nu(sd-fp)$ shell. This makes ^{33}Al a very interesting case for a g-factor measurement, because the g-factor for a 0p-0h 5/2+ ground state (1.702) is very different from that of a pure 2p-2h ground state (1.398). Allowing 2 excitations across N = 20 in the sdpf-sm interaction, only lowers the g factor from 1.702 to 1.689, indicating only a small admixture of the intruder components into the ground state of ^{33}Al.

$^{34}_{13}\mathbf{Al}_{21}$

Filling the sub-shells with 21 neutrons and 13 protons, a $\pi(d_{5/2})$-hole coupled to a $\nu(f_{7/2})$-particle is suggested as ground state. Of all possible couplings, J = 4^- and 5^- are the lowest based on the parabolic rule. If a 1p-1h state would be the ground state, its spin would be 1^+ or 4^+ as a coupling of $\pi(d_{5/2})$ with $\nu(d_{3/2})$.

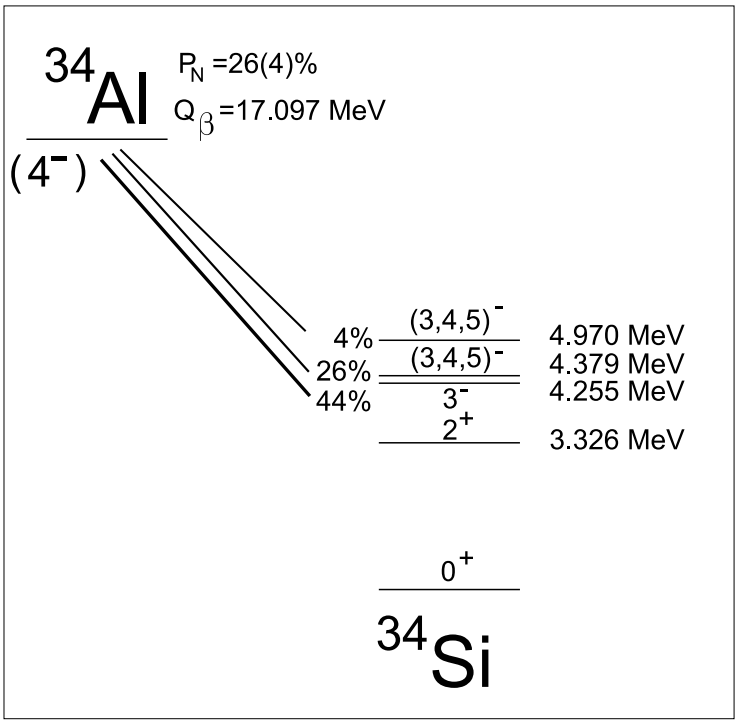

Figure 3.15: ^{34}Al β-decay scheme

It is very unlikely that the spin of the ground state of ^{34}Al is 1^+. In that case, a large β-decay branch to the ground state of ^{34}Si should have been observed. Such a branch was not observed in the decay, measured by Baumann et al. [73] and Nummela et al. [74].

They have shown that 44% of ^{34}Al decays to a level at 4255 keV in ^{34}Si (see Figure 3.15). Assuming 4^- as the ground state spin and parity of ^{34}Al, this level is proposed to be a 3^- because of the combination of the life time of this level (<300ns) and the allowed β-decay ($4^- \rightarrow 3^-$). The theoretical lifetime of a 4^- state, decaying with an M4 transition to the ground state is much longer than the observed lifetime.

Pritychenko et al. [75] studied ^{34}Al via intermediate energy Coulomb excitation and found a first excited state at 657(9) keV and a B(E2) $=100(39)e^2fm^4$. They suggest a 3^- assignment for this first excited state, since $B(E2; 4^- \rightarrow 3^- = 42e^2fm^4)$, while $B(E2; 4^- \rightarrow 2^- = 5.3e^2fm^4)$ and $B(E2; 5^- \rightarrow 3^- = 5.6e^2fm^4)$. Notice that from this measurement a 5^- ground state is not excluded, since $B(E2; 5^- \rightarrow 4^- = 44e^2fm^4)$.

Because of the scarce data on ^{34}Al, it can not yet be concluded whether its ground state is a normal state $(4^-, 5^-)$, a 1p-1h state (4^+) or a mixture of a normal and an even particle - even hole state, although the 4^- spin parity assignment is most plausible.

From a g-factor measurement of the ground state of ^{34}Al, it can be decided whether the 1p-1h state is the ground state or not, since $g_{calc}(4^+) = 1.24$ while $g_{calc}(4^-) = 0.38$ and $g_{calc}(5^-) = 0.35$.

3.6 Si-isotopes (Z = 14)

We have explained before, intuitively, that it is the combination of the monopole energy and the correlation energy that brings the intruder components down in energy. Si has 6 protons in the sd-shell, thus it normally fills up the $\pi(d_{5/2})$ subshell completely. Due to the strong interaction between $\pi(d_{5/2})$ and $\nu(d_{3/2})$, the N = 20 gap becomes larger. Due to the filled proton shell the correlation gain is small. Both features are responsible for the intruder states of Si to be at rather high energy. This is proven experimentally.

$^{33}_{14}\mathbf{Si}_{19}$

From intermediate energy Coulomb excitation of ^{33}Si [76], single neutron knockout from ^{34}Si [77], ^{11}B on ^{36}S at 83 MeV [78], ^{13}C on ^{34}S at 91 MeV [79], and γ-γ coincidence data of ^{160}Gd on ^{37}Cl [80], the following level scheme for ^{33}Si was proposed (Figure 3.16).

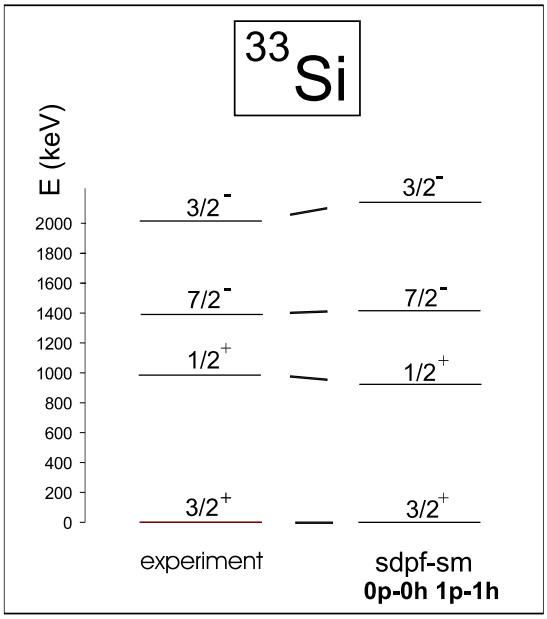

Figure 3.16: Proposed level scheme of ^{33}Si, using the sdpf-sm interaction and only allowing 1 excitation across N = 20.

The relative cross section (of the ^{36}S on ^{11}B reaction) for the ground state, first excited state and the level at 4320 keV agreed with the interpretation of these as the $d_{3/2}$, $s_{1/2}$ and $d_{5/2}$ holes, respectively. From the ^{34}S(^{13}C,^{14}O)^{33}Si reaction the second and third excited states where proposed to be $7/2^-$ and $3/2^-$ respectively. Both are 1p1h excitations, which are in very good agreement with the sdpf-sm calculations. Since the excitation spectrum of ^{35}Si is one of the building blocks of the sdpf-sm interaction, this good correspondence for ^{33}Si is expected.

$^{34}_{14}\mathbf{Si}_{20}$

Both the MCSM and the ANTOINE code predict the ground state of ^{34}Si to be merely a normal 0^+ sd state. They also predict an almost pure 2p-2h 0^+ state as the first excited state around 2 MeV. Although several experiments were carried out to find this second 0^+ state, it was not observed up to now [71] [81].

The B(E2) value of the transition of the first 2^+ state at 3326 keV to the ground state was measured to be 85(33) e^2fm^4 [82]. This value is not in agreement with the USD value, but is considerably lower as shown in Figure 3.5. This does not mean that the ground state of ^{34}Si is influenced by intruder components. Making the MCSM calculations it is predicted that the structure of the ground state of ^{34}Si is still dominated by the normal configuration and it's first excited 2^+ state is an almost pure 2p-2h state. The overlap of these wave functions is very small, explaining the small B(E2) value connecting these states. Since the first 2^+ state in the USD model has a normal configuration, the B(E2) value from the USD calculation is higher than the experimental value.

$^{35}_{14}\mathbf{Si}_{21}$

The ground state is determined by the odd neutron in the $f_{7/2}$ subshell. The excited state at 910 keV is the $3/2^-$ level coming from the odd neutron in $p_{3/2}$ and the first 1p-1h state is a $3/2^+$ at 974 keV [74] [24].

^{35}Si is a very interesting nucleus from the point of view of sd-fp shell model calculations. In the mass region just above N = 20, some key nuclei having a simple structure play a major role for the determination of the interaction: these are the Z = 19 $^{39-41-43-45-47}$K and the N = 21 ^{31}Ne, ^{33}Mg,^{35}Si,^{37}S,^{39}Ar, ^{41}Ca nuclei. The energy of the $3/2^+$,$1/2^+$ and $5/2^+$ levels in the K isotopes give information on the behavior of the single particle energy of the $\pi(d_{5/2})$, $\pi(s_{1/2})$ and $\pi(d_{3/2})$ from N = 20 to N = 28. The energy of the $7/2^-$ and $3/2^-$ levels in ^{31}Ne, ^{33}Mg,^{35}Si,^{37}S,^{39}Ar, ^{41}Ca give information on the behavior of the single particle energy of the $\nu(f_{7/2})$ and $\nu(p_{3/2})$ from Z = 8 to Z = 20.

Taking into account the spectroscopy data from ^{35}Si, the sdpf interaction was slightly modified and renamed as sdpf-sm interaction as mentioned before. Figure 3.17 shows that the prediction of the energy of the 3/2- level in ^{35}Si is more than 1 MeV higher than the experimental value, using the sdpf interaction.

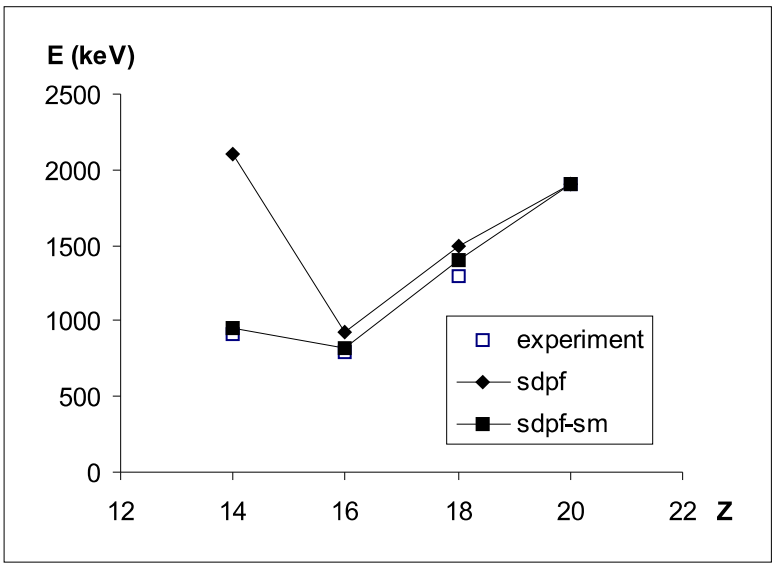

Figure 3.17: Evolution of the experimental and theoretical $3/2^-$ excitation energy in N = 21 isotones. After the observation of the $3/2^-$ state in ^{35}Si, the sdpf interaction was changed and renamed as sdpf-sm.

Notice that for instance from the energy difference between the $7/2^-$ ground state and the first $3/2^-$ excited state in ^{35}Si the single particle energy difference between $\nu(f_{7/2})$ and $\nu(p_{3/2})$ can be derived, if the wave function of both states is predicted correctly. By measuring the ground state g-factor of ^{35}Si, this can be verified already for the ground state.

The location of the observed single-particle states in ^{35}Si can be interpreted as a reduction of the neutron gap between the $f_{7/2}-p_{3/2}$ shells. This can be explained by an erosion of the spin-orbit force far from sta-

bility, since this gap finds its origin in the splitting of $f_{7/2} - f_{5/2}$ due to the spin-orbit force. This erosion is moderate for ^{35}Si but is interesting in particular going from the N = 20 Z = 13 region to the N = 28 Z = 20 region.

3.7 Conclusion

Figure 3.18 makes an overview of the present experimental situation in the region of the island of inversion. The ground states of certain nuclei are certainly severely influenced by intruder states: ^{30}Ne, $^{29-30-31-32}$Na, $^{31-32-33-34}$Mg. Of some other $N < 22$ nuclei on this part of the chart, it is quite sure that all nuclear properties of the ground state can be explained with the WBMB interaction, not taking into account intruder components: ^{26}Ne, ^{28}Na, ^{31}Al, $^{33-34-35}$Si.

One notices that some nuclei are still undecided. They form the borders of the island of inversion. As shown before, the recent shell model calculations can describe the ground state properties of the most general cases embedded inside the island of inversion, such as ^{31}Na (Z = 11) and ^{32}Mg (Z = 12), and also nuclei far out of the island, such as ^{34}Si (Z = 14) and ^{31}Al. It is at the edge of the island of inversion that the different models give different predictions: the MCSM with the SDPF-M interaction predicts a 50% mixed ground state for ^{33}Al, while the ANTOINE code with the sdpf-sm interaction suggests a low amount of mixing. In order to come to a correct parametrization of the shell model, a good understanding of the island of inversion and a correct prediction of its border along Z, one needs accurate experimental data from these nuclei, which is the goal of this thesis.

Z = 14	Si	30	31	32	33	34	35	
Z = 13	Al	29	30	31	32	33	34	
Z = 12	Mg	28	29	30	31	32	33	34
Z = 11	Na	27	28	29	30	31	32	
Z = 10	Ne		27	28	29	30		
Z = 9	F			27		29		
N =		16	17	18	19	20	21	22

Figure 3.18: Part of the nuclear chart around the island of inversion. Nuclear properties of the ground state of nuclei in light grey can be explained without intruders. Some experimental properties are in serious disagreement with the WBMB interaction for the dark grey nuclei and this is explained by including intruder configurations into their wave function. The white nuclei are undetermined.

Chapter 4

Set-up and technique

The major topic of this thesis work is the interpretation of the measured nuclear gyromagnetic ratio (or g-factor) of some exotic β-decaying nuclei.

We will first discuss how these nuclei are produced and how they are guided to the experimental set-up. Then a description of the β-Nuclear Magnetic Resonance (β-NMR) set-up is made.

In a second part, the topics 'polarisation' and 'g-factor' are introduced and an explanation (both general and mathematical) is given of the method to measure this nuclear property, the so called β-NMR technique. A discussion is made on how to use this technique optimally i.e. how to destroy all polarisation in order to see the largest effect in the NMR curve.

In the last part of this chapter, the experimental procedure which we followed to measure the g-factor of rarely produced exotic isotopes is described.

4.1 Production and set-up

4.1.1 Production

The observed Al, Si and Mg isotopes are neutron rich, light, exotic nuclei. They are produced and oriented by a fragmentation reaction or a pick-up reaction at the Grand Accélérateur National d'Ions Lourds (GANIL, Caen, France). A schematic overview of this facility is shown in Figure 4.1.

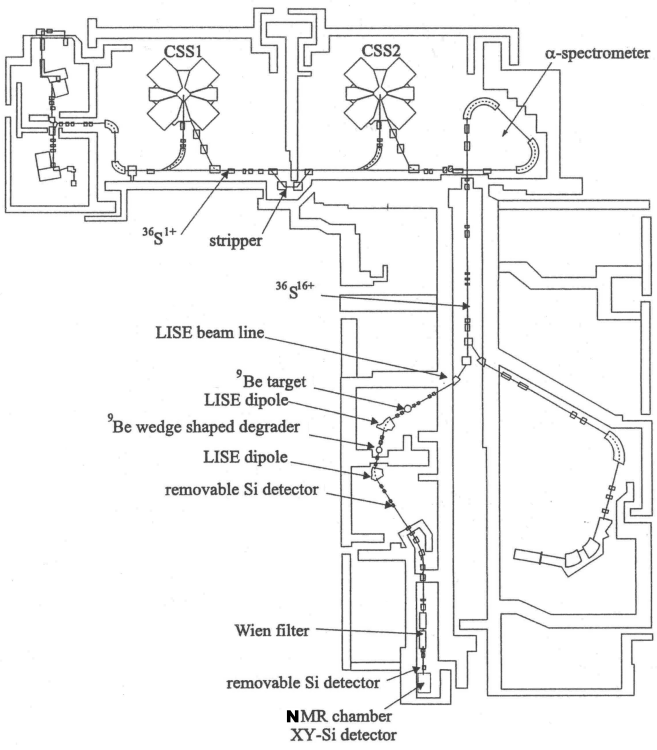

Figure 4.1: Overview of the experimental hall of GANIL. Two silicon detectors are put in the beam line, one after the LISE spectrometer and one before the NMR setup. In the chamber a position sensitive silicon detector was installed.

A primary beam of $^{36}S^{16+}$ with an intensity around 2μA is accelerated by two segmented cyclotrons (Cyclotrons à Secteurs Séparés: CSS1 and CSS2) to 77.5MeV/u and directed to the LISE beam (Ligne d'Ions Super Epluchés) via the α-spectrometer. At LISE, the beam is bombarding a rotating ^{9}Be target (thickness $\sim$ 1 mm).

The 2 LISE dipoles together with the wedge degrader halfway these two magnets, permit a selection of the secondary fragment beam according to their charge state, speed and mass of the isotope of interest.

The determination of the magnetic rigidity Bρ of the first dipole is a measurement of the deviation of the beam according to the mass to charge ratio of the isotopes as well as their velocity:

$$B\rho = \frac{A\gamma\beta}{3.1071q} \tag{4.1}$$

with B the magnetic field in [T], ρ the radius of the bending in [m], q the charge of the ion, $\beta = v/c$ with v the velocity of the nucleus in [m/s] and $\gamma = 1/\sqrt{1-\beta^2}$. This first dipole selects only nuclei with a certain A/Z ratio.

The degrader, situated in the intermediate focal plane, purifies the secondary beam composed of several ions with different charge state. The energy loss (and consequently also the decrease in velocity) in the degrader is a characteristic of the ions with a specific mass A and atomic number Z:

$$\frac{dE}{E} \cong eK\frac{A^3}{Z^2} \tag{4.2}$$

with e the thickness of the degrader, K a constant associated with the degrader. Since the second dipole makes another velocity selection, the degrader in combination with the second dipole, makes an extra A^3/Z^2 selection.

The final identification of the fragments and the purity of the secondary beam was achieved by energy-loss and time-of-flight measurements using Si detectors both at the intermediate (after wedge) and final focal planes in the beam line. The Si detectors were taken out of

the beam after the ion identification in order to avoid straggling effects and the pick-up of electrons by the fully stripped fragments, which could reduce the reaction induced spin-orientation significantly. The beam is further guided to the NMR chamber, to be implanted in a suitable crystal.

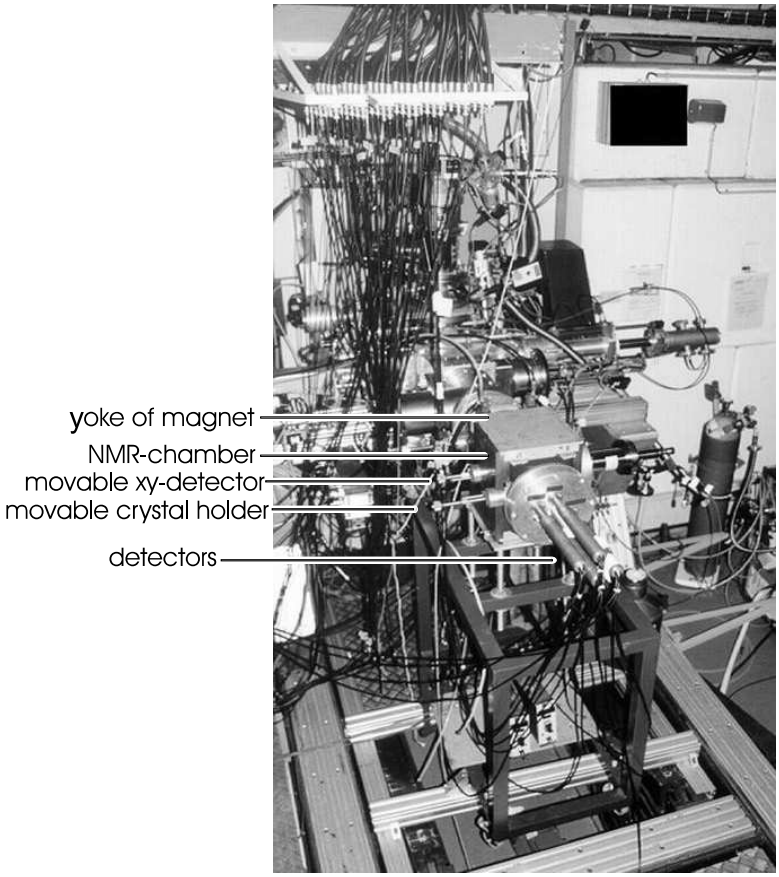

Figure 4.2: Outside of the NMR-chamber - the beam comes from the left

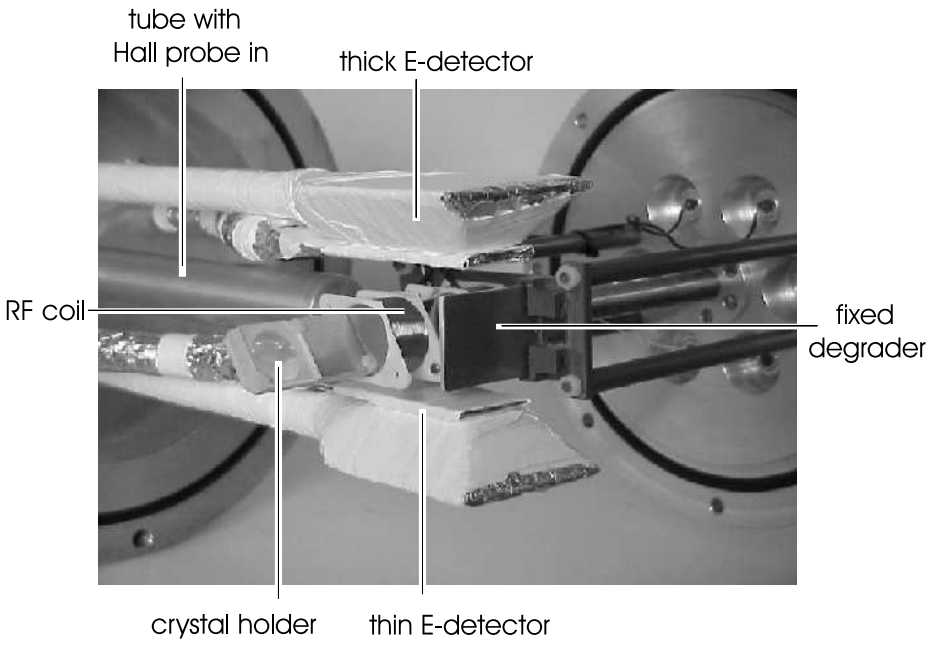

Figure 4.3: Inside of the NMR-chamber - the beam comes from the right

4.1.2 NMR set-up

At the entrance of the NMR-chamber a collimator of 14 mm diameter is placed such that the beam only hits the crystal which has a minimal diameter of 20 mm.

The NMR set-up (Figure 4.2 and 4.3) consists of a vacuum chamber in which 4 20x20x2 mm^3 crystals can be entered on a movable crystal holder. Notice that the crystal holder is tilted by 30^o, because this angle gives less scattering than a vertical position, according to GEANT simulations. A fixed degrader of 2.00 mm thickness is put directly in front of the stopper crystal, in order to minimize the straggling when reducing the beam energy. Finetuning of the fragment energy is done using degraders placed 40 cm upstream, with variable thicknesses between 0 and 1200 μm.

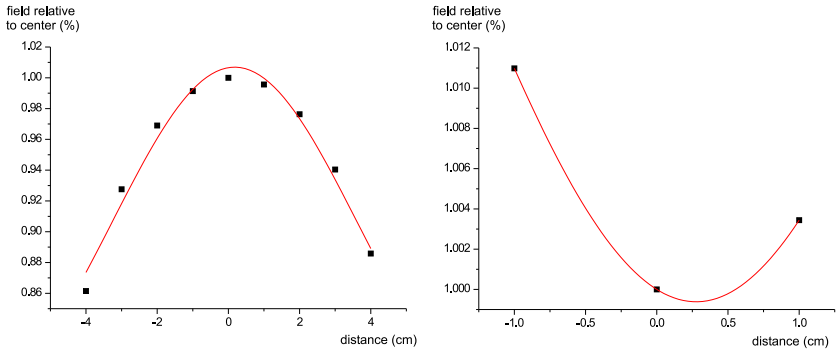

Figure 4.4: (left) Field profile in horizontal direction - (right) Field profile in vertical direction

Two coils around this vacuum chamber provide a vertical static magnetic field B_0, parallel to the direction of polarisation, in order to keep the orientation as will be shown in the next chapter. The magnetic field is measured with a Hall Probe at 7 cm from the crystal, the read-out being integrated in the data acquisition system. To calibrate B_0, prior to each run, the linear relation between B_{exp} and B_{center} is deduced, with B_{center} the static magnetic field at the place of the stopper crystal and B_{exp} the field measured at 7 cm from the center. It has to be noted that the relation is slightly different in every experiment, since the Hall Probe is not put at exactly the same place every time. For each experiment, its own calibration is used to deduce the g-factor.

The magnet can produce positive and negative static magnetic fields up to 0.18 T. The results of an accurately measured field profile show that the produced static magnetic field varies strongly over the beam spot area (diameter: 14 mm) on the stopper crystal. It is shown in Figure 4.4 that at the extremes of the beam spot, a difference with the center value of 0.4% in the vertical and 0.5% in the horizontal direction is measured. This inhomogeneity will influence the linewidth and amplitude of the observed resonances and will limit the accuracy of the measured g-factors. This will be explained in Chapter 6.

Symmetrically above and below the crystal, β-scintillator telescopes, referred to as E_{up} and E_{down}, are placed inside the vacuum chamber to detect the emitted β-particles. Each telescope consists of a 2 cm thick scintillator crystal, allowing to stop β-particles up to $\sim$6 MeV (E-detector) and a 2 mm thin scintillator ΔE. Only events detected in coincidence are taken into account in order to deduce random noise counting, but mainly to eliminate signals from γ-rays which give a signal in the E detector, but not in the ΔE, since the energy deposition in the latter one is too small. N_{up} (N_{down}) represents the number of coincident events in the Up (Down) detector.

The scintillators are connected via a plexiglass lightguide through a vacuum connection to the photomultipliers (type: R7600U Hamamatsu) which are outside the vacuum.

A coil, made of 66 turns of a 0.1 mm Cu wire with a diameter of 2.3 cm and $L \simeq 1\mu H$, which is part of a series LRC circuit, with capacitors of around 100nF, is placed around the implantation crystal to induce a radio-frequent (RF) field, with certain frequency ν_{RF}. The generated RF-strength is $\sim$1 gauss. For one capacitor settings, the FWHM of the generated power curve is $\sim$100kHz. Using variable capacitors, a frequency range from 250 to 1600 kHz can be reached with the present system.

4.2 The gyromagnetic ratio

The gyromagnetic ratio (or g-factor) is linked to the better known magnetic moment in the following way: $\mu = gI\mu_N$

Experimental magnetic moments are always expressed in units of nuclear magneton μ_N. Knowing the spin of the nuclear state and the measured g-factor, the magnetic moment is obtained from the formula above. Note that some experimental methods measure the magnetic moment and others the g-factor.

The magnetic operator $\bar{\mu} = g_l \bar{l} + g_s \bar{s}$ is a one-body operator and the magnetic moment is the expectation value of $\bar{\mu}_z$. The M1 operator acting on a composed state $|I, m>$ can then be written as the sum of single particle M1 operators $\bar{\mu}_z$(j) acting each on an individual valence nucleon with total momentum j (with $\bar{j} = \bar{l} + \bar{s}$):

$$\mu(I) = \left\langle I(j_1, j_2, \ldots, j_n), m = I \left| \sum_{i=1}^{n} \hat{\mu}_z(i) \right| I(j_1, j_2, \ldots, j_n), m = I \right\rangle \tag{4.3}$$

The single particle moment μ(j) for a valence nucleon around a doubly magic core is uniquely defined by quantum numbers l and j of the occupied single particle orbit [83].

$$\begin{aligned} &\text{for } j = l + \tfrac{1}{2}: \quad \mu = \left(g_l \left(j - \tfrac{1}{2} \right) + \tfrac{1}{2} g_s \right) \mu_N \\ &\text{for } j = l - \tfrac{1}{2}: \quad \mu = \left(g_l \tfrac{j\left(j+\frac{3}{2}\right)}{j+1} - \tfrac{1}{2(j+1)} g_s \right) \mu_N \end{aligned} \tag{4.4}$$

These single particle moments calculated using the free nucleon values for g_l and g_s (i.e. $g_l^\pi = 1$, $g_l^\nu = 0$ and $g_s^\pi = 5.587$, g_s^ν = -3.826) are called 'the Schmidt moments'. In a realistic nucleus, the valence nucleons can not be considered as free particles, due to which the free nucleon values do not always give good agreement with experimental g-factors.

In certain regions of the nuclear chart, it is shown by thorough comparison between theory and experiment, that the free g-factors do give reasonable agreement with theory. Brown and Wildenthal [84] found that the free nucleon g factors give no obviously deviating magnetic moments in the $8 \leq N, Z \leq 20$ region close to the line of stability using the USD interaction. The same conclusion was drawn for the KB3G interaction [85], which is the interaction used to describe the full pf-nuclei and used with the Antoine code. Honma et al. [86] come to the same conclusion for the GXPF1 interaction (the most recent interaction for the $47 < A < 66$ region used with the MCSM code).

Because the magnetic moment operator is a one-body operator, it allows one to deduce some general 'additivity' rules for the magnetic

moment of a 'composed' nuclear state, provided that it can be described, in a simple model, with a few particles (and/or holes) around an inert core. For a nuclear state described by a weak coupling between protons and neutrons, the magnetic moment can be calculated as:

$$\mu(J) = \frac{J}{2}[\frac{\mu(J_\pi)}{J_\pi} + \frac{\mu(J_\nu)}{J_\nu} + (\frac{\mu(J_\pi)}{J_\pi} - \frac{\mu(J_\nu)}{J_\nu})\frac{J_\pi(J_\pi+1) - J_\nu(J_\nu+1)}{J(J+1)}] \tag{4.5}$$

Nuclear magnetic moments are almost completely determined by the orbits that are occupied by the valence particles (or holes). They thus provide a good test for the purity of a particular configuration.

Magnetic moments are very sensitive to mixing spin-flip matrix elements into the wave function, e.g. configurations of the type $\mid \pi(j_> j_<); 1^+ >$, with $j_> = l + 1/2$ and $j_< = l - 1/2$, called first-order core polarization effects, will strongly influence the magnetic moment (thus contributing little to the wave function, but still having a remarkable influence on the magnetic moments of these states).

On the other hand, the magnetic moment is less sensitive to nuclear deformation and to second-order core polarization (particle-core coupling and mixing with 2p-2h excitations). In order to find evidence for such 2p-2h excitations via the magnetic moment, the measurements should be very precise. As explained in the second Chapter, magnetic moments gave conclusive information on the even particle-even hole intruder character of ^{30}Na and ^{31}Na.

4.3 NMR method: theory

4.3.1 General

The Nuclear Magnetic Resonance (NMR) method on β-decaying nuclei is a well understood technique to measure the g-factor of the ground states of radioactive nuclei [87] [88].

A necessity to measure a g-factor of an ensemble of nuclei with the NMR technique is the presence of spin-polarisation in the implanted ensemble of nuclei. If the spins of a nuclear ensemble have a certain preferred direction in space, this ensemble is spin oriented. The orientation axis Z is defined as the symmetry-axis if the orientation is axially symmetric around this preferred direction. Two distinctions of orientation exist: alignment and polarisation. If $p_m(t)$ is the probability that the projection of I on Z is $|m>$ at time t, an ensemble is referred to as aligned if $p_m(t) = p_{-m}(t)$ for all m and polarised if at least for 1 m $\neq 0$ $p_m(t) \neq p_{-m}(t)$.

The amount of alignment/polarisation for a nuclear ensemble with spin I is defined as [89]:

$$A_I(t) = \sum_m \frac{[3m^2 - I(I+1)]p_m(t)}{I(I+1)} \tag{4.6}$$

$$P_I(t) = \frac{1}{I}\sum_m m p_m(t) \tag{4.7}$$

The β-decay pattern of an oriented nuclear ensemble is not isotropic. Assuming a polarised and axial symmetric ensemble, the angular distribution for allowed β-decay ($\Delta I = -1, 0, +1$ and no parity change) can be calculated to first order as follows:

$$W(\theta, t) = 1 - A_1\sqrt{\frac{3I}{I+1}}P_I(t)cos(\theta) \tag{4.8}$$

with θ the detection angle with respect to the Z - axis, which is defined downwards in our experiments, and A_1 the asymmetry parameter. Formula 4.10 is used to calculate A_1.

$$\begin{aligned}
&\text{if } I_f = I_i - 1: \quad A_1(\beta^{\pm}) = \mp\tfrac{v_\beta}{c}\sqrt{\tfrac{I_i+1}{3I_i}} \\
&\text{if } I_f = I_i + 1: \quad A_1(\beta^{\pm}) = \pm\tfrac{v_\beta}{c}\sqrt{\tfrac{I_i}{3(I_i+1)}} \\
&\text{if } I_f = I_i \neq 0: \quad A_1(\beta^{\pm}) = \tfrac{v_\beta/c}{1+y^2}[\tfrac{\mp 1}{\sqrt{(3I_i(I_i+1)}} + \tfrac{2}{\sqrt{3}}y]
\end{aligned} \tag{4.9}$$

with $y = \frac{C_V M_F}{C_A M_{GT}}$ the Fermi/Gamow-Teller mixing ratio with C_V = 1.00, C_A = -1.27 being the vector, respectively the axial vector coupling constants. From Formula 4.9 it follows immediately that the β-decay is isotropic if $P_I(t) = 0$ and anisotropic if $P_I(t) \neq 0$.

The spin polarised nuclei are implanted in a crystal with cubic lattice symmetry, in which the nuclei do not undergo an electric field gradient. The static magnetic field B_0 induces the Zeeman splitting of the nuclear hyperfine levels. The energy difference between all sublevels m_1 and m_2 with $|m_1\text{-}m_2| = 1$, is equal and depends on the g-factor and the static magnetic field ($\Delta E = g\mu_N B_0$), as shown in Figure 4.5.

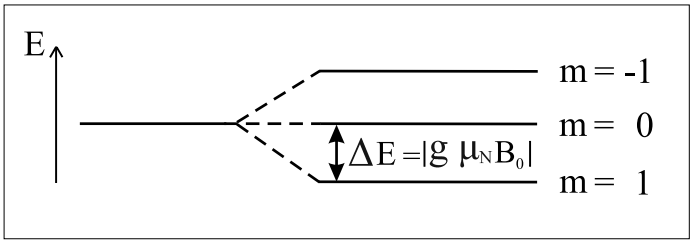

Figure 4.5: The substates are degenerate without external magnetic field (left) and the degeneracy is removed with applied field (right), resulting in an equidistant level splitting.

Perpendicular to B_0, a linearly polarised oscillating magnetic field, with amplitude B_1 and frequency ν_{RF}, is provided by the LRC circuit. Each applied rf frequency was modulated continuously around a fixed value over a modulation range δ.

If the Zeeman splitting ($g\mu_N B_0$) equals the energy of the oscillating magnetic field ($h\nu_{RF}$), the population of the sublevels will mix and the polarisation is lost, which means that at this resonance condition $W(\theta,t)$ will suddenly change from $W(\theta,t) \neq 1$ to $W(\theta,t) = 1$ and

$$(\frac{W(180^0)}{W(0^0)})_{in-resonance} = 1 \tag{4.10}$$

This change can be observed by measuring the β-asymmetry, deduced via the two β-detectors, placed close to the crystal at $\theta = 0^0$ and 180^0 and defined as A=N_{UP}/N_{DOWN}, with N_X the number of particles detected in the X detector:

$$A_{in-resonance} = (\frac{N_{up}}{N_{down}})_{in-resonance} = \epsilon(\frac{W(180^0)}{W(0^0)})_{in-resonance} = \epsilon \tag{4.11}$$

with ϵ, the experimental asymmetry of the set-up, due to different efficiency of both detectors, a non-centered beamspot, anisotropic scattering,...

The difference in β-asymmetry between in and out of the resonance condition, reflects the amount of polarisation in the ensemble:

$$\frac{(A)_{in-resonance} - (A)_{out-resonance}}{(A)_{in-resonance}} \tag{4.12}$$

$$= \frac{\epsilon(\frac{W(180^0)}{W(0^0)})_{in-resonance} - \epsilon(\frac{W(180^0)}{W(0^0)})_{out-resonance}}{\epsilon(\frac{W(180^0)}{W(0^0)})_{in-resonance}} \tag{4.13}$$

$$= \frac{\epsilon - \epsilon\frac{1+A_1\sqrt{\frac{3I}{I+1}}P_I}{1-A_1\sqrt{\frac{3I}{I+1}}P_I}}{\epsilon} = 2A_1\sqrt{\frac{3I}{I+1}}P_I \tag{4.14}$$

Searching for this resonance condition can be done in 2 ways: changing B_0 gradually (called field scan), or changing ν_{RF} (called frequency scan). Both methods are used in this thesis work to derive the g-factor from the resonance condition ($g = \frac{h\nu}{\mu_N B}$).

4.3.2 Mathematical

Since the investigated nuclei are very exotic, the production rate is low. The β-count rate for ^{34}Al is for instance around 75 per second per detector. Next to this problem, the obtained beam time at large accelerator facilities is limited and thus it has to be used efficiently.

It will be shown in the next chapter that the production of polarisation is very well understood and can be optimised in both reaction types used in this thesis work.

A second crucial factor is the polarisation that can be maintained for several nuclear lifetimes, since this is the maximum amount that can be destroyed. The optimal conditions to preserve polarisation are discussed in the next chapter as well.

A third crucial factor is the amount of polarisation that is destroyed. This value is linearly proportional to the effect observed in the NMR resonance. Notice that four times better statistics is needed to observe an effect that is twice smaller. It is thus necessary to find out what are the conditions on nuclear lifetime, RF power, modulation frequency,... to observe the maximal effect in the NMR curve.

These conditions can be pinned down by making a mathematical derivation of the NMR curve starting from the NMR Hamiltonian. From this, we can give answers to questions such as: How important is the applied RF power? Is it important to have a very homogenous static magnetic field? Should a nucleus have a minimal/maximal life time to be able to perform a NMR measurement? Why is it better to modulate the RF frequency and how much should it be modulated? How can these limits be influenced?

The main goal of this derivation is to find out what are the crucial conditions for efficient NMR measurements by developing a formalism to make simulations on a case by case basis. This mathematical model has then also been used to fit the data described in Chapter 6.

Analytic

The Hamiltonian of the NMR system with the Z-axis along B_0 is [87]

$$H_{NMR}(t) = \omega_B I_z + \omega_1(cos\theta(t)I_X + sin\theta(t)I_Y) \tag{4.15}$$

with $\omega_B = -\frac{g\mu_N B_0}{\hbar}$ proportional to the Larmor frequency ($\nu_{Larmor} = |\frac{\omega_B}{2\pi}|$), $\omega_1 = -\frac{g\mu_N B_1}{\hbar}$ proportional to the Rabi oscillation frequency ($\nu_{Rabi} = |\frac{\omega_1}{2\pi}|$) and $\theta(t) = \omega_{RF}(t)t$. The first part represents the static magnetic field, the second the oscillating magnetic field (RF field) composed of a right and left circularly polarized component. $\nu_{RF} = \frac{\omega_{RF}}{2\pi}$ is the frequency of the oscillating field.

In our experiments ν_{RF} is not constant during 1 step (of typical 1 minute in case of a field scan and 10 seconds for frequency scans) but changes in time between 2 extreme values $[\nu_{RF}-\delta, \nu_{RF}+\delta]$ with a typical 'sweep frequency' ν_{mod} of 100Hz as shown in Figure 4.6. This frequency modulation will prove to be crucial for efficient and fast search for the resonance condition.

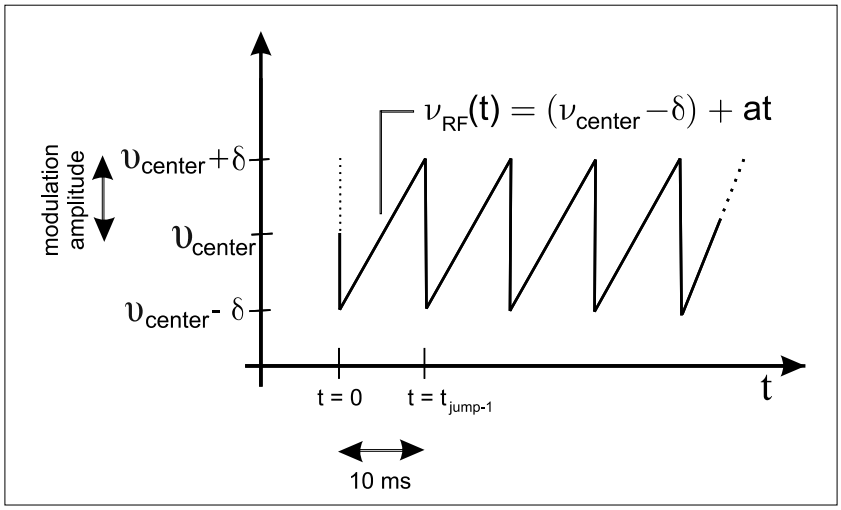

Figure 4.6: The time dependence of the oscillating field around $\nu_{center} = \frac{\omega_{center}}{2\pi}$.

If no frequency modulation is applied $\nu_{RF}(t)$ does not depend on time and the Hamiltonian becomes time-independent after a unitary transformation $U(t) = e^{\frac{iI_z\theta(t)}{\hbar}}$ [87]:

$$H'_{NMR} = [\omega_B - \omega_{RF}]I_{Z'} + \omega_1 I_{X'} \tag{4.16}$$

This formula shows that the mixing element is proportional to the amplitude of the oscillating field B_1(= the RF strength). The more the Larmor frequency ($\nu_{Larmor} = \frac{|\omega_B|}{2\pi} = |\frac{g\mu_N B_0}{h}|$) approaches the oscillating field frequency (ν_{RF}), the smaller the first term and the more important the mixing element becomes. This indicates mathematically that the mixing is maximal (and consequently the destruction of orientation) if $\nu_{RF} = \nu_{Larmor}$. This equation is called the resonance condition, from which the g-factor can be deduced:

$$g = \frac{h\nu_{RF}}{\mu_N B_0} \tag{4.17}$$

Due to this unitary transformation, the Hamiltonian becomes time-independent, which makes it possible to obtain the time evolution of this system by solving the Von Neumann-equation,with $\rho(I)$ the nuclear density operator:

$$\frac{\delta}{\delta t}\rho(I,t) = -\frac{i}{\hbar}[H(t), \rho(I,t)] \tag{4.18}$$

Using some tensor-rotations, this solution can be transferred back to the LAB-system, where it still has to be time-integrated in order to obtain W(θ). This is described in more detail in [90].

In case of a field scan W(θ) is calculated for each ω_B (or ν_{Larmor}). In case of a frequency scan W(θ) is calculated for each ω_{RF} (or ν_{RF}). Using formula 4.8 and 4.14 the NMR curve can be simulated.

Numeric

If ν_{RF} is modulated, the above theory is not valid, because the used unitary transformation does not make the Hamiltonian time independent (since ν_{RF} is time dependent in this case) and consequently the time

evolution can not be obtained via solving the Von Neumann equation. No mathematical treatable transformation is found which allows an analytic solution to the problem. We thus search for an other method to obtain $W(\theta, t)$.

To make the mathematical derivation synoptic, we limit this derivation to nuclei with I = 1/2. In this case, only 2 substates exist: m = +1/2 and m = -1/2. Using these states as basis, the wave function of a nucleus can be expressed for all times:

$$\mid \Psi(t) >= c_{+1/2}(t)e^{\frac{itE_{+1/2}}{\hbar}} \mid +1/2 > +c_{-1/2}(t)e^{\frac{itE_{-1/2}}{\hbar}} \mid -1/2 > \quad (4.19)$$

with $\mid c_x(t) \mid^2$ the probability that the nucleus is in state x at time t. Denote that $c_x(t)$ is complex and can be written as $c_x(t) = a_x(t)+ib_x(t)$. In order to obtain the time evolution of this system, the Schrodinger equation needs to be solved:

$$i\hbar\frac{\delta \mid \Psi(t) >}{\delta t} = H \mid \Psi(t) > \quad (4.20)$$

Using the Hamiltonian of equation 4.15, this results in 4 differential equations.

$$\begin{aligned}
-\dot{b}_{+1/2} &= A(a_{-1/2}cos((\omega_{RF}(t) - \omega_B)t) - b_{-1/2}sin((\omega_{RF}(t) - \omega_B)t)) \\
\dot{a}_{+1/2} &= A(a_{-1/2}sin((\omega_{RF}(t) - \omega_B)t) + b_{-1/2}cos((\omega_{RF}(t) - \omega_B)t)) \\
-\dot{b}_{-1/2} &= A(a_{+1/2}cos((\omega_{RF}(t) - \omega_B)t) + b_{+1/2}sin((\omega_{RF}(t) - \omega_B)t)) \\
\dot{a}_{-1/2} &= A(-a_{+1/2}sin((\omega_{RF}(t) - \omega_B)t) + b_{+1/2}cos((\omega_{RF}(t) - \omega_B)t))
\end{aligned} \quad (4.21)$$

with $|A| = |\frac{g\mu_N B_1}{2\hbar}| = \frac{2\pi\nu_{Rabi}}{2}$, dependent on B_1 (= the RF strenght) and the g-factor.

If $\omega_{RF} \neq \omega_B$ and time-dependent, the 4 differential equations do not have an analytic solution. Many different techniques exist to solve a system of differential equations of first order to find the probability

coefficients as function of time. The Runge-Kutta Method was used to derive the time evolution of $c_{-1/2}(t)$ and $c_{+1/2}(t)$. Up to $t = 10\tau$, with τ the lifetime of the nucleus, this method is used in the following manner to calculate $c_i(t)$ every $t_i = t_{i-1} + h$ with h = 10ns.

The first derivatives of $a_{1/2}$, $b_{1/2}$, $a_{-1/2}$ and $b_{-1/2}$ can be written as a function of t, $a_{1/2}$, $b_{1/2}$, $a_{-1/2}$ and $b_{-1/2}$:

$$\begin{aligned}
\dot{b}_{+1/2} &= f(t, b_{1/2}(t), a_{1/2}(t), b_{-1/2}(t), a_{-1/2}(t)) \\
\dot{a}_{+1/2} &= g(t, b_{1/2}(t), a_{1/2}(t), b_{-1/2}(t), a_{-1/2}(t)) \\
\dot{b}_{-1/2} &= j(t, b_{1/2}(t), a_{1/2}(t), b_{-1/2}(t), a_{-1/2}(t)) \\
\dot{a}_{-1/2} &= k(t, b_{1/2}(t), a_{1/2}(t), b_{-1/2}(t), a_{-1/2}(t))
\end{aligned} \tag{4.22}$$

The values of $a_{1/2}$, $b_{1/2}$, $a_{-1/2}$ and $b_{-1/2}$ can be obtained at time step n+1 ($t_{n+1} = t_n + h$ with $h = 10ns$) from the values at t_n:

$$\begin{aligned}
b_{+1/2}(t_{n+1}) &= b_{+1/2}(t_n) + \tfrac{1}{6}(f_1 + 2f_2 + 2f_3 + f_4) \\
a_{+1/2}(t_{n+1}) &= a_{+1/2}(t_n) + \tfrac{1}{6}(g_1 + 2g_2 + 2g_3 + g_4) \\
b_{-1/2}(t_{n+1}) &= b_{-1/2}(t_n) + \tfrac{1}{6}(j_1 + 2j_2 + 2j_3 + j_4) \\
a_{-1/2}(t_{n+1}) &= a_{-1/2}(t_n) + \tfrac{1}{6}(k_1 + 2k_2 + 2k_3 + k_4)
\end{aligned} \tag{4.23}$$

with

$$\begin{aligned}
f_1 &= hf(t_n, b_1(t_n), a_1(t_n), b_2(t_n), a_2(t_n)) \\
f_2 &= hf(t_n + h/2, b_1(t_n) + f_1/2, a_1(t_n) + g_1/2, b_2(t_n) + j_1/2, a_2(t_n) + k_1/2) \\
f_3 &= hf(t_n + h/2, b_1(t_n) + f_2/2, a_1(t_n) + g_2/2, b_2(t_n) + j_2/2, a_2(t_n) + k_2/2) \\
f_4 &= hf(t_n + h, b_1(t_n) + f_3, a_1(t_n) + g_3, b_2(t_n) + j_3, a_2(t_n) + k_3) \\
g_1 &= ...
\end{aligned} \tag{4.24}$$

Because a NMR measurement is a time integrated measurement, these coefficients have to be integrated according to the formula below:

$$\mid c_x(averaged) \mid^2 = \frac{1}{\tau}\int_0^{\infty} e^{-t/\tau} \mid c_x(t) \mid^2 dt \simeq \frac{1}{\tau}\int_0^{10\tau} e^{-t/\tau} \mid c_x(t) \mid^2 dt \tag{4.25}$$

with τ the lifetime of the nucleus. The polarisation in these conditions can now be calculated with Formula 4.8:

$$P = \frac{1}{2}(\mid c_{-1/2}(averaged) \mid^2(-1/2) + \mid c_{1/2}(averaged) \mid^2(1/2)) \tag{4.26}$$

In case of a field scan W(θ) is calculated for each ω_B (or ν_{Larmor}). In case of a frequency scan W(θ) is calculated for each ω_{RF} (or ν_{RF}). Using formula 4.14 the NMR curve can be simulated.

Resonance condition: $\omega_{RF} = \omega_B$

To get more insight in these formulae, we look first at the differential equations in case $\omega_{RF}(t) = \omega_B$, that means at resonance:

$$\begin{aligned} -\dot{b}_{+1/2} &= Aa_{-1/2} \\ \dot{a}_{+1/2} &= Ab_{-1/2} \\ -\dot{b}_{-1/2} &= Aa_{+1/2} \\ \dot{a}_{-1/2} &= Ab_{+1/2} \end{aligned} \tag{4.27}$$

which is analytically solvable:

$$\begin{aligned} a_{1/2}(t) &= a_{1/2}(t=0)cosAt + b_{-1/2}(t=0)sinAt \\ b_{1/2}(t) &= b_{1/2}(t=0)cosAt - a_{-1/2}(t=0)sinAt \\ a_{-1/2}(t) &= a_{-1/2}(t=0)cosAt + b_{1/2}(t=0)sinAt \\ b_{-1/2}(t) &= b_{-1/2}(t=0)cosAt - a_{1/2}(t=0)sinAt \end{aligned} \tag{4.28}$$

These coefficients show a sinusoidal behavior, with an angular velocity A. These oscillations are called Rabi-oscillations. Figure 4.7 shows

an example with $\mid c_{-1/2}(t=0) \mid^2 = 1$. The $c_i(t)$ coefficients are then time-integrated:

$$\mid c_x(averaged) \mid^2 = \frac{1}{\tau} \int e^{-t/\tau} \mid c_x(t) \mid^2 dt \approx \frac{1}{2} \tag{4.29}$$

with τ the lifetime of the nucleus. The approximation is only valid if the Rabi-oscillation is much faster than the exponential decay from the lifetime:

$$|\frac{g\mu_N B_{RF}}{2\hbar}| = \frac{\omega_1}{2} >> \frac{1}{\tau} \tag{4.30}$$

If this condition is not valid, $\mid c_x(averaged) \mid^2$ will not be equal to 1/2. Formula 4.9 shows that not all polarisation is destroyed in that case. Formula 4.30 gives the lower limit of the combination of lifetime, RF strength and g-factor to be able to perform a β-NMR measurement. Filling in the values of μ_N and $\hbar$ this formula gives $B_{RF}(gauss) >> \frac{1}{5g\tau(ms)}$, proving that NMR on nuclei with lifetimes much shorter than ms are impossible at reasonable RF power.

General case: $\omega_{RF} \neq \omega_B$

Using the Runge-Kutta method, the polarisation can be calculated for all ω_B and ω_{RF}. From the polarisation, the NMR curve is obtained with Formula 4.8 and 4.14.

When the applied RF frequency and the Larmor frequency are slightly different, the amplitude of the oscillations is not maximal (see Figure 4.8 middle). Making the time integral, one obtains a value for $\mid c_x(average) \mid^2$ different from 0.5, which means that not all polarisation is destroyed in this case.

Although no simple mathematical formula exists, notice that the frequency of the Rabi oscillations depends on the RF power and the difference between ν_{RF} and ν_{Larmor} (or ω_{RF} and ω_B).

Some simulated frequency scans are shown in Figure 4.9 top. Notice that the shape of the curve is Lorentz like and the width of the obtained resonance increases linearly with increasing RF power.

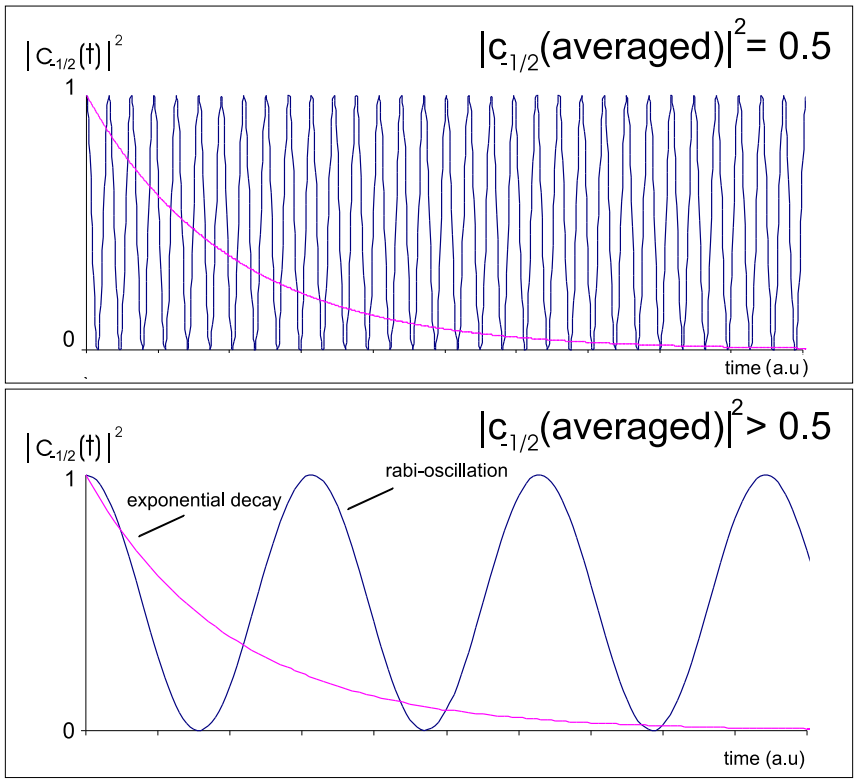

Figure 4.7: Time evolution of $\mid c_{-1/2} \mid^2$. (top) with large B_1, (bottom) with small B_1

Inhomogenous line-broadening

From Formula 4.30 one concludes that all polarisation is destroyed when $\nu_{RF} = \nu_{Larmor}$. This of course assumes that all nuclei interact with the same static field B_0, thus that the field is homogenous. Experimentally it is shown that to reach a maximum breakdown of asymmetry, the minimal RF-power should be higher than given in Formula 4.30.

Because the magnet that is used in the β-NMR experiments described in this thesis, is not homogenous over the full beam spot, the implanted nuclei feel a different B_0 depending on the implantation po-

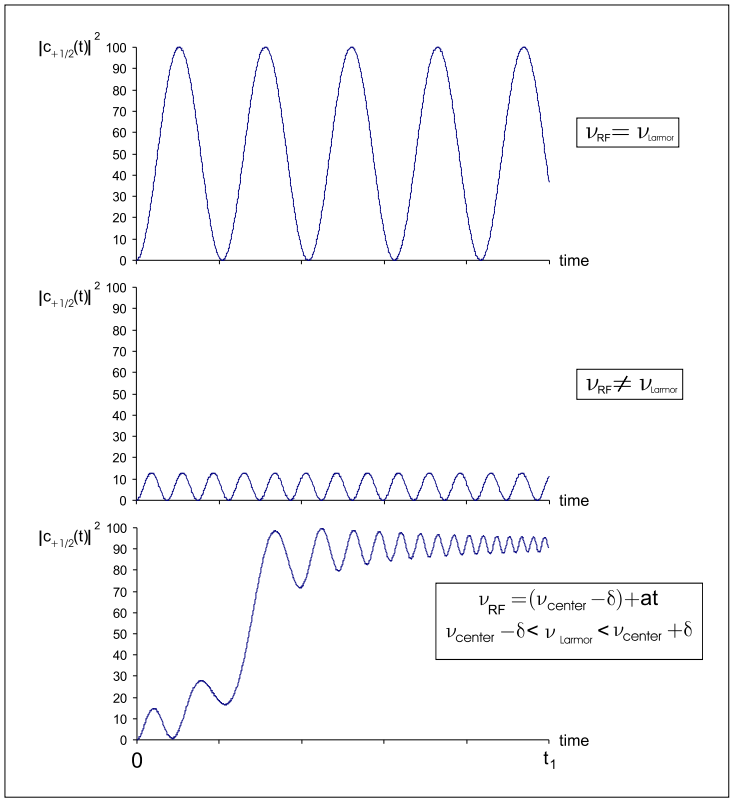

Figure 4.8: Behavior of $\mid c_{+1/2}(t) \mid^2$ for different NMR conditions.

sition.

In order to take the inhomogeneity of B_0 into account, we convolute the theoretically obtained NMR curve with a gaussian function, of which the width (ΔB) corresponds to the inhomogeneity.

As shown in the middle panel of Figure 4.9, the effect of such a convolution is a reduction of the amplitude of the NMR resonance, indicating that more RF strength is necessary to obtain the maximal effect in the NMR curve. If the NMR width due to the RF strength is larger than the

inhomogeneous line-broadening, the NMR amplitude is still maximal as shown in Figure 4.9 bottom. Once the inhomogeneous line-broadening is of the order or even larger than the RF strength width the amplitude decreases.

Frequency modulation (FM)

We will show now that next to increasing the RF power, applying a modulated RF-signal can give an increase of the amplitude in the NMR scan as well.

Notice that when taking into account the modulation, the Runge-Kutta method does not give extra complications in contrast to the analytic approach.

In the bottom panel of Figure 4.8, the behavior of $\mid c_{+1/2} \mid^2$ is shown for the first frequency sweep of ν_{RF} ($\nu_{RF} - \delta \rightarrow \nu_{RF} + \delta$), assuming maximal negative polarisation at $t = 0$. The RF frequency increases linearly with time from $\nu_{RF} - \delta$ to $\nu_{RF} + \delta$. If $\nu_{RF} - \delta$ is smaller than ν_{Larmor}, $\mid c_{+1/2} \mid^2$ gradually increases. When ν_{RF} has passed ν_{Larmor}, the population of the substates is inverted.

At this point one small problem occurs: a numerical method can only be used if at each moment the derivative of each parameter is continuous. Looking at Figure 4.6, this is not the case at t_{jump-1} for ν_{rf}. As an approximation, for the calculation of $c_i(t = t_{jump-x})$ it is assumed that

$$\begin{array}{l} \nu_{RF}(t_{jump-x} - \Delta t) = (\nu_{center} + \delta) - a\Delta t \\ \nu_{RF}(t_{jump-x} - \frac{\Delta t}{2}) = (\nu_{center} + \delta) - a\frac{\Delta t}{2} \\ \nu_{RF}(t_{jump-x}) = (\nu_{center} + \delta) \end{array} \tag{4.31}$$

and for $c_i(t = t_{jump-x} + \Delta t)$

$$\begin{array}{l} \nu_{RF}(t_{jump-x}) = (\nu_{center} - \delta) \\ \nu_{RF}(t_{jump-x} + \frac{\Delta t}{2}) = (\nu_{center} - \delta) + a\frac{\Delta t}{2} \\ \nu_{RF}(t_{jump-x} + \Delta t) = (\nu_{center} - \delta) + a\Delta t \end{array} \tag{4.32}$$

In the second sweep, $\mid c_{+1/2} \mid^2$ will decrease in the same manner as it increased in the first sweep. Calculating the time integration of sev-

eral sweeps results in $\mid c_{+1/2}(averaged) \mid^2 \approx 1/2$. For a frequency sweep $\nu_{RF} - \delta \rightarrow \nu_{RF} + \delta$, the polarisation will thus be destroyed completely, if $\nu_{Larmor} \epsilon [\nu_{RF} - \delta, \nu_{RF} + \delta]$.

If the duration of 1 sweep is of the same time order as the Rabi oscillation time of $\mid c_{+1/2} \mid^2$, the inversion of the levels is not completed when the next sweep starts. In that case the polarisation will not be destroyed completely. On the other hand, the lifetime of the nucleus should be longer than the duration of 1 sweep to obtain an average of 0.5.

In conclusion, the amplitude of the NMR resonance is mainly determined by five factors: lifetime of the observed nucleus, RF power, inhomogeneous line-broadening, modulation amplitude and modulation frequency. The most important conditions to perform efficient NMR experiments are:

$$\nu_{Rabi} > \nu_{mod} > 1/\tau \tag{4.33}$$

and the inhomogeneous line-broadening should be appreciably smaller than the NMR width due to the combination of the RF strength and frequency modulation amplitude.

4.4 NMR method: experimental procedure

Before starting a NMR measurement, a certain procedure is followed:

1. It is first checked if polarisation is present in the beam and which static magnetic field needs to be applied in order to keep the polarisation long enough.

2. Afterwards it can be checked for which experimental conditions this polarisation is maximal, e.g. by changing the selection in the longitudinal momentum of the fragments, by trying different crystals,...

The different steps of this procedure are explained in detail in the next chapter, solely devoted to polarisation. When all these parameters are optimised a NMR measurement is started.

Since a series LRC circuit with a narrow resonance peak ($\nu_{FWHM} \sim 100kHz$) is used to generate a high power radiofrequent signal, only a small g-factor region ($\Delta g = \frac{h\nu_{FWHM}}{B_0\mu_N}$) can be scanned at one time with a NMR scan as function of frequency (typically $\Delta g \approx 0.1g$). Therefore, in case the g-factor of the nucleus of interest is not known, we first scan a broad g-factor range by varying the static magnetic field B_0 while the frequency of the radiofrequent signal is kept constant. In a second step, the g-factor range is reduced enough to be able to measure as function of frequency, a measurement that is much faster as changing frequency is faster than changing field.

The data are taken in a sweep mode in order to avoid the influence of experimental asymmetry fluctuations during the scan. In case of a field scan, the field is changed every 2 minutes. Performing a frequency scan, the frequency is changed every 10 seconds. Data are taken between 1 hour and 8 hours typically, depending on the isotope production rate.

In both NMR methods, some beam time is used for normalizing the data, by turning off the RF signal. The measuring procedures are visualised in Figure 4.10. Notice that 50% of the beam time is used to normalize in the case of field scans, while this is less than 10% in a frequency scan, depending on the number of frequencies scanned.

In case of a field scan, the asymmetry A ($=N_{UP}/N_{DOWN}$) as a function of the field for the RF off data gives a 'decoupling curve' (see further) without any resonance. A fitted trendline through these data is used to determine the asymmetry of the baseline (A_{base}). In case of a frequency scan, the RF off point is pictured on the outer right of the NMR figure and the average of all data in the base-line as well as the RF-off point is used to determine A_{base}.

In case of a field scan (frequency scan), from the plot of the field (frequency) versus 'A_{NMR}', the g-factor is deduced, using the fit program explained before. A_{NMR} and ΔA_{NMR} are defined as

$$A_{NMR}(x) = \frac{A(x) - A_{base}}{A(x)} \tag{4.34}$$

$$\Delta A_{NMR} = \frac{(A_{NMR})_{in-resonance} - (A_{NMR})_{out-resonance}}{(A_{NMR})_{in-resonance}} \tag{4.35}$$

with $A(x)$ the asymmetry N_{up}/N_{down} for the applied static magnetic field (frequency) x.

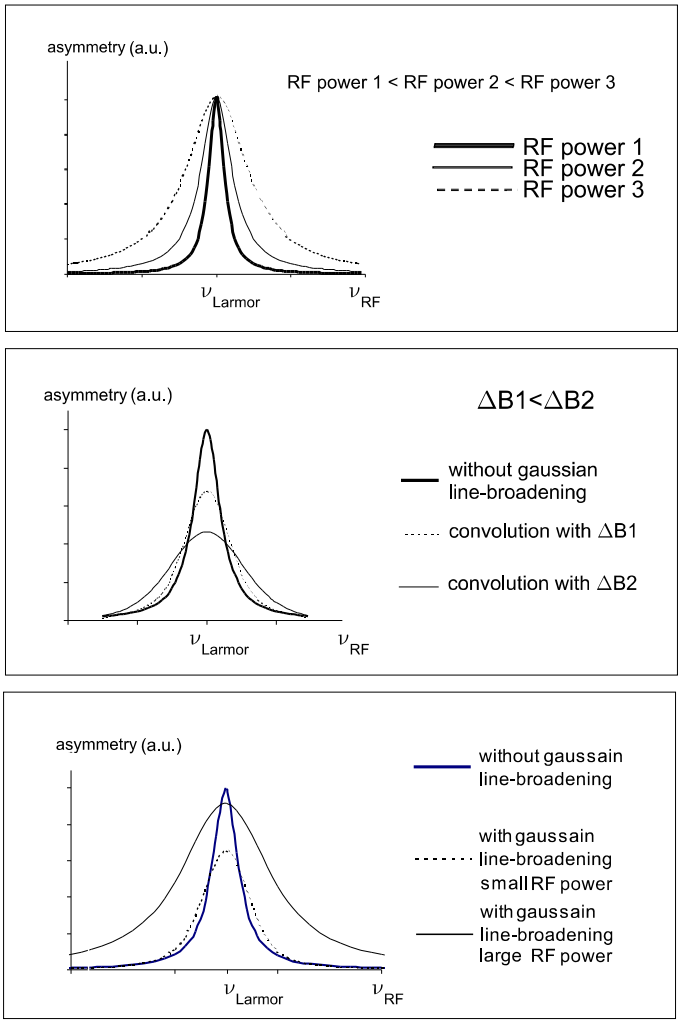

Figure 4.9: (top)Simulated NMR curves showing the dependency of the NMR width on RF strength. (middle) Simulated NMR curves showing the dependency of amplitude and shape of the NMR curve on gaussian line-broadening. (bottom) Simulated NMR curves showing the dependence of the asymmetry on RF strength and gaussian line-broadening.

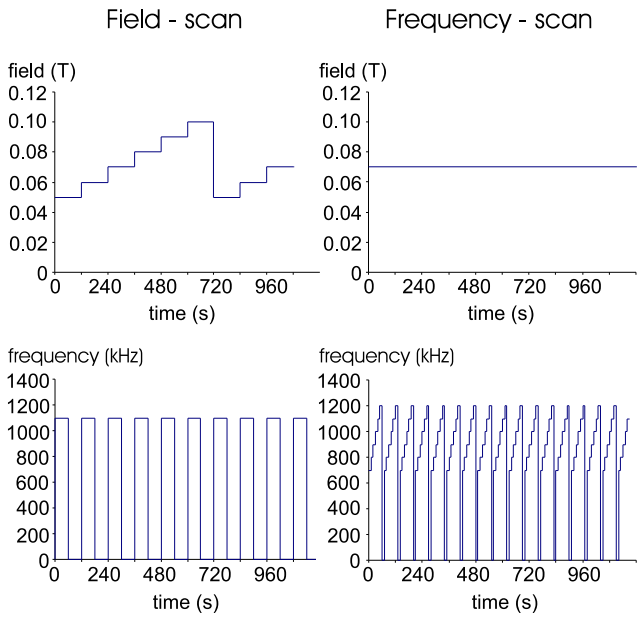

Figure 4.10: Visualisation of static magnetic field and radio-frequent field as function of time.

Chapter 5

Polarisation

In the previous chapter some conditions on the NMR parameters (such as RF power, lifetime of the nucleus,...) were given to destroy as much polarisation as possible at the resonance condition, in order to obtain the largest effect in the NMR resonance.

In this chapter, first it will be explained how this polarisation is obtained and second, what are the optimal conditions to preserve it.

It is known that the reaction products of some reaction mechanisms such as fusion evaporation, projectile-fragmentation and pick-up, are polarised under certain conditions. Only the latter two reaction types were used to produce the nuclei studied in this thesis work. A simple kinematical model developed by Asahi et al. [91] and Okuno et al. [92] describes the spin-orientation created in a projectile fragmentation reaction. Turzo et al. [93] extended this model to describe the production of polarisation with a pick-up reaction. Both models will be introduced and some obtained experimental results will be discussed in the beginning of this chapter.

To determine the lowest magnetic field necessary to preserve the polarisation, a decoupling curve is measured. Also different crystals are used as a stopper crystal in order to deduce the crystal with the best implantation properties: the Al and Si isotopes should be implanted at substitutional lattice sites with cubic symmetry and the relaxation times

of the implanted nuclei have to be longer than the life-time, in order to be able to obtain the maximal effect in the NMR scan. These tests are discussed in the second part of this chapter.

5.1 Production of polarisation: theory

5.1.1 Projectile fragmentation reaction

All investigated nuclei were produced at GANIL with a ^{36}S beam of around 77.5MeV/u impinging on a ^{9}Be or a ^{184}W target. At relativistic energies, the fragmentation occurs for peripheral collisions. One can assume for a projectile fragmentation reaction that the nucleons from the projectile which belong to the geometrical overlapping volume with the target nuclei, are removed.

The rest of the projectile (the pre-fragment) undergoes the evaporation of a few nucleons after which the final fragment is formed. This simple picture, known as 'the participant-spectator model', results in a gaussian like shape for the longitudinal and transversal momentum distribution of the outgoing fragments, if we assume that the removal happens randomly.

Although the energies in this work are considered as intermediate, we choose 'the participant-spectator model' as a good approach to describe our results.

The width of the longitudinal momentum distribution is known as the Goldhaber width $\sigma_{//}$ [94], which is a function of the reduced width σ_0:

$$\sigma_{//} = \sigma_o \sqrt{\frac{A_f(A_p - A_f)}{A_p - 1}} \tag{5.1}$$

with A_p and A_f the masses of the projectile and the outgoing fragment respectively.

The width of the transversal momentum distribution is called the 'perpendicular width' $\sigma_\perp$ which is a function of the Goldhaber width, with σ_d the orbital dispersion.

$$\sigma_\perp^2 = \sigma_{//}^2 + \sigma_d^2 \frac{A_f(A_f-1)}{A_p(A_p-1)} \tag{5.2}$$

The fragments produced at the target are collected at a small finite angle θ_L (with $\theta_L \epsilon [(\theta_L)_{min}, (\theta_L)_{max}]$, which are the experimental selection angles, depending on the angular acceptance of the fragment separator) in order to break the symmetry of the reaction and to be able to select a polarised ensemble, as explained further. The spin-orientation is created in these reactions via the transfer of momentum during the reaction process. The angular momentum of the formed fragments allows to deduce the fragment spin-orientation. The linear and angular momentum of the pre-fragment ($\bar{p}_f^*$ and $\bar{J}_f^*$) can be calculated as a function of the projectiles linear momentum $\bar{p}_p$ and the relative position and momentum of the abraded part of the projectile using linear and angular momentum conservation laws.

It is assumed that in the subsequent evaporation stage, the angular momentum of the fragment does not change its orientation. This means that the evaporation of the nucleons from the pre-fragment to become the fragment occurs in random direction. We assume as well that the projectile spin is zero and the abraded nucleons have negligible intrinsic spin. The energy of the projectile before the target is taken as the energy the projectile would have after the target, according to LISE simulations, in order to take into account for the small amount of energy loss in the thin target.

$\bar{K}$ is defined as the momentum of the abraded part in the target rest frame (=laboratory frame), while $\bar{k}$ is the momentum of the abraded part in the projectile rest frame. In case of projectile fragmentation the average momentum vector of the nucleons that are abraded from the projectile ($< \bar{k} >$), is found to be zero.

Using basic mechanics, the relation between $\bar{K}$ and $\bar{k}$ can be derived for projectile fragmentation reactions:

$$\bar{k} = \bar{K} - \frac{m_p - m_f^*}{m_p}\bar{p}_p \tag{5.3}$$

In the laboratory frame the following relations hold (see Figure 5.1):

$\bar{p}_p = \bar{p}_f^* + \bar{K}$	the linear momentum vector of the projectile is equal to the sum of the linear momentum vector of the pre-fragment and the linear
$\Rightarrow \bar{p}_f^* = \frac{m_f^*}{m_p}\bar{p}_p - \bar{k}$	momentum vector of the abraded nucleons
$< \bar{p}_p >= \frac{m_p}{m_f^*} < \bar{p}_f^* >$	the average linear momentum of the projectiles is directly related to the average linear momentum of the pre-fragments through $\frac{m_p}{m_f^*}$ since $< (\bar{k})_{x,y,z} >= 0$ in a fragmentation reaction
$< \bar{p}_f >= \frac{m_f}{m_f^*} < \bar{p}_f^* >$	the average linear momentum of the fragments is directly related to the average linear momentum of the pre-fragments
$\bar{J}_f^* = -\bar{R} \times \bar{k}$	since nucleons of the projectile are abraded, the angular momentum of the pre-fragment opposites the angular momentum of the abraded nucleons (assuming the spin of the projectile to be 0)
$< \bar{J}_f^* >=< \bar{J}_f >$	the average angular momentum of the pre-fragments is equal to the average angular momentum of the fragments(we assume that evaporation occurs isotropically and does not affect therefore the spin-orientation)

The polarisation is defined as

$$P = \frac{< (J_f)_z >}{\mid \bar{J}_f \mid} \text{ with } (J_f)_z = -(R)_x(k)_y + (k)_x(R)_y \qquad (5.4)$$

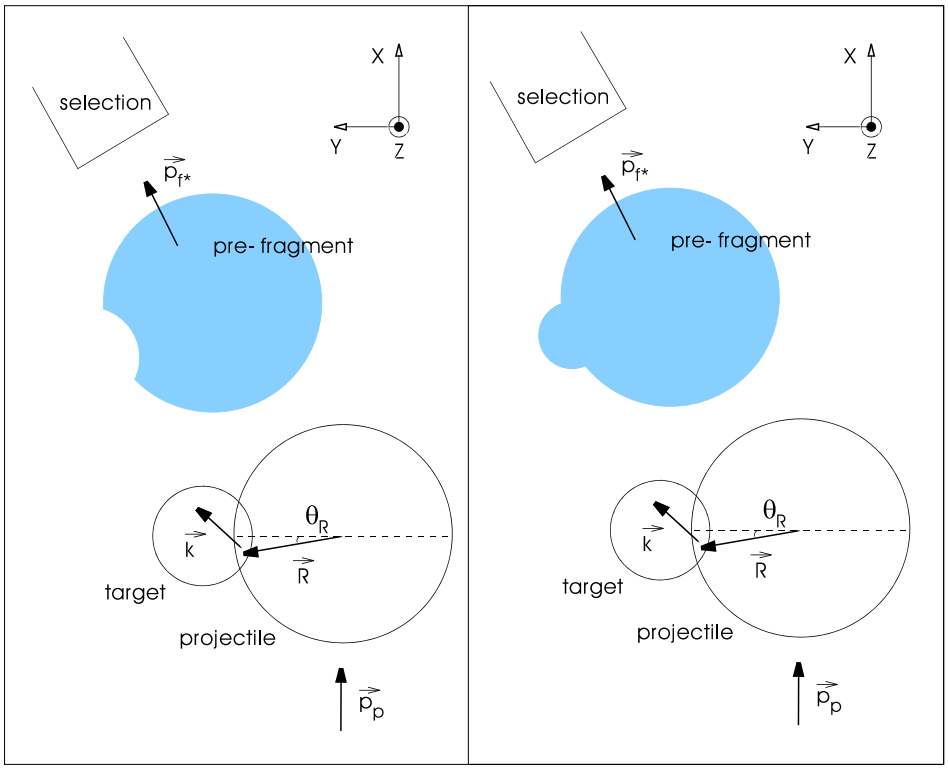

Figure 5.1: Schematic design of fragmentation (left) and pick-up (right) reaction.

A schematic design of the reaction is presented in the projectile rest frame in Figure 5.1. The X-axis is chosen as the beam direction, the Z-axis perpendicular to the reaction plane and in such a way that the cross product $\bar{p}_p \times \bar{p}_f^*$ has the same sense as the Z-axis. The angle θ_R is defined as the angle from the positive Y-axis to the negative X-axis. In

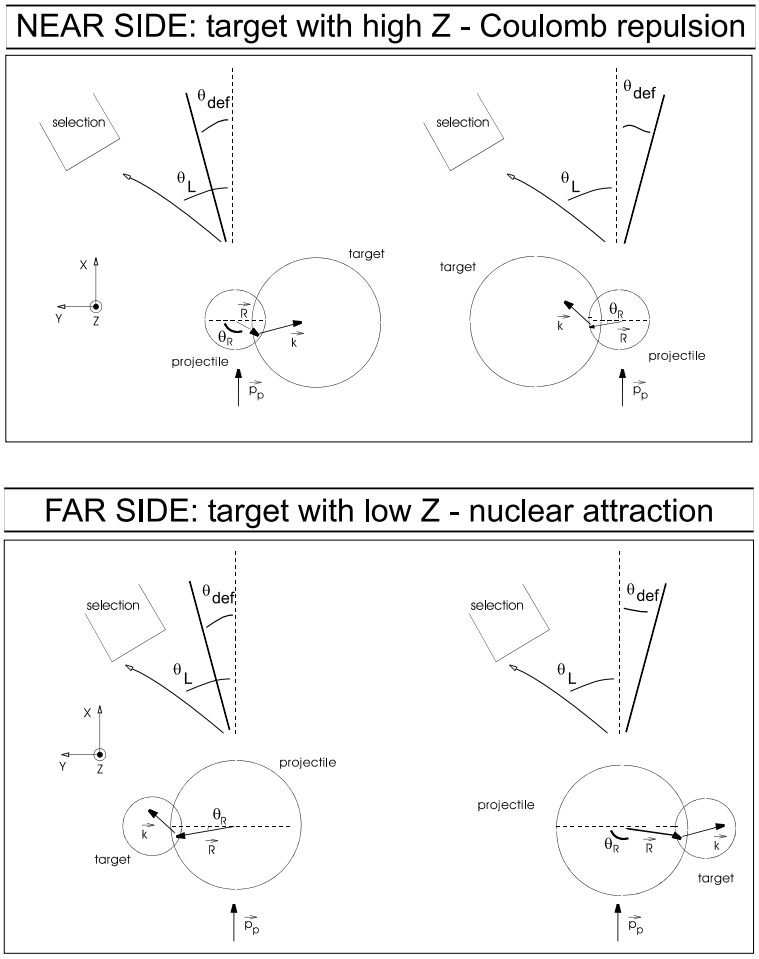

Figure 5.2: (top) Near side reaction. (bottom) Far side reaction.

Figure 5.1 this angle is positive.

At this point a distinction between two types of projectile fragmentation reactions is made: 'near side' and 'far side' reactions. In 'near side' reactions the target is substantially larger than the projectile and the Coulomb repulsion dominates over the nuclear attraction. In 'far side' reactions, with light targets, the reaction is dominated by the nuclear attraction. The difference between the two reaction types is shown in Figure 5.2. Notice that in both reaction types the projectile can hit the target at either side.

The angle the fragment makes with the projectile is the sum of two components:

- the deflection angle: This angle is calculated classically with the Coulomb and nucleus-nucleus potentials [95]. In this calculation, the impact parameter is chosen so that the geometrical overlapping volume corresponds to the number of abraded nucleons from the projectile to form the pre-fragment. It is assumed that 1/3 of $|A_p - A_f|$ is evaporated after the pre-fragment is made [96]. For the reactions studied in this thesis work, this angle is $\sim 0.9^o$. The deflection angle depends primarily on the beam energy and the number of nucleons abraded from the target:

$$E_{beam} \nearrow \Longrightarrow \theta_{def} \searrow \tag{5.5}$$

$$\mid A_p - A_f \mid \nearrow \Longrightarrow \theta_{def} \nearrow \tag{5.6}$$

- the angle due to k_y: Simple geometry on the left part of Figure 5.3a shows that the absolute value of this angle is equal to

$$|arctan(\frac{k_y}{\frac{m_f^*}{m_p}|p_p|})| \tag{5.7}$$

It is assumed that if the sum of these angles is a value between θ_{Lmin} and θ_{Lmax}, the nucleus is detected, see Figure 5.3b.

In order to understand the influence of some parameters on the polarisation, we omit at the moment the reaction products on the right part of Figure 5.2. This restriction is allowed only if the width of the

longitudinal distribution is small (and thus k_y small) and θ_L large.

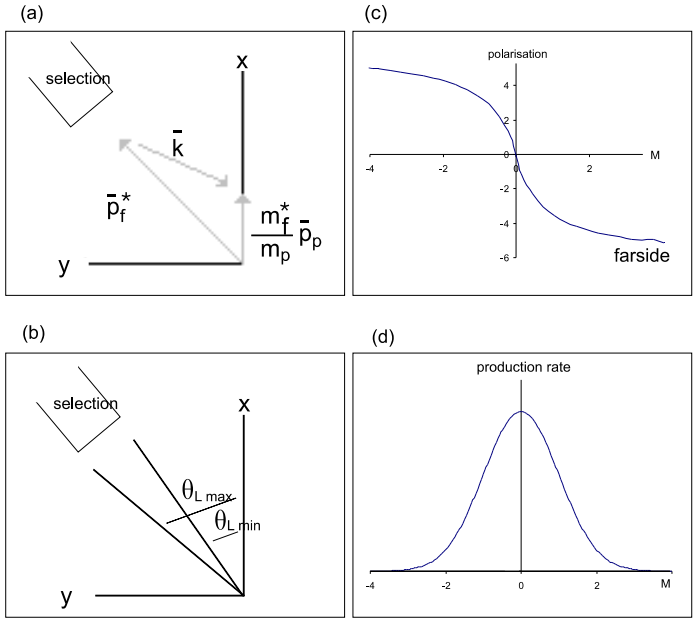

Figure 5.3: (a) Determination of the sign of k_x (b) definition of θ_{Lmin} and θ_{Lmax} (c-d) Polarisation and production rate as function of $M = \frac{(\bar{p}_f)_x - \frac{m_f}{m_p}(\bar{p}_p)_x}{\frac{m_f}{m_p}(\bar{p}_p)_x}$ for near and far side reactions.

It is clear from Figure 5.2 that $(\bar{R}_y) > 0$ ($(\bar{R}_y) < 0$) in pure far side (near side) reactions. On the other hand, from the left part of Figure 5.3 one concludes that

$$|(\bar{p}_f)_x| > \frac{m_f}{m_p}|(\bar{p}_p)_x| \Rightarrow k_x < 0 \tag{5.8}$$

$$|(\bar{p}_f)_x| < \frac{m_f}{m_p}|(\bar{p}_p)_x| \Rightarrow k_x > 0 \tag{5.9}$$

Since $P \sim < (\bar{J}_f)_z > = < (\bar{k})_x (\bar{R})_y >$, the polarisation for both reaction types is different and changes sign when going from $(\bar{p}_f)_x$ smaller

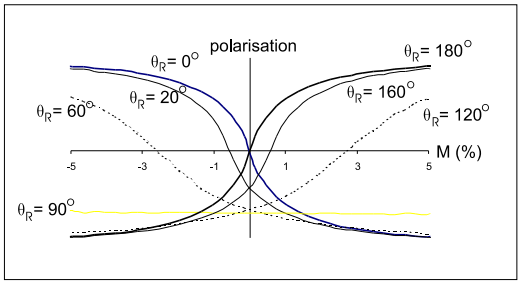

Figure 5.4: Dependence of polarisation on θ_R for $\theta_L = 2^o$, without taking into account the reaction products of Figure 5.2 right.

than $\frac{m_f}{m_p}(\bar{p}_p)_x$ to $(\bar{p}_f)_x$ larger than $\frac{m_f}{m_p}(\bar{p}_p)_x$. A simulation of this behavior of the polarisation, with $\theta_R = 0^o$ (farside) or $\theta_R = 180^o$ (nearside) is shown on Figure 5.3c.

The relative momentum

$$M = \frac{(\bar{p}_f)_x - \frac{m_f}{m_p}(\bar{p}_p)_x}{\frac{m_f}{m_p}(\bar{p}_p)_x} \tag{5.10}$$

is presented on the x-axis. The 0-point of this axis is defined as the momentum at which the production rate is maximal. In case of fragmentation, this is when $(\bar{p}_f)_x = \frac{m_f}{m_p}(\bar{p}_p)_x$.

In general both the Coulomb repulsion and the nuclear attraction processes can contribute to the fragmentation reaction. That means that R_x is not zero since θ_R is no longer equal to 0^o or 180^o, but equals an intermediate value. As a consequence, $- < R_x k_y >$ is different from zero which leads to the fact that the polarisation is no longer vanishing at the center of the yield distribution. For all projectile fragmentation reactions in between the pure near and far side cases, at the center of the momentum distribution the polarisation is negative (see Figure 5.4) since $R_x < 0$ and $k_y < 0$ for all fragments detected at $\theta_L \epsilon [\theta_{Lmin}, \theta_{Lmax}]$ and θ_R between 0^o and 180^o (see Figure 5.2 and 5.3). Since $|k_y| \sim \theta_L$, the polarisation at the center of the yield distribution for a reaction in between near and far side increases with increasing θ_L at the center of the momentum distribution.

As mentioned before, in reality the assumption of omitting reaction products from the right side of Figure 5.2 is incorrect. If k_y is not very small and θ_L small, reaction products from the right side of Figure 5.2 can be detected as well. Notice that R_y has the opposite sign for these reactions. This causes the sign of the polarisation for the latter reactions to be opposite to the reaction from Figure 5.2 left. The more fragments from Figure 5.2 right are selected the smaller the absolute polarisation will be.

Bearing in mind this last comment, the maximum amount of polarisation created depends crucially on the beam energy, projectile, θ_L, the deflection angle and the number of nucleons abraded. Some of these dependencies are shown in Figure 5.5, but it is not possible to draw general conclusions from this. Each reaction needs to be simulated, in order to define the optimal conditions for producing a polarised beam.

In case a selection is made symmetrically around 0^o, as much fragments produced from the left as the right part of Figure 5.2 are detected. In this case, the polarisation will be 0, showing that a non symmetrical selection needs to be made in order to detect polarisation in fragmentation reactions.

5.1.2 Pick-up reaction

In a pick-up reaction, also the participant-spectator model is assumed, stating now that the nucleons from the target, which belong to the geometrical overlapping volume with the projectile nuclei, are picked up by the projectile. A schematic picture of a pick-up reaction is shown in Figure 5.2b.

The polarisation trend as a function of the linear momentum can be derived in an analog way as for the projectile fragmentation case. The main difference is the fact that in a pick-up reaction first 1 or several extra nucleons are picked up from the target by the projectile, while 1 or several nuclei are abraded from the projectile in the case of projectile fragmentation. In both reaction types, this process is followed by the evaporation of some nuclei. For instance, in the ^{36}S+^{9}Be$\rightarrow^{34}Al$ reaction, it is assumed that 1 neutron is picked up in a first step (leading to polarisation), followed by the isotropic evaporation of 3 protons. We have demonstrated that this simple model indeed gives a very good description of the qualitative behavior of spin-polarisation in a pick-up reaction [93].

In the case of a pick-up reaction at intermediate energies Souliotis et al. [97] and Pfaff et al. [98] have shown that the average momentum of the nucleon that is picked-up from the target, has a momentum equal

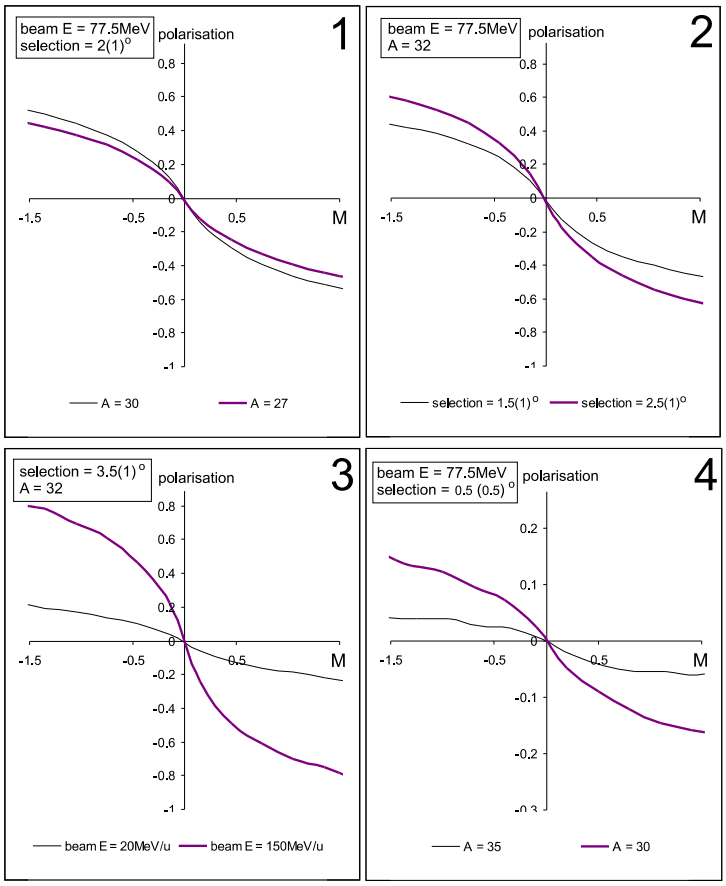

Figure 5.5: Dependence of polarisation on fragment mass, selection angle (θ_L) and beam energy for a fragmentation reaction of a ^{36}S beam on a ^{9}Be target. Comparing simulation 1 and 4 clearly shows the need to simulate each reaction in order not to make wrong generalizations.

to the Fermi momentum and is oriented preferentially parallel to the incident projectile direction in the target rest frame. In our experiments, the Fermi momentum is about 212 MeV/c [99], as compared to the projectile momentum of about 13 GeV/c.

Using basic mechanics, the relation between $\bar{K}$ and $\bar{k}$ can be derived for pick-up reactions:

$$\bar{k} = \bar{K} - \frac{m_f^* - m_p}{m_p}\bar{p}_p \tag{5.11}$$

Assuming $< K_x >= 212 MeV/c$ and $(p_p)_x = 13 GeV/c$, we find that $< k_x >= -152 MeV/c$.

The formulas used in the projectile fragmentation case have to be altered slightly, considering that now a nucleon with momentum $\bar{K}$ is picked up from the target:

$\bar{p}_p = \bar{p}_f^* - \bar{K}$ $\Rightarrow \bar{p}_f^* = \frac{m_f^*}{m_p}\bar{p}_p + \bar{k}$	the linear momentum of the pre-fragment is equal to the sum of the linear momentum of the projectile and the linear momentum of the picked-up nucleon
$\bar{p}_p = \frac{m_p}{m_f^*}\bar{p}_f^* - \frac{m_p}{m_f^*}\bar{k}$	the linear momentum of the projectile is directly related to the linear momentum of the pre-fragment and the momentum of the picked-up nucleon
$< \bar{p}_f >= \frac{m_f}{m_f^*} < \bar{p}_f^* >$	the average linear momentum of the fragment is directly related to the average linear momentum of the pre-fragment through $\frac{m_f}{m_f^*}$
$\bar{J}_f^* = \bar{R} \times \bar{k}$	the angular momentum of the pre-fragment is equal to the angular momentum of the picked-up nucleon

$< \bar{J}_f^* >=< \bar{J}_f >$	the average angular momentum of the pre-fragment is equal to the average angular momentum of the fragment
$< (K)_x >= p_{Fermi}$	the x-component of the average linear momentum of the picked-up nucleon is equal to the Fermi energy of the nucleon in the target rest frame

Assuming a pure 'far side' trajectory and a selection as in Figure 5.2, $(J)_z = -(k)_x(R)_y$, with $(k)_x$ negative and $(R)_y$ positive, the polarisation is positive at the maximum of the production rate p_{center} and becomes zero if $(\bar{p}_f)_x = p_{center} + 152MeV/c$.

Assuming a pure 'near side' trajectory and a selection as in Figure 5.2, $(J)_z = -(k)_x(R)_y$,with $(k)_x$ negative and $(R)_y$ negative, the polarisation is negative at the maximum of the production rate p_{center} and becomes zero if $(\bar{p}_f)_x = p_{center} + 152MeV/c$.

The polarisation as function of momentum for a pure 'far side' 1 nucleon pick-up reaction ($^{36}S +^{9} Be \rightarrow^{34} Al$) is shown in Figure 5.6. The relative momentum

$$M = \frac{(\bar{p}_f)_x - \frac{m_f}{m_p}(\bar{p}_p)_x - \frac{m_f}{m_f^*} < (k)_x >}{\frac{m_f}{m_p}(\bar{p}_p)_x + \frac{m_f}{m_f^*} < (k)_x >} \tag{5.12}$$

is presented on the x-axis.

The 0-point of this axis is defined as the momentum at which the production rate is maximal. In case of pick-up, this is when $(\bar{p}_f)_x = \frac{m_f}{m_p}(\bar{p}_p)_x + \frac{m_f}{m_f^*} < (\bar{k})_x >$.

Notice that in the case two nucleons are picked up $< (\bar{K})_x >= 2p_{Fermi}$ and the polarisation will be zero at $(\bar{p}_f)_x = p_{center} + 304 MeV/c$.

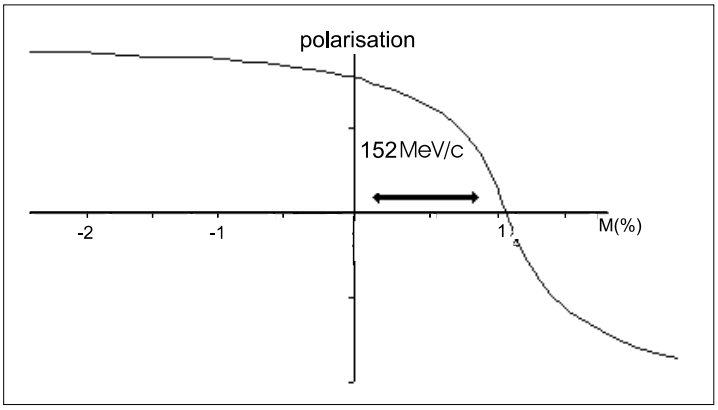

Figure 5.6: Polarisation as function of momentum for a pure far side pick-up reaction, in which one particle is picked up from the target. $M = \frac{(\bar{p}_f)_x - \frac{m_f}{m_p}(\bar{p}_p)_x - \frac{m_f}{m_f^*}<(k)_x>}{\frac{m_f}{m_p}(\bar{p}_p)_x + \frac{m_f}{m_f^*}<(k)_x>}$

Notice that at the center of the momentum distribution, where the production rate is maximal, the polarisation is large, in contrast to the projectile-fragmentation reaction, that has zero polarisation at the center. This is a big advantage of pick-up reactions.

For a pick-up reaction in between near and far side, the first term of $< (J)_z >$ is different from zero. Since it has the opposite sign as in the fragmentation case, the polarisation curve will be shifted to the right.

5.2 Methods to measure polarisation

In the description of the kinematical model, it was explained that the secondary beam needs to be selected under a certain angle different from zero in order to obtain a polarised ensemble. In practice, this condition is obtained, not by selecting the secondary beam under an angle θ_L, but by deviating the primary beam over a deflection angle θ_L. This is done via a movable dipole magnet just before the target. The reaction products are then selected in a forward direction, as shown in Figure 5.7.

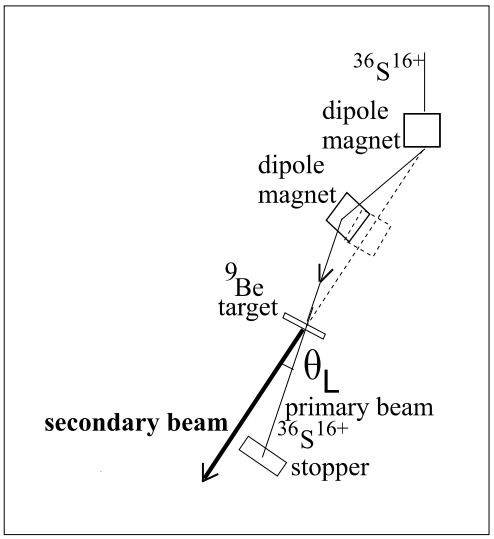

Figure 5.7: Schematic view of part of the LISE beamline

In case of a projectile fragmentation reaction, the maximum yield of a certain fragment is obtained when $(\bar{v}_f)_x = (\bar{v}_p)_x$ (or $(\bar{p}_f)_x = \frac{m_f}{m_p}(\bar{p}_p)_x$). This condition can be fulfilled by changing the magnetic rigidity of the dipole since $(\bar{p}_f)_x \sim B\rho 1$.

A first method to select different parts of the longitudinal momentum distribution of the fragments, is by altering the target thickness by tilting the target over an angle θ_t, while the same magnetic rigidity is being kept for the dipoles of the spectrometer. If the target is tilted more

with respect to the vertical position, the momentum of the fragment will be smaller (due to higher effective target thickness). In order to determine the exact dependence of the momentum on the target thickness, LISE calculations are made. The opening of the slits at the intermediate focal plane of the spectrometer (called F31) determines the width of the momentum acceptance.

Instead of altering the angle on the target, the momentum distribution can be scanned by changing the position of the momentum slits at LISE (F31) and keeping the target angle fixed. Because the path of the nuclei influenced by a dipole magnet depends crucially on their velocity, changing the slit position will select another part in the longitudinal momentum distribution. In order to determine the dependence of the momentum on the slits position, again LISE calculations are made. Both selection methods are schematically visualised in Figure 5.8.

Once the preferred momentum selection is made, the polarisation in the selected nuclear ensemble is determined. In order to get a rough idea of the amount of polarisation produced, so called 'polarisation tests' are performed:

The β-decaying nuclei are implanted in a crystal with cubic lattice symmetry, placed at the center of the static magnetic field. This field is changing from a high value ($B_0 \approx 0.1T$) to a very low value ($B_0 \approx 0T$) every 60 seconds. If $B_0 \approx 0$ T, it is assumed that the nuclear polarisation is immediately destroyed after implantation in the crystal due to interactions with small defect associated electric field gradients or small random fields. At high static magnetic fields the Zeeman interaction is stronger than these interactions. The nuclear ensemble is said to be decoupled from the perturbing interaction and coupled to the Zeeman interaction. Because the magnetic field is chosen along the symmetry axis of polarisation, the polarisation of the implanted ensemble is maintained in this case. If then the spin-lattice relaxation time of the implanted isotope in the crystal is longer than a few nuclear lifetimes, the observed β-asymmetry reflects the amount of produced polarisation. The behavior of the β-asymmetry as function of the applied static magnetic field is called the decoupling curve.

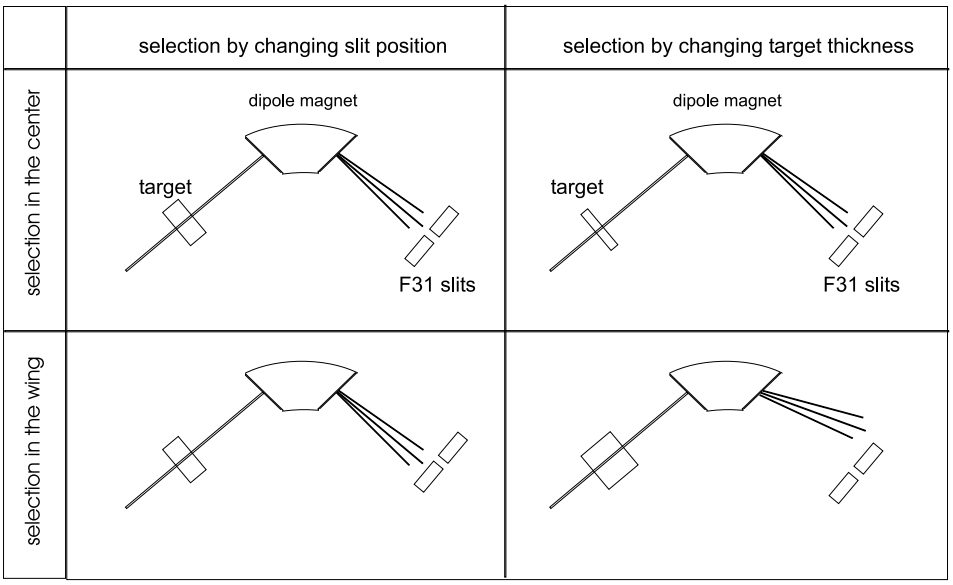

Figure 5.8: Schematic view of 2 methods to select the desired part of the longitudinal momentum distribution. (top) Since the path of the fragments after the dipole magnet depends on the fragment velocity, by changing the slit position another part of the distribution can be selected. (bottom) Making the target thicker (by tilting), decreases the velocity of the fragments and consequently changes the path of the fragments after the dipole magnet.

According to Formula 4.7, the amount of polarisation can be obtained from the difference in experimental β-asymmetry $A = N_{UP}/N_{DOWN}$ in the two cases:

$$\Delta A_N = \frac{(\frac{N_{up}}{N_{down}})_{B_0=0} - (\frac{N_{up}}{N_{down}})_{B_0=high}}{(\frac{N_{up}}{N_{down}})_{B_0=0}} = \frac{A_{B_0=0} - A_{B_0=high}}{A_{B_0=0}} \tag{5.13}$$

$$\approx \frac{(\frac{N_{up}}{N_{down}})_{B_0=0} - (\frac{N_{up}}{N_{down}})_{B_0=0}(\frac{1+A_1P_I\sqrt{\frac{3I}{I+1}}Q_1^{exp}}{1-A_1P_I\sqrt{\frac{3I}{I+1}}Q_1^{exp}})}{(\frac{N_{up}}{N_{down}})_{B_0=0}} \tag{5.14}$$

$$= 1 - \frac{1 + A_1P_I\sqrt{\frac{3I}{I+1}}Q_1^{exp}}{1 - A_1P_I\sqrt{\frac{3I}{I+1}}Q_1^{exp}} \approx -2A_1P_I\sqrt{\frac{3I}{I+1}}Q_1^{exp} \tag{5.15}$$

ΔA_N is referred to as the normalised asymmetry difference. In the following, the experimental asymmetry is deduced from the whole coincident β-spectrum, unless otherwise mentioned.

In trying to derive the amount of created polarisation with this method, three problems arise:

1. It is possible that the polarisation is lost before the nucleus decays due to relaxation effects. Relaxation times (T_1) mainly depend on the crystal properties and in case of a metallic host the Korringa relaxation is dominant. This depends on the g factor of the implanted nucleus, the Knight shift (K) and the temperature (T) [100]:

$$T_1 = \frac{1}{274900K^2g^2T} \tag{5.16}$$

The Knight shift in Si is small because of the low free-electron density in semiconducting Si crystal at room temperature. The relaxation time of ^{25}Al in Si was measured to be 4(1)s [101]. Since the lifetime of all measured nuclei is shorter than 1 second, the relaxation time is sufficiently longer than the lifetime of every examined nucleus.

2. In a first approximation the decoupling curve can be described as the interaction between the nucleus in the static magnetic field and a randomly oriented electric field gradient. The interaction between an ensemble of nuclei and the combination of a static field and a field gradient which makes an angle β with the static magnetic field is extensively studied before. Such a system is used in the Level Mixing Resonance technique and the expected asymmetry curve as function of the magnetic field can be calculated exactly. By integrating over all angles $0 < \beta < 90^0$, the decoupling curve is obtained. In Figure 5.9 some simulated decoupling curves are shown for different field gradients, spins, alignment and polarisation. In order to perform a correct polarisation test, the measurements of the asymmetry have to be done at 0T and at fields so high that the decoupling curve becomes constant. Depending on the electric field gradient of the crystal and the quadrupole moment of the implanted nucleus, this can occur at very high fields. Since the magnet used in these experiments can only generate a maximal B_0 of 0.16 T, in some cases the decoupling curve is not saturated at these field values and consequently a wrong amount of polarisation is deduced from a polarisation test.

3. Since alignment can be transferred to polarisation due to the interaction with an electric field gradient in the crystal and it is the change in polarisation that determines the amplitude of the decoupling curve, the decoupling curve is determined not only by the amount of polarisation, but also partly by the alignment in the beam. Figure 5.9 shows two extreme cases: a pure aligned versus a pure polarised beam. A mixture of both figures will be the real result. Notice that the polarisation curves are not sensitive to the sign of the quadrupole frequency. The alignment curves are mirrored around the baseline if the sign of the quadrupole frequency is changed. In a first approach we can say, for instance for I = 1, that an asymmetry difference of 8% between B = 0.005T and B = 0.15T can be due to 5% polarisation and 5% alignment (with QF = -0.1 MHz), or 9% polarisation and 5% alignment (with QF = +0.1 MHz).

It was shown experimentally that the alignment component indeed influences A_N drastically. A measurement of the polarisation via the amplitude of an NMR scan resulted in $\Delta A_{NMR} = 0.6(7)\%$, while a po-

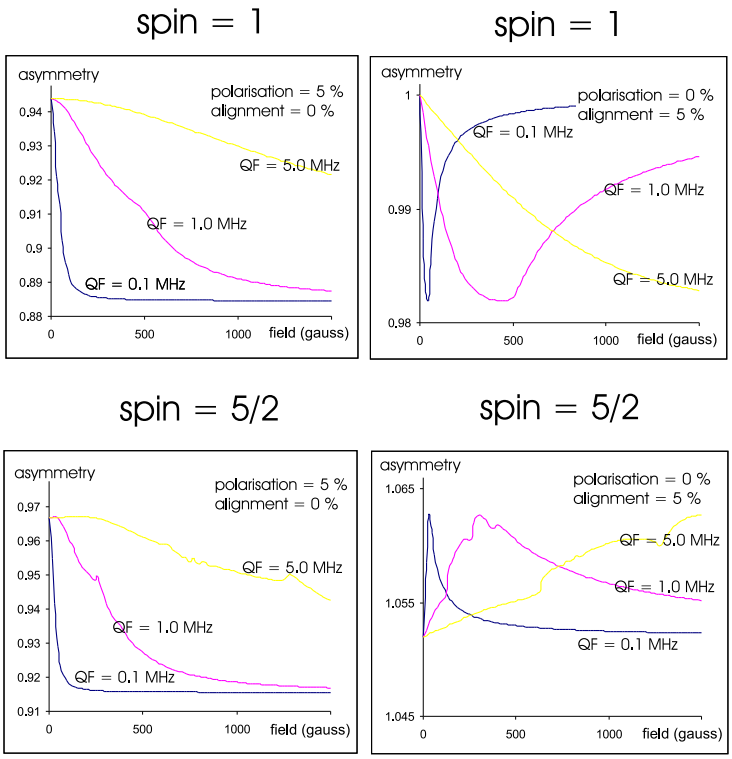

Figure 5.9: Asymmetry as function of field for several quadrupole frequencies (QF), spins, alignment and polarisation.

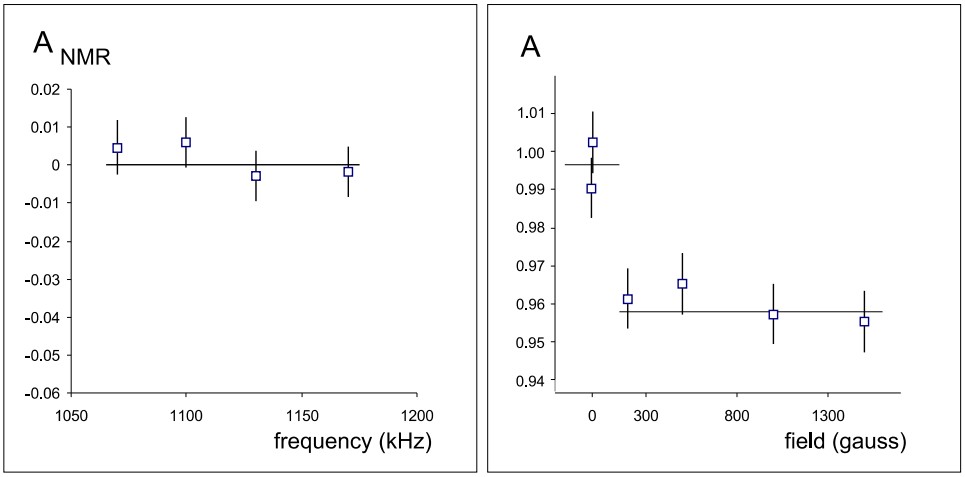

Figure 5.10: (left) β-NMR curve of ^{32}Al with the momentum selection at the center of the yield distribution. No effect is observed at the expected frequency ($\sim$ 1097kHz) . (right) Polarisation test of ^{32}Al with the momentum selection at the center of the yield distribution. An effect of 4.1(5)% is observed.

larisation test gave $\Delta(A)_N = -4.1(5)\%$ (see Figure 5.10). In both cases nuclei in the center of the momentum distribution are selected. The NMR result indicates that at the center of the distribution, as expected from the kinematical model, the polarisation is nearly zero. ΔA_N in the polarisation test is solely due to the alignment. Fitting the decoupling curve through the six measured fields suggests 10% alignment and a positive quadrupole frequency.

Since the sign of the field gradient responsible for the decoupling curve is not known, the sign of the quadrupole moment can not be deduced from this result. The sign of the quadrupole moment of another nucleus could be derived relative to ^{32}Al, performing the same experiment. Since the effect of alignment becomes smaller with increasing spin, this experiment was not performed on ^{31}Al (I = 5/2), ^{33}Al (I = 5/2), ^{34}Al (I = 4) or ^{35}Si (I = 7/2).

A more exact way to compare the polarisation for different isotopes, is to look at the amount of destroyed polarisation, deduced from the observed NMR resonances. Once the gaussian line-broadening and RF power are determined, the only unknown parameter to fit the height of the resonance is the amount of initial polarisation. This is done for some exotic Al-isotopes in the next sub-section.

5.3 Theory versus experiment

5.3.1 Width of longitudinal momentum distribution

Figure 5.11 shows the production rate as a function of the F31 slit position for one nucleus produced via projectile fragmentation (^{32}Al) and 2 by pick-up (^{34}Al and ^{35}Si).

According to the LISE code, a shift of 1mm of the F31 slit position, corresponds to 0.058% difference in longitudinal momentum. The longitudinal momentum widths of ^{32}Al, ^{34}Al and ^{35}Si are 95(5)MeV/c, 154(7)MeV/c and 135(7)MeV/c, respectively. These widths will be used to fit the polarisation curves as function of momentum distribution. Notice that the curves are measured with θ_L=0^o for ^{32}Al and ^{34}Al but with

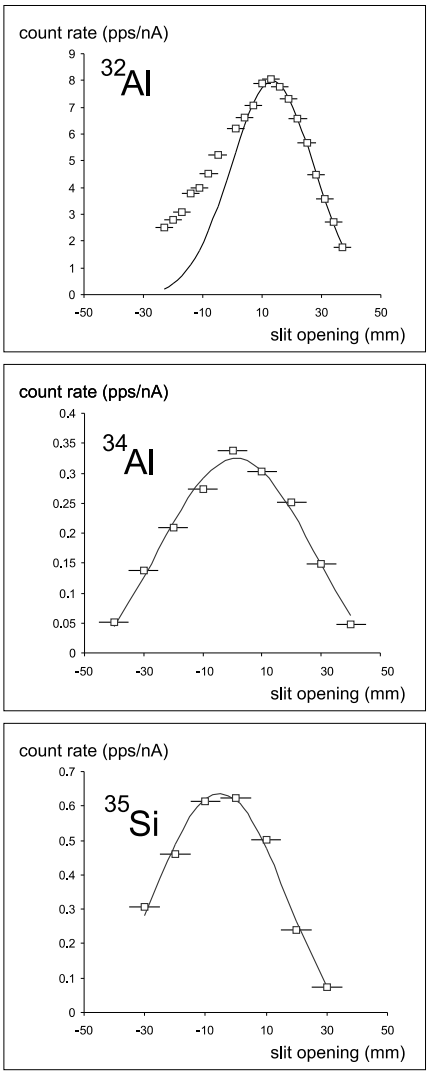

Figure 5.11: Production rate versus slit opening for ^{32}Al, ^{34}Al and ^{35}Si. A beam of ^{36}S (77.5MeV/u) is sent onto a ^{9}Be target (185 mg/cm^2). Notice that the curves are measured with θ_L=0^o for ^{32}Al and ^{34}Al but with θ_L=2^o for ^{35}Si.

θ_L=2^o for ^{35}Si. In case of ^{32}Al only the peak and the high momentum data are used to make the gaussian fit. At low momenta other reaction mechanisms come into play [102]. Using Formula 5.1, a reduced width (σ_0) of 49(3) MeV/c is obtained for ^{32}Al. For the pick-up cases, Formula 5.1 can not be used any more.

It was noticed that the position of the maximum of the yield distribution changes slightly when changing θ_L from 0^o to 2^o (see Figure 5.12). We do not have an explanation for this shift.

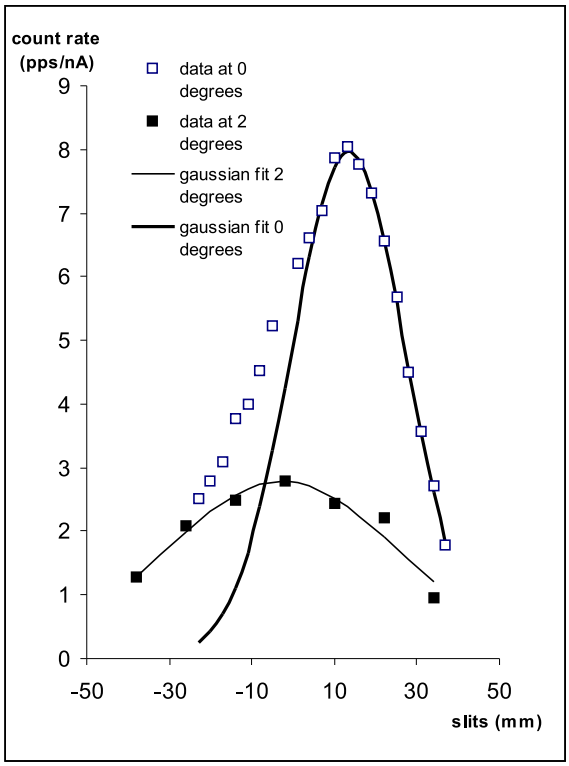

Figure 5.12: Comparison of production rate versus slit opening for ^{32}Al with θ_L=0^o and θ_L=2^o. Notice the slight shift in peak position.

5.3.2 Polarisation in a projectile fragmentation reaction

Comparison of polarisation of $^{31-32-33}$Al: spin dependence?

In July 2003 polarisation tests of ^{31}Al (I=5/2), ^{32}Al (I=1) and ^{33}Al (I=5/2) nuclei were performed as well as successful NMR scans of all three isotopes. The aim of the analysis of these data is to find out if the amount of produced polarisation depends on the spin of the formed fragment. All fragments were produced via a projectile fragmentation reaction of a ^{36}S beam (77.5MeV/u) on a ^{9}Be target (185 mg/cm^2). A wedge of 270 mg/cm^2 was used to purify the beam.

In an NMR scan, only the destruction of polarisation and not the alignment determines the height of the resonance. The amount of polarisation can be deduced from a fit of the NMR spectrum and referred to as P_{NMR}. The polarisation obtained from the fit is not equal to the initially created amount of polarisation, since part of the nuclei are not implanted at a cubic lattice site and this part of the polarisation can not be resonantly destroyed. It is assumed that the implantation properties of all the measured exotic Al isotopes are the same. The obtained P_{NMR} for different experiments are compared with the kinematical model. In order to test the dependence of produced polarisation on the spin of the observed fragment, the scaling factors used in the kinematical model have to be compared for $^{31-32-33}$Al.

In order to deduce P_{NMR} correctly from a code based on the mathematical derivation of a β-NMR experiment as explained in the previous chapter, the following parameters need to be known:

- spin of the fragment
- life time of the nucleus
- the asymmetry parameter (A_1)
- polarisation losses due to pick-up of electrons, scattering, ... (Q_{exp})
- the applied frequency (ν_{center}),
- modulation amplitude (δ) and sweep-frequency (ν_{mod})
- the gaussian line-broadening
- the RF power

Spin, life-time and A_1 of the observed nuclei are given in Figure 5.13. Since the β-decay of all three isotopes is extensively studied, a good estimate of the A_1 parameter can be deduced. Since Q_{beta} of the three isotopes is high ($>$ 8 MeV) and the electron pick-up is negligible according to LISE simulations, the Q_{exp} of ^{31,32,33}Al are all taken the same and equal to 1. The applied frequency and the modulation characteristics are written down in the logbook for every experiment. Comparing the polarisation of the 3 cases can only be done if also the gaussian line width and the linear relation between generator voltage and induced RF power is known explicitly. Both are derived from data of a different experiment in the following way.

In November 2004, two NMR field scans and three NMR frequency scans of ^{32}Al were performed, with varying values for the RF-parameters. The same set-up and implantation crystal as in July 2003 were used. In order to find the exact width of the gaussian line-broadening and the relation between RF power and input voltage, the shape and amplitude of the five scans were fit several times to P_{NMR} and gaussian line-broadening, assuming each time another linear relation between RF power and input voltage. Since the frequency scans were all measured at the same $B_0 = 0.0739$ T and the field scans were made in a very narrow field region, the gaussian line-broadening (mainly due to the inhomogeneity of the magnetic field over the beam spot) should be constant for all scans. Furthermore it is assumed that the amount of produced polarisation stays constant throughout the five measurements, since the same selection in momentum distribution was made, the set-up was not touched and the scans were taken one right after the other.

Figure 5.14 shows that the relation

$$\text{1V input voltage} = \text{0.08 gauss RF power}$$

leads to a very constant P_{NMR} and gaussian line-broadening for all five scans done at $B_0 \approx$740 gauss and ν_{RF}=1100kHz. Inside the RF-coil, a small pick-up coil is attached. The fact that 1V input voltage corresponds to 0.08 gauss when the circuit is tuned at 1100kHz and the fact that the output voltage of the pick-up coil in this case is 25 mV

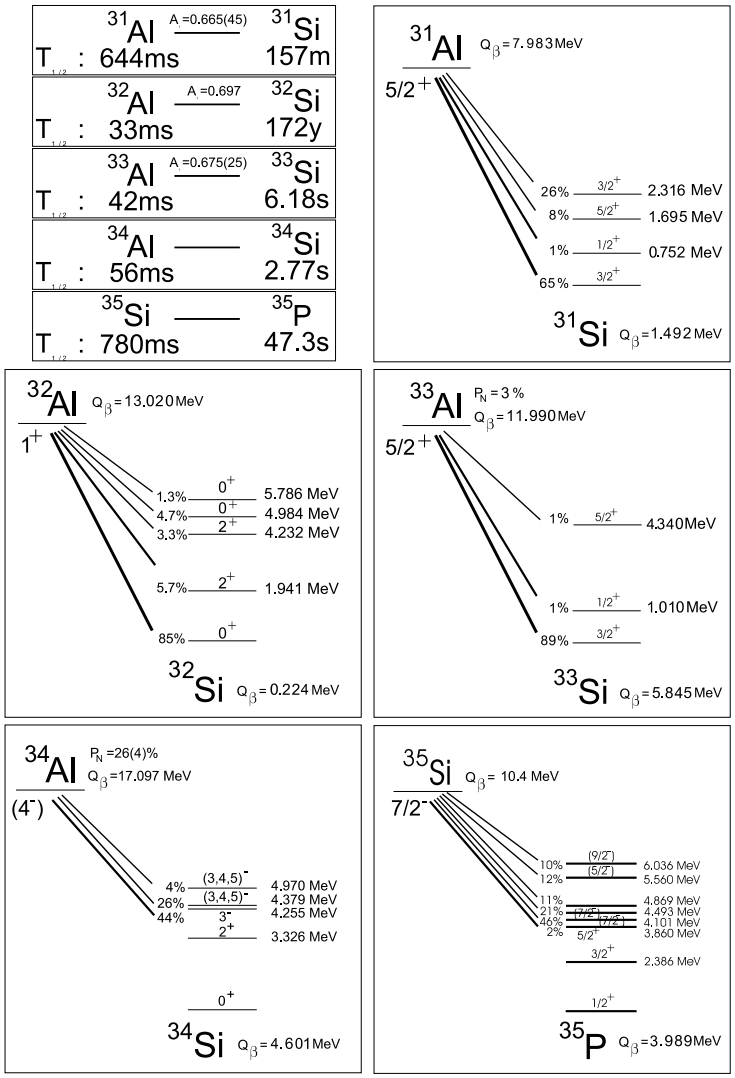

Figure 5.13: Lifetimes and β-decay schemes of ^{31,32,33,34}Al,^{35}Si.

per volt input voltage, gives us a way to determine the RF-power for every frequency ν_{RF} and input voltage V_{in} starting from the measured pick-up output voltage V_x:

$$power = 0.08 * \frac{1100}{\nu_{RF}} * \frac{V_x}{25} * V_{in} \tag{5.17}$$

with V_x in mV, V_{in} in V and ν_{RF} in kHz [103].

In this case $|P_{NMR}|$ is 4.0(4)% and the gaussian line-broadening 2.8(6) gauss. It is supposed that the gaussian line-broadening is mainly determined by the inhomogeneity of the magnet, which makes it relative to the magnetic field $B_0 = 0.0739$ T and thus equal to 0.38(8)% of the applied magnetic field.

With this relationship between input voltage and RF power and assuming the inhomogenious linebroadening to be 0.38(8)%, the NMR scans of July 2003 are fit to polarisation. Notice that this is an approximation, since different isotopes can have a slightly different gaussian linebroadening. Assuming the inhomogeneity of the magnet as the cause of the linebroadening, the width of this gaussian will depend on the size of the beam spot, which can be different for different isotopes. The fits of the NMR field scans of ^{31}Al, ^{32}Al and ^{33}Al are shown in Figure 5.15.

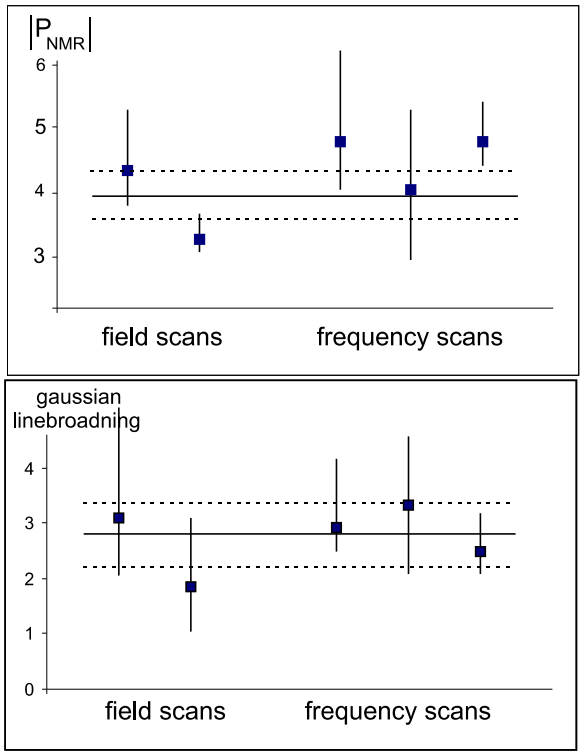

Figure 5.14: P_{NMR} and gaussian line-broadening for the five NMR scans measured in November 2004 for 0.08 gauss per input volt.

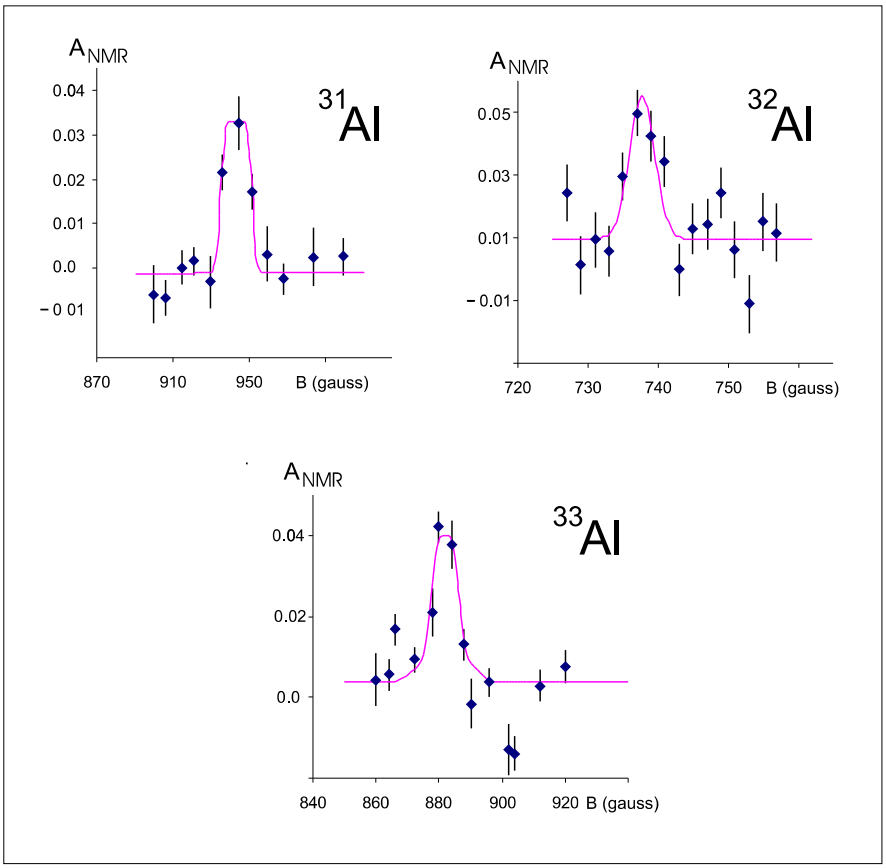

Figure 5.15: Determination of produced polarisation from NMR curves of the experiment in July 2003.

In order to compare the initial polarisation of different isotopes, these deduced P_{NMR} values are fit with the kinematical model. Table 5.2 gives the scaling factors for each of the three isotopes. These results show that the amount of polarisation for ^{32}Al is higher than of ^{31}Al and ^{33}Al.

Table 5.1: Deduction of scaling factor for ^{31,32,33}Al

	P_{NMR}	momentum (%)	scaling factor
^{31}Al	1.6(4)	2.9	0.021(5)
^{32}Al	3.2(6)	2.5	0.043(8)
^{33}Al	1.2(2)	2.6	0.017(3)

One of the reasons for this unexpected trend can be the following. For all isotopes the obtained polarisation is deduced from almost the entire coincident β-spectra. In the case of ^{31}Al and ^{33}Al, a part of these counts come from the short lived daughter nuclei with a Q_{beta} and life-time comparable to the nucleus itself . This is not the case for ^{32}Al. An overview of the lifetimes and Q_{beta} values of the examined nuclei and their descendants are tabulated in Figure 5.13.

Avoiding these daughter particles would appreciably increase the observed asymmetry difference for ^{31}Al and ^{33}Al, since they do not contribute to the amplitude of the NMR resonance. They can be avoided by for instance putting some lead foils in between the E and ΔE detectors. By cutting away the low energy part of the β-spectra, it is also possible to avoid the daughter nuclei, but also a part of the good statistics is lost. In order to get reliable results, this cutting should be done at the same energy for both detectors.

Looking at the β-spectra of ^{32}Al, a clear bump around channel number 6000 appears (Figure 5.16 a-b-c). Since β-particles lose around 3 MeV per cm plastic detector, a lot of the β-particles from the ^{32}Al-decay go through the thick E-detector. Since the Q_{beta} of the daughter of ^{32}Al is so low and the life-time so long, this peak is believed to be a ΔE-bump formed by β's of ^{32}Al going through the E-detector. This was verified by comparing the experimental β-spectra with theoretical spec-

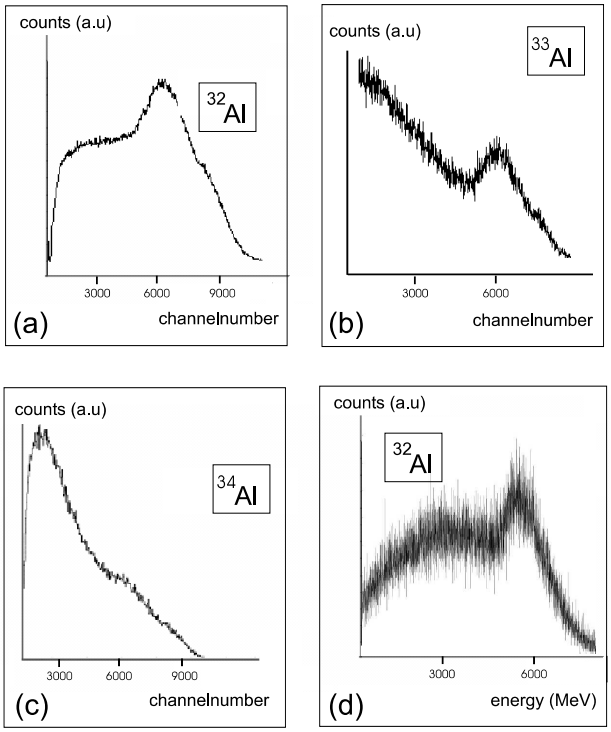

Figure 5.16: (a-b-c)β-spectrum of ^{32}Al,^{33}Al and ^{34}Al. A clear ΔE bump is present in the spectrum of ^{32}Al. Due to contamination of daughter nuclei, the bump is less visible in the spectrum of ^{33}Al and ^{34}Al. (d) Result of GEANT simulation in which a β source (Q_β=12MeV) is placed in the center of the Si-stopper crystal.

tra obtained from GEANT simulations as shown in Figure 5.16d Since both E-detectors have the same thickness, the maximum of this bump is at the same energy in both detectors and can be used to calibrate both spectra. Cutting in both spectra at a certain percentage of each peak, which is supposed to be gaussian-like shaped, is a reliable way to be sure to cut at the same energy in both detectors.

Since the Q_{beta} of ^{31}Al is appreciably smaller than the Q_{beta} of ^{32}Al, less β-particles of the decay of ^{31}Al go through the E detectors. Due to this and the fact that the spectrum of ^{31}Al is contaminated by the decay of its daughter nucleus, hardly any bump is expected. Together with the fact that not enough effort was done to tune the energy amplifiers and thresholds in a correct way for ^{31}Al, it is not possible to distinguish a ΔE-bump.

Because the Q_{beta} of the daughter of ^{33}Al is so high and so short lived, the spectrum is even more contaminated with the ^{33}Si decay than in the case of ^{31}Al and consequently the bump is rather small. Fortunately the gain of all energy amplifiers was the same for ^{32}Al and ^{33}Al, thus the same energy calibration for ^{33}Al can be used. Unfortunately this was not the case for ^{31}Al, for which isotope we thus can not make a reliable energy cut.

Figure 5.17 demonstrates that cutting at higher energy in ^{32}Al does not increase the scaling factor, but it does for ^{33}Al, because the higher the cutting the fewer daughter nuclei are taken into account. Still, the scaling factor of ^{33}Al stays somewhat lower than the scaling factor of ^{32}Al.This suggests that the production of polarisation by a projectile fragmentation can be spin dependent, since ^{31}Al and ^{33}Al both have the same spin (5/2), while I(^{32}Al)=1.

The kinematical model does not take into account the spin of the formed nucleus, nor that of the abraded nucleons. A systematic study of several nuclei with different spins and small Q_β and/or long lifetimes of their daughter nuclei, is needed to draw final conclusions.

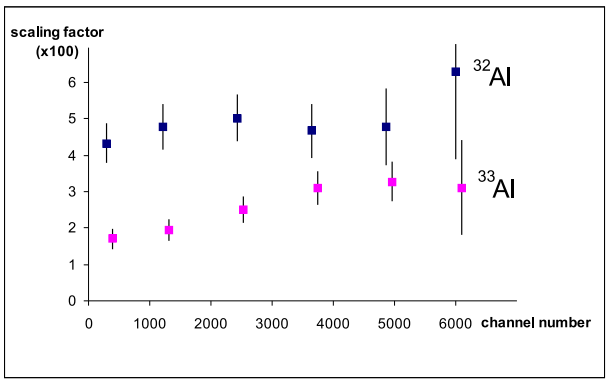

Figure 5.17: Scaling factor for ^{32}Al and ^{33}Al as function of channel number cut.

Polarisation as function of momentum

The kinematical model can explain the behavior of polarisation as a function of longitudinal momentum for a far side fragmentation reaction. This dependence was measured for a ^{32}Al beam, obtained from the fragmentation reaction of a ^{36}S beam (77.5MeV/nucleon) on a ^{9}Be target ($\approx$1mm).

The obtained polarisation, derived from NMR scans using the procedure above, together with the simulation of the kinematical model, the production rate and purity are shown in Figure 5.18.

In an internal report written by D. Borremans, it is experimentally observed that for the reactions similar to the ones investigated here, the reaction angle θ_R can be taken 0^0 or 10^0. From the simulations, shown in Figure 5.18, no firm conclusions can be made on the optimum θ_R, although θ_R=10^o seems to fit the data nicely. Notice that the fit curve only has one free parameter: the scaling factor. The other parameters, such as beam energy, selection angle (θ_L), fragment mass, ... are all fixed.

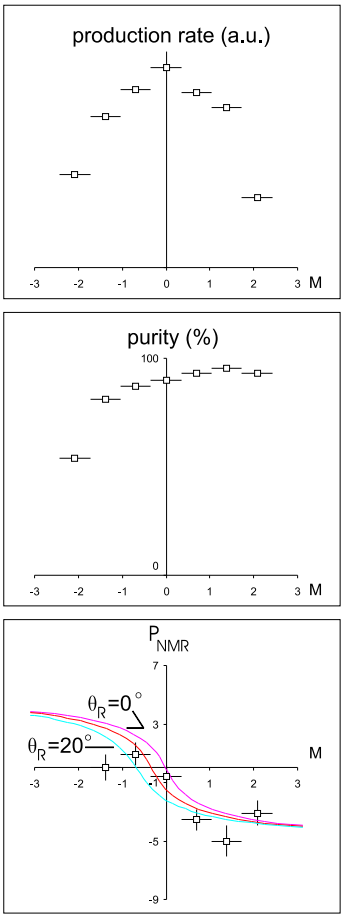

Figure 5.18: (top) Production rate (middle) Purity (bottom) Polarisation of ^{32}Al as function of momentum.

Heavy versus light target

It was shown in the explanation of the kinematical model that the polarization as a function of the momentum distribution has the same, but opposite, trend for light and heavy targets. In the case of a light (heavy) target, the nuclear attraction (Coulomb repulsion) dominates which results in a 'far side' ('near side') trajectory.

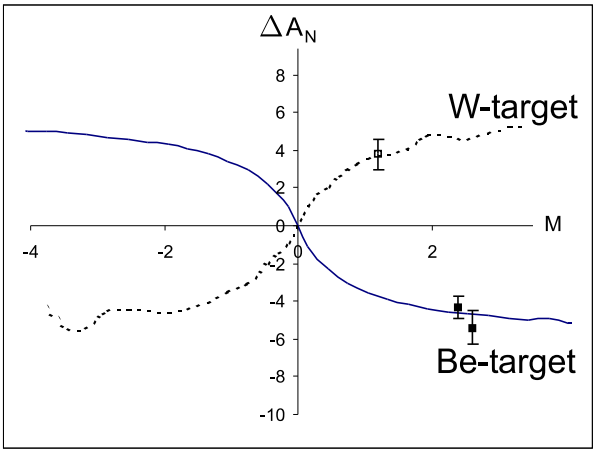

Figure 5.19: Asymmetry as function of momentum for ^{33}Al produced with W (t = 141.3μm = 273mg/cm^2) and Be (t = 1250μm = 231mg/cm^2) target. The simulations presented assume pure far side and pure near side reactions. The scaling factor is in both cases 0.067 and θ_R=0^o

This idea was confirmed by comparing the polarisation of a ^{33}Al beam produced with a 77.5 MeV/u ^{36}S beam on a ^{9}Be (t = 1250μm = 231mg/cm^2) and on a ^{184}W (t = 141.3μm = 273mg/cm^2) target. The results of the polarisation test are shown in Figure 5.19, clearly indicating that the sign of polarisation is different in both cases, as expected from the kinematical model.

LISE versus LISE2000

In March 2003, a polarised ensemble of ^{31}Al nuclei was selected by the LISE2000 beam line, which is an extension of the LISE spectrometer starting from the second dipole and ending in D4. LISE2000 has an angular acceptance of 2.5 msr and a max $B\rho$ of 4.3 Tm, while LISE has an angular acceptance of only 1.0 msr and a max $B\rho$ of 3.2 Tm [104]. This makes the LISE2000 set-up even more appropriate to select exotic neutron rich isotopes. The nuclei were guided to the NMR chamber in D4 and implanted in a Si crystal. In July of the same year, the same set-up and stopper crystal were used and ^{31}Al nuclei were selected with the LISE spectrometer and directed to D6.

Figure 5.20 shows the result of the polarisation test, together with the simulations of the kinematical model. For the LISE2000 data, a scaling factor of 0.036 is used to fit the data point, while the LISE data are in agreement with the kinematical model using a factor of 0.067.

For the LISE 2000 set-up $\theta_L = 2.5(2.12)^o$ and for the LISE set-up this angle is $2(1)^o$. It was shown in the first part of this chapter that the selection angle has an influence on the amount of polarisation that can be detected (see figure 5.5). The different selection angles for LISE and LISE2000 can only explain a difference of 10% between both and not a factor 2, as observed.

It is shown in Figure 5.20 that $\theta_R \neq 0$ can not explain the different scaling factors either. Probably the large difference has the following reason: The purity in LISE2000 (53%) was much worse than in LISE (95%). The main contaminants in the LISE2000 set-up are ^{33}Si (20%), ^{29}Mg(8%), ^{30}Mg(7%) and ^{32}Al(7%). Since all the statistics of the coincident β-spectra are taken into account to calculate A_N, also these contaminants determine the observed asymmetry difference. Notice that all these contaminants can also be polarised by the reaction. According to LISE simulations, if the Bρ is chosen such that ^{31}Al fragments are selected in the right wing of the momentum distribution, then this means a selection around the center for ^{29}Mg, ^{30}Mg and ^{32}Al, while for ^{33}Si the outer right part of the wing is selected. Consequently the selected ^{29}Mg, ^{30}Mg and ^{32}Al nuclei are not polarised and thus decrease

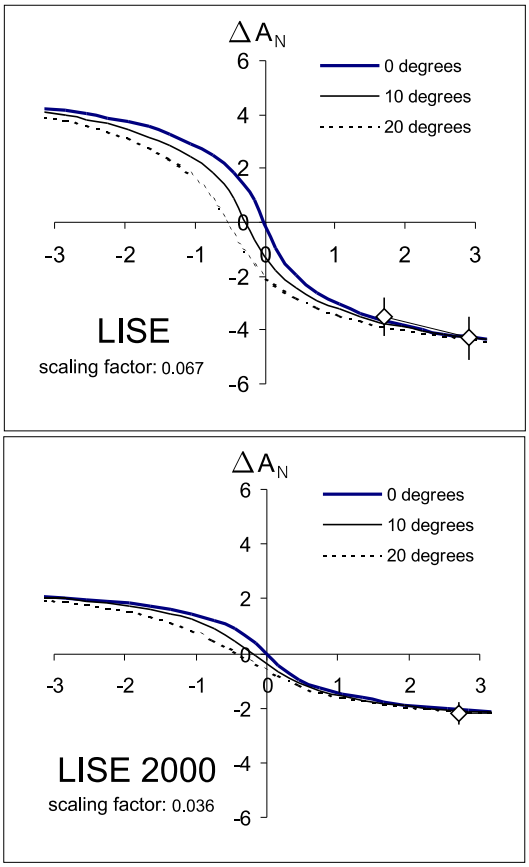

Figure 5.20: Asymmetry as function of momentum for ^{31}Al at LISE2000 and LISE beamline.

the amount of asymmetry observed in the polarisation test. Notice that the A_1 parameter of ^{33}Si (β-decay: $3/2^+ \rightarrow 5/2^+$) has the opposite sign of the A_1 parameter of ^{31}Al (β-decay: $5/2^+ \rightarrow 3/2^+$). This means that ^{33}Si reduces the amount of observed asymmetry drastically.

Making cuts in the β-spectra obtained from the LISE 2000 set-up, does not increase the polarisation, since the Q_β values of the contaminants are of the same energy as the Q_β of ^{31}Al.

5.3.3 Polarisation in pick-up reaction: the cases ^{34}Al and ^{35}Si

^{34}Al: polarisation tests as function of momentum

In July 2003 also ^{34}Al was produced via the $^{9}Be(^{36}S,^{11}N)^{34}Al$ reaction. In the kinematical model we assume that this reaction is a one neutron pick-up reaction followed by the evaporation of 3 protons. A polarisation test with $B_0 = 0$, 0.06 and 0.08 T was performed at three different cuts in the momentum distribution. The change in momentum selection was done by changing the target angle.

In November 2004 the same experiment, with more statistics, was repeated. This time, the change in momentum selection was made by changing the slit position.

In both experiments, ^{32}Al was first selected and the gains were untouched so that the ΔE bump could be used to perform the energy calibration. The results are shown in Figure 5.21 and described in more detail in [93]. The energy cut was taken at 50% of the ΔE bump, since this was found to be the optimum between observed asymmetry and error bar.

The main decay branch of ^{34}Al has a Q_β=14MeV, which is similar to the main decay branch energy of ^{32}Al. A clear ΔE-bump is thus expected. But, similar to ^{33}Al, the low energy β-particles of daughter and granddaughter nuclei of ^{34}Al reduce the bump drastically as shown in Figure 5.16 right.

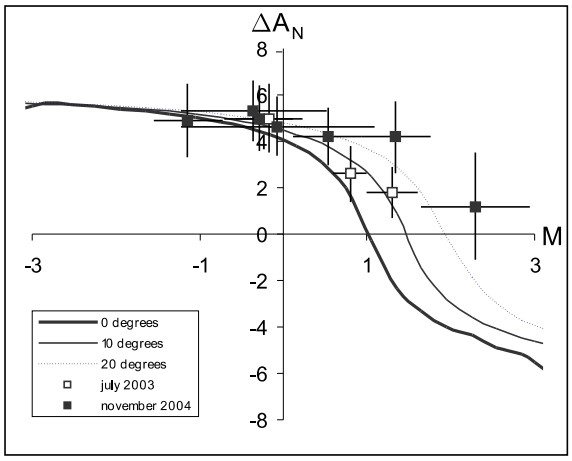

Figure 5.21: Asymmetry from polarisation tests on ^{34}Al. The data from July 2003 (November 2004) are represented with open(closed) squares. A fit with different reaction angles is made. ΔA_N (= the normalised asymmetry difference between low and high external field) is defined in formula 5.13. The scaling factor is 0.073.

A simulation with the kinematical model for pick-up reactions with $\theta_R = 20^o$ nicely reproduces the experimental data of July 2003 and November 2004 (Figure 5.21). Notice the observed polarisation at the center of the momentum distribution in contrast with the projectile fragmentation reaction.

Notice that part of ΔA_N that is observed, can be due to the alignment component in the nuclear ensemble, since the data are taken from a polarisation test and not a NMR measurement. Still, the trend of polarisation as function of momentum is reproduced well by the kinematical model, not taking into account alignment.

^{35}Si: NMR scans as function of momentum

Apart from ^{34}Al, also ^{35}Si was produced via a pick-up reaction of a ^{36}S beam on the same ^{9}Be target (one neutron pick-up and two proton evaporation). First the g-factor was measured accurately (described in the next chapter) after which frequency NMR scans were made at different places in the momentum distribution. Figure 5.22 shows the initial asymmetry derived from the fits of the NMR spectra as a function of the fragment momentum and the simulation of the kinematical code with a scaling factor 0.029. The ratio of polarisation over error is optimal when taking a energy cut at 12.5% of the gaussian ΔE-bump of ^{32}Al. (Notice that the highest NMR amplitude was observed at 25% of this bump, resulting in a scaling factor for ΔA_{NMR} of 0.051.)

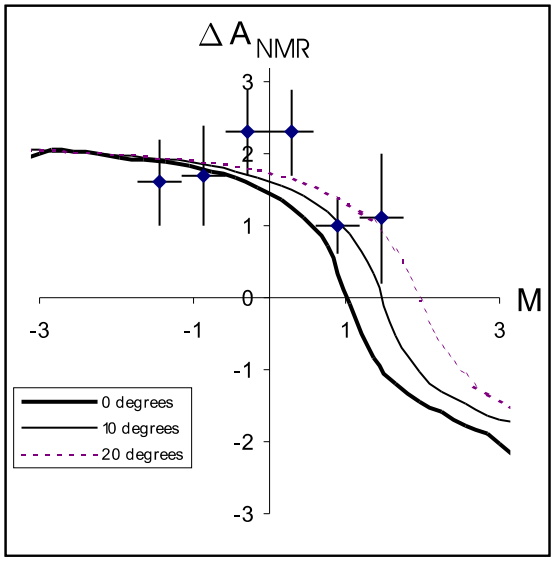

Figure 5.22: ΔA$_{NMR}$ of ^{35}Si as function of momentum. ΔA$_{NMR}$ (= the normalised asymmetry difference between RF on and the baseline) is defined in formula 4.34. The scaling factor is 0.029.

^{34}Al and ^{35}Si: comparison of the amount of polarisation

In order to calculate the polarisation from ΔA_{NMR}, A_1 is needed since $\Delta A_{NMR} \approx -2A_1 P_I \sqrt{\frac{3I}{I+1}} Q_{exp}$. The β-decay of ^{35}Si is shown in Figure 5.13. Calculations with the ANTOINE code using the interaction described in [105] made by Warburton et al. [106], resulted in $A_1 = 0.21$. Assuming perfect implantation behavior and no polarisation losses due to scattering ($Q_{exp} = 1$), the amount of created polarisation is 6(1)%, using the highest NMR amplitude, and the scaling factor for P_{NMR} of 0.08(1).

The g-factor of ^{34}Al was measured during the same experiment as for ^{35}Si. The fit of the NMR frequency scan of ^{34}Al with the best energy cut resulted in ΔA_{NMR}=2.5(5)%. The A_1 parameter is deduced from the β-decay of ^{34}Al (see Figure 5.13), using three decay branches: 26% β-delayed neutron decay, 44% to a 3^- level at 4255keV and 26% to a level at 4379keV. The spin of the final state of the third decay mode can be 3^-,4^- or 5^-. Taking into account these three decay modes, the different possible A_1 and P_{NMR} are calculated in the table below.

Table 5.2: Possible A_1 and P_{NMR} values for ^{34}Al

spin of 3th excited level	A_1	P_{NMR}(%)	scaling factor
3-	0.41	2.0(4)	0.027(5)
4-	0.15-0.41	2.0(4)-5.5(1.1)	0.027(5)-0.074(13)
5-	0.15	5.5(1.1)	0.074(13)

Since the same target was used and the spins are similar (I(^{34}Al) = 4 and I(^{35}Si) = 7/2), we expect that the amount of polarisation is similar for both nuclei. This suggests that it is unlikely that the spin of the third excited state of ^{34}Si is 3^-.

Notice that a ground state spin of 5^- for ^{34}Al would result in a scaling factor of 0.056 (assuming the spin of the 3th and 4th excited level of ^{34}Si to be 4^-), which is not impossible. Other spin-parity assumptions for the 3th and 4th excited level of ^{34}Si would result in much higher

polarisation. But a decay branch of 44% from a 5^- to a 3^- state is very unlikely.

Comparing these amounts of polarisation:

$$P_{NMR}(^{34}Al) = 2 - 7\% \tag{5.18}$$

$$P_{NMR}(^{35}Si) \sim 6\% \tag{5.19}$$

with the results from the exotic Al isotopes produced via projectile fragmentation ($P_{NMR}(^{32}Al) \sim 4\%$), it is seen that the pick-up reaction mechanism produces at least as much (or even more) polarisation than the projectile fragmentation reaction. Notice again that in the case of pick-up, the fragments can be selected in the center of the momentum distribution, where the production rate is maximal, while the fragments from projectile fragmentation are only maximal polarised in the wing of the distribution. We thus conclude that pick-up reaction is a very interesting tool to produce neutron rich exotic nuclei, with a high degree of polarisation and a good production rate.

LISE simulations

The beam energy, target thickness and wedge thickness are needed to calculate the $B\rho_1$ and $B\rho_2$ value to select the desired nucleus. The production rate as function of longitudinal momentum was measured for ^{31,32,33}Al and the maximum of the yield curve is within 0.2% in agreement with the LISE code. In the case of ^{34}Al and ^{35}Si, the suggested $B\rho_1$ value is respectively 1.3% and 1.7% higher than the optimal values found during the experiment. These results are shown for ^{34}Al in Figure 5.23.

The LISE program wrongly assumes that the ^{36}S $+^{9}$Be$\rightarrow$ ^{34}Al,^{35}Si reaction is a fragmentation reaction. It is thus expected that the relation between the projectile and the observed fragment is $(\bar{p}_p)_x = \frac{m_p}{m_f}(\bar{p}_f)_x$.

In reality, this relation is different, since ^{34}Al and ^{35}Si are produced via a pick-up reaction. The relation should be $(\bar{p}_f)_x = \frac{m_f}{m_p}(\bar{p}_p)_x + \frac{m_f}{m_f^*} < (\bar{k})_x >$, with $< (\bar{k})_x >$=-152MeV/c.

Since $< (\bar{p}_p)_x > = 13$ GeV, the difference between the LISE simulations for a pick-up reaction and the measured momenta should be positive and equal to 1.2%, in reasonable agreement with the experimentally observed difference.

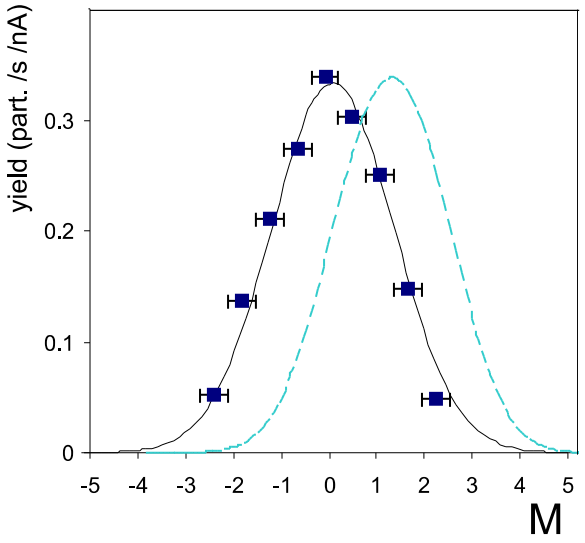

Figure 5.23: Comparison of experimentally observed production rate for ^{34}Al as function of longitudinal momentum with LISE simulations. The shift can be explained by the pick-up mechanism as explained in the text.

5.4 Preserving the polarisation

5.4.1 Decoupling curve

It was noticed above that a polarisation test is not a good tool to derive the amount of polarisation. In case the g-factor is not known, it is however the only way to obtain a first idea of the orientation in the beam.

Besides at least the proof that orientation is present in the beam, a full decoupling curve (= the β-asymmetry as function of the externally applied static magnetic field - see Section 5.2) is measured for a second reason. Only at fields when this decoupling is completed, the maximum amount of polarisation is maintained, which is the necessary condition to measure a g-factor efficiently. In order to know at which field the decoupling is completed, the asymmetry should be measured at different high fields. Such a full decoupling curve is measured for ^{32}Al in Si and shown in Figure 5.24. From this measurement, it is decided to perform g-factor measurements at $B_0 > 0.08T$ in this crystal.

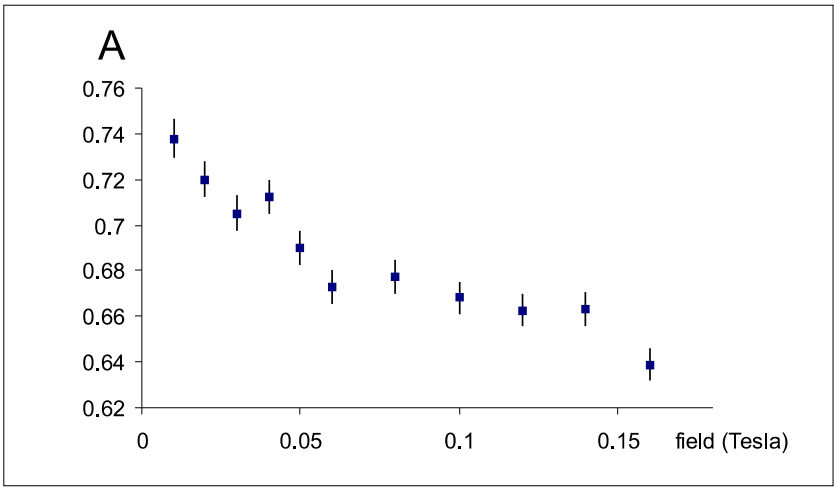

Figure 5.24: Decoupling curve of ^{32}Al in Si. A = N_{up}/N_{down}

5.4.2 Crystals

Several materials were tested as a stopper crystal in order to find the type with the best implantation properties for Al-isotopes. A ^{31}Al and ^{29}Mg beam were implanted in NaCl, MgO and Si, all with cubic lattice symmetry. Polarisation tests were performed for each crystal and the results are summarized in Figure 5.25.

This test shows that Si is the best crystal out of this list to implant Al in. As a general rule [107], the smaller the difference in atomic radius and electronegativity between host and implantation nucleus the better the implantation. Since the atomic radius of Al is more similar to Si than to Na, Mg and O, and since the electronegativity difference between Al and Si is only 0.29, the combination of Al(Si) is obvious (see Table 5.4). For the determination of the g-factor of all the neutron rich Al-isotopes, Si was used as an implantation crystal.

As expected, the implantation properties of Mg(MgO) are better than in the other crystals. Obviously, in order to measure the g-factor of ^{35}Si, the Si crystal was used as well.

Table 5.3: Difference of atomic radii and electronegativity (E.N.) between Al, Mg and several implantation crystals.

Al(crystal)	ΔE.N.	Δatomic radius (A)
Al(Si)	0.29	0.15
Al(Mg)	0.30	0.25
Al(Na)	0.68	0.55
Al(Cl)	1.55	0.25
Mg(Si)	0.59	0.40
Mg(Mg)	0	0
Mg(Na)	0.38	0.30
Mg(Cl)	1.85	0.50

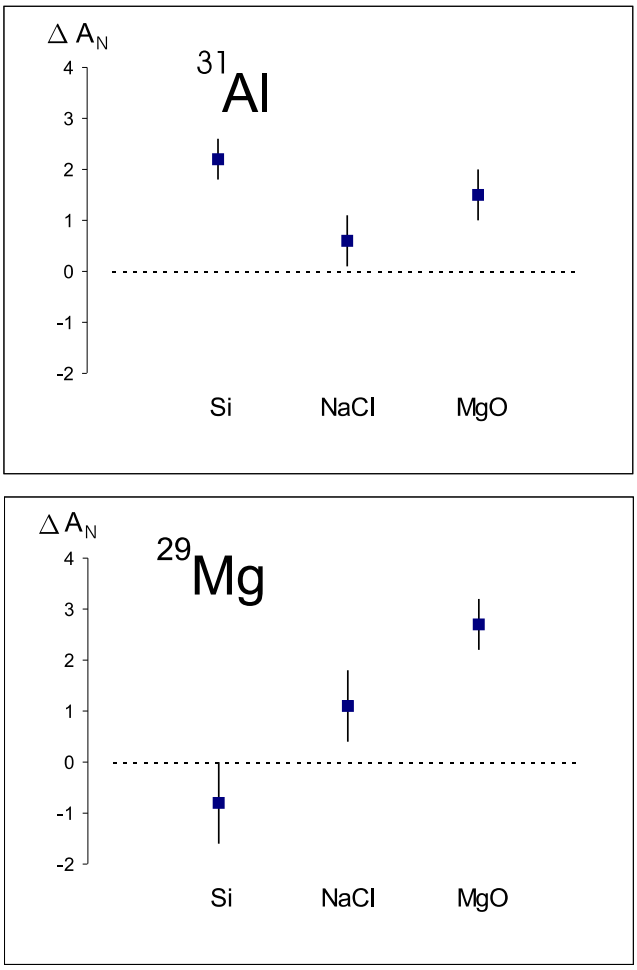

Figure 5.25: Asymmetry in different crystals for ^{29}Mg and ^{31}Al.

5.5 Conclusion

In this chapter, solely devoted to the aspect 'polarisation', the kinematical model is introduced for fragmentation reactions and pick-up reactions. This model was tested in several ways, in order to find the best conditions for NMR measurements: high production rate combined with an as high production and maintenance of polarisation as possible.

A polarisation curve of ^{32}Al, produced via projectile fragmentation, was measured, concluding that the model reproduces the correct trend as function of momentum.

A comparison between $^{31-32-33}$Al was made, concluding that the decay of the daughter nuclei severely decreases the amount of polarisation detected.

Two examples of pick-up reactions are described, from which it is concluded that this reaction mechanism produces at least as much polarisation as the fragmentation reaction. A second advantage of pick-up is the presence of polarisation at the center of the momentum distribution.

It was proven experimentally that the polarisation changes sign when a light target is replaced by a heavy target, as expected from the kinematical model.

From the measurement of a full decoupling curve and from polarisation tests in several crystals, the decision was taken to measure the g-factor of Al-isotopes in a Si-crystal at $B_0 > 0.08T$, in order to preserve the created polarisation as much as possible.

Chapter 6

g-factors from NMR measurements

In the fifth chapter the method to produce and maintain polarisation is explained and optimized. In the fourth chapter it was shown mathematically what are the best conditions to destroy the polarisation. Thus, now g-factor measurements can be performed in an efficient way.

In this chapter, the method to determine the statistical and systematic error on the g-factor is worked out for the NMR scans of ^{32}Al. The same procedure is used to obtain the final g-factor results of the other measured nuclei: ^{31}Al,^{33}Al,^{34}Al and ^{35}Si.

6.1 ^{32}Al

In July 2003, using the NMR technique as function of field, the g-factor of ^{32}Al was measured for the first time. Since the g-factor was not known prior to this, first a very broad g-factor range was scanned (see Figure 6.1). The frequency modulation in the first scan was 50 kHz. The g-factor derived from this scan is 1.94(7). The large modulation (5%) is the main contributor to the error. The statistical error is neglected.

Following this first measurement, the g-factor of ^{32}Al was measured eight times with much better statistics and less modulation. Three times

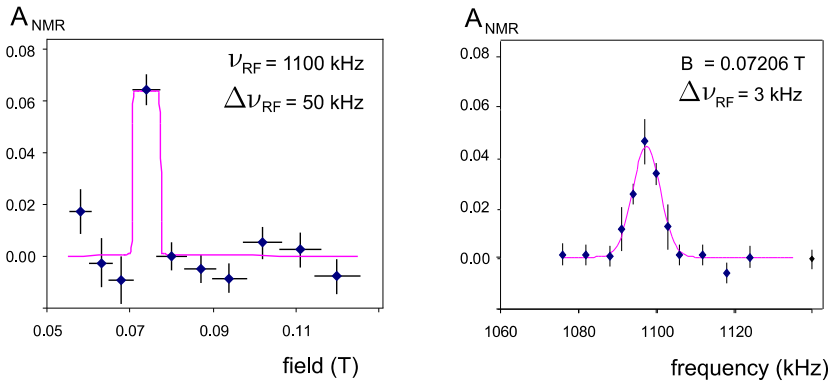

Figure 6.1: NMR scans of ^{32}Al

a scan as function of field and five times a frequency scan was made. Figure 6.1 (left) shows the first field scan on ^{32}Al, while Figure 6.1 (right) presents data from a very precise measurement as function of frequency.

Besides the g-factor, the amount of polarisation, RF power and the line-broadening, the other parameters needed to fit the NMR curve (lifetime, ground state spin, frequency modulation and amplitude modulation) are known.

In the previous chapter the gaussian line-broadening (0.38(8)%) and the formula to derive the RF power were deduced. For every experiment and each examined nucleus, the linear relation between input voltage and RF power produced is the same, since the same coil was used throughout all experiments. The gaussian line-broadening strongly depends on the shape (width and height) of the beam spot. Since the beam spot is reshaped with different quadrupoles and stearers, the gaussian line-broadening does not have to be the same in different experiments and for different nuclei.

In order to deduce the statistical 1 σ error of the measured g-factor, first a χ^2-square plot of polarisation versus line broadening is made, for different fixed g-factors. From these fits χ^2_{min} is deduced. The lower (higher) limit of g is defined as the lowest (highest) g-factor for

which a polarisation and a gaussian linewidth can be found, so that the $\chi^2 < \chi^2_{min} + \chi^2_{red}$ with $\chi^2_{red} = \frac{\chi^2_{min}}{(N-1)}$ and N the number of datapoints. This procedure is shown schematically in Figure 6.2 and results in a statistical error δ_1. In a next step, the relation between input voltage and RF power was changed slightly and all the fits were redone, which results in statistical errors $\delta_2, \delta_3, ...$ The largest δ_i was taken as final statistical 1 σ error for the g-factor of the ground state of ^{32}Al.

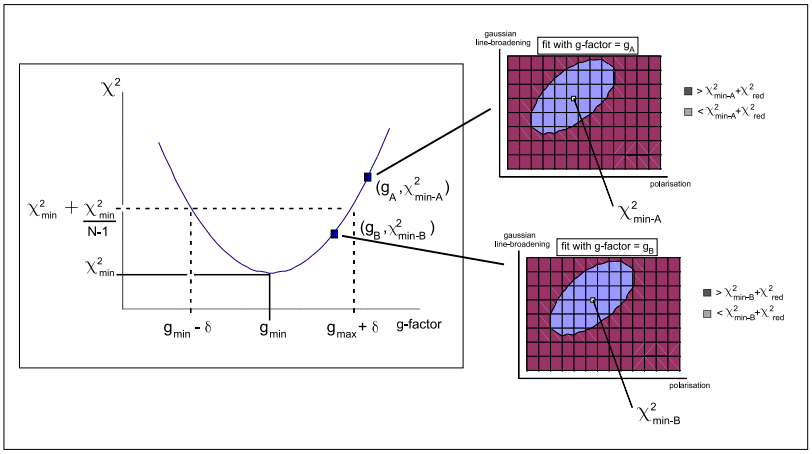

Figure 6.2: Schematical overview of fitting procedure to determine the statistical error on measured g-factors. For each g-factor value, a χ^2-plot is made (gaussian line-broadening versus polarisation). The minimal χ^2 of each of these plots is put on a graph which presents g-factor versus χ^2. On the figure, δ represents the 1 σ error derived with this method.

In total, the g-factor of ^{32}Al was measured eight times over four different experiments with the precision of Figure 6.1(right). Figure **??** (left) presents the results of five measurements obtained during the same experiment. The errors quoted in this figures are purely statistical. This figure shows that within one experiment, the obtained g-factors are consistent within the statistical uncertainty, leading to g = 1.9516(4) (using the weighted mean formulae).

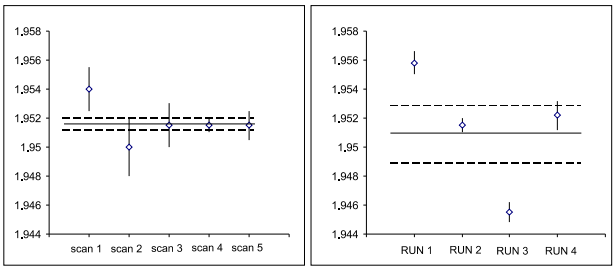

Figure 6.3: (a) *left*: all g-factor results from 1 run (b)*right*: most precise g-factor results of ^{32}Al from each run, with experimental standard deviation

Figure 6.3 (right) shows the most precise result from each run (referred to as y_i with statistical error σ_i). The full line represents the weighted average (=m) of the four (=N) measurements. If the scattering is purely statistical a χ^2_{red} around 1 is expected, with

$$\chi^2_{red} = \frac{\sum(y_i - m)^2/\sigma_i^2}{(N-1)} \tag{6.1}$$

The χ^2_{red} of this fit is 33, which shows the necessity of taking into account a systematic error. This means that the final error is determined by the experimental standard deviation σ_A, defined as

$$\sigma_A = [\frac{\sum(y_i - m)^2/\sigma_i^2}{(N-1)\sum(1/\sigma_i^2)}]^{1/2} \tag{6.2}$$

which is 0.0021 (or 0.11%) in this case. This error represents the combination of statistical and systematic error. Since the statistical error for ^{32}Al is much smaller than 0.0021, the systematic error is taken as 0.0021.

To determine the error on the g-factor of the other isotopes, the same systematic error is used. The total error (=σ_{total}) for ^{31,33,34}Al and ^{35}Si is derived using formula 6.3.

$$\sigma_{total} = \sqrt{\sigma_A^2 + \sigma^2_{statistical}} \tag{6.3}$$

This systematic error is most probably due to an error related to the calibration of the magnetic field and also due to the inhomogeneity of the static magnetic field:

1. To calibrate the magnetic field, the Hall Probe is first put at the place of the crystal. A mismatch of 1 mm between the Hall Probe position and the crystal position results in an error of 0.03%. Putting the Hall Probe not in a perfect horizontal position induces again an extra error.

2. Since the difference of B_0 for the extremities of the beam spot is $\sim 1\%$, nuclei from a slightly off-centered beam spot will feel a different B_0 when implanted in the stopper crystal. If the beam is not well centered, a few millimeters deviation can explain the observed systematic error.

Taking into account this systematic error, g(^{32}Al) = 1.952(2)

6.2 ^{31}Al

In 2001 the g-factor of the ground state of ^{31}Al was measured using the NMR method as function of field with 12kHz frequency modulation on a basic frequency of 1000 kHz. This result is published in [66] and details from the experiment are extensively discussed in the thesis work of S.Teugels. The derived g-factor was 1.517(20).

In July 2003, this g-factor was remeasured, using the same technique (NMR as function of field), beam and target ($^{36}S^{16+}$ primary beam (77.5 MeV/u) on a rotating ^{9}Be target (1250μm)), but with less frequency modulation (10 kHz) and more statistics, shown in Figure 6.4.

The g-factor derived from the fit, using the same procedure as for ^{32}Al, is 1.5315(8). We add an error of 0.11% to this statistical error, in order to take into account the systematic error. The final value is then 1.532(2), an order of magnitude more accurate and in agreement with the previous value.

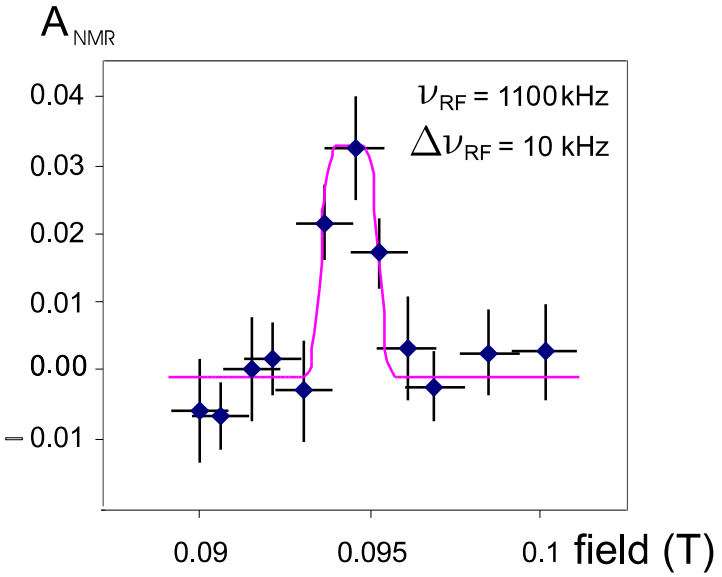

Figure 6.4: NMR field scan of ^{31}Al

6.3 ^{33}Al

In July 2003, the g-factor of ^{33}Al was measured with the NMR technique as function of field. First a broad field scan was made, since the g-factor was not known before. This result is shown in Figure 6.5 (left), which shows that around 0.088T an asymmetry change of 4% is observed with respect to the baseline. Next a zoom of this region was investigated (Figure 6.5 (right)) with $\Delta\nu = 6kHz$. The g-factor deduced from a fit to this dataset is 1.635(2), including the systematic error of 0.11%.

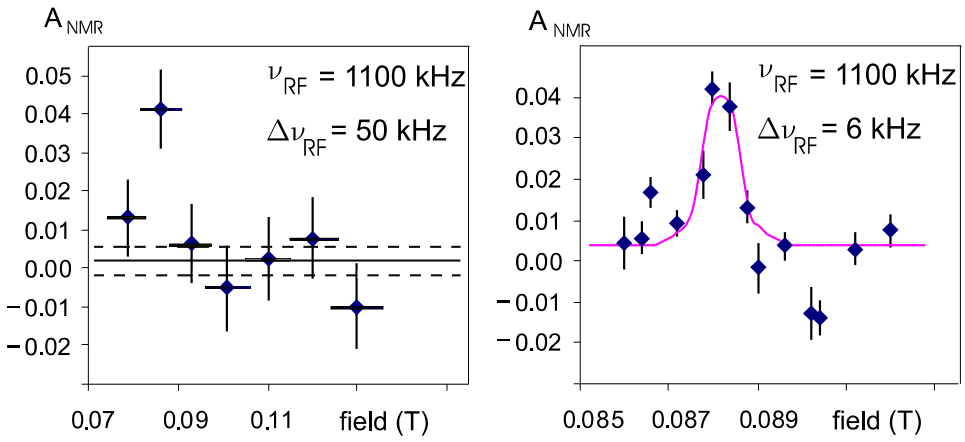

Figure 6.5: NMR scans as function of field of ^{33}Al

6.4 ^{34}Al

In November 2004 a first attempt was made to measure the g-factor of ^{34}Al with a NMR scan as function of frequency. In the first scan one data point might be out of the baseline, corresponding to g = 0.511(34). A finescan around this frequency, with less modulation, revealed again the onset of some resonant behavior with g = 0.535(15). These data are shown in Figure 6.6, first separately and then on the same picture, where each time the data are normalised to the average of the asymmetry observed in the RF off point and the points clearly outside the resonance.

In September 2005 this indication was confirmed with 2 fine-scans as function of frequency. These data are presented in Figure 6.7. The g-factor deduced from these scans is 0.536(5) and 0.5406(7). The final value is 0.541(1) if the systematic error is taken into account.

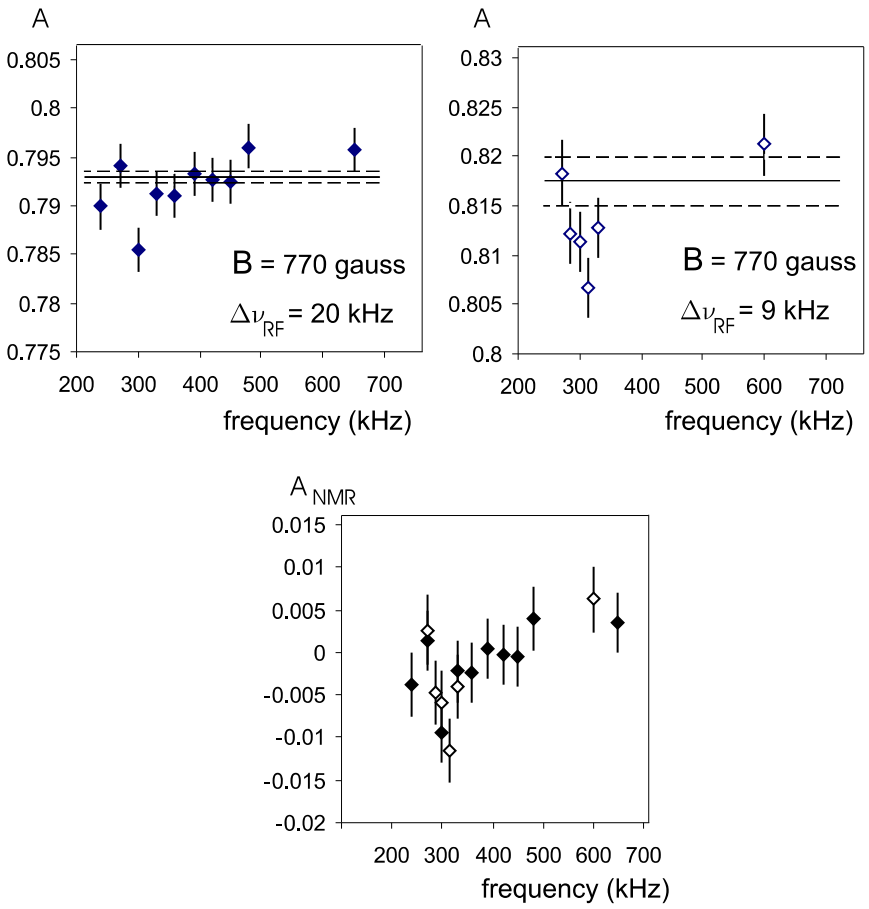

Figure 6.6: First indication of NMR resonance of ^{34}Al

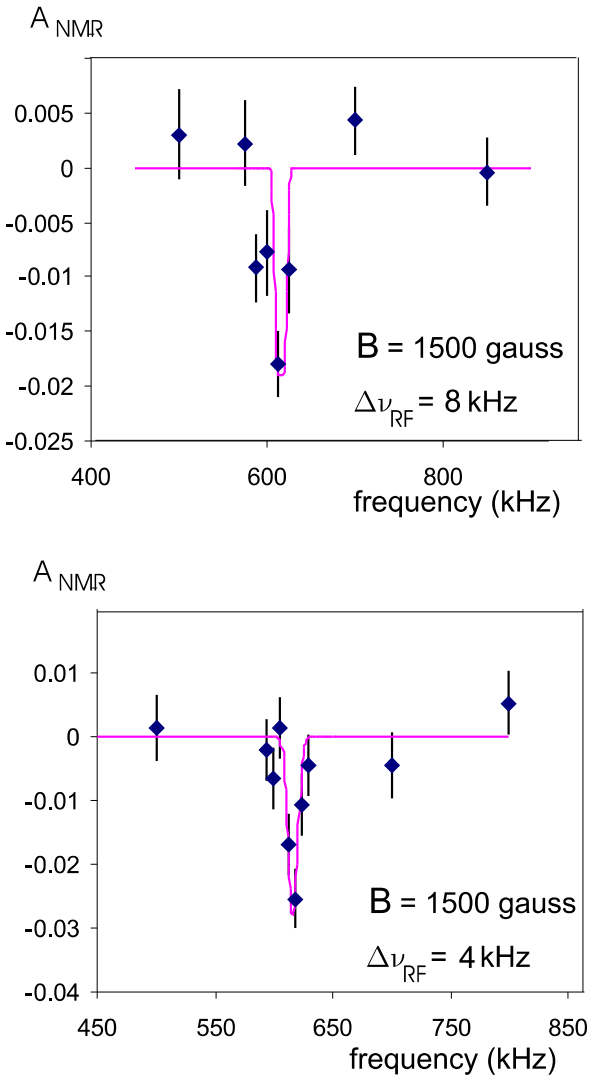

Figure 6.7: NMR resonances of ^{34}Al

6.5 ^{35}Si

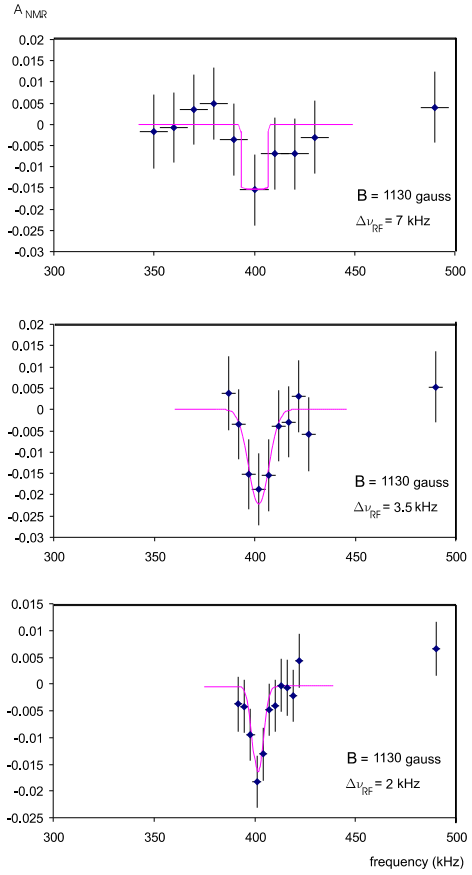

Figure 6.8: NMR resonances of ^{35}Si

In September 2005, the g-factor of ^{35}Si was measured with the NMR technique as function of frequency. First a broad frequency scan was taken, since the g-factor was not known before. Next several zooms of this region were investigated (Figure 6.8) with $\Delta\nu = 2kHz$ as smallest modulation. The g-factor deduced from the first fine scan is 0.469(2) and 0.4683(5) is the result from the finest scan. The final g-factor, taking into account the systematic error is 0.468(1).

Chapter 7

Interpretation of g-factor results

For each exotic nucleus that was investigated, first a comparison between measured nuclear properties (such as spin, parity and level scheme) and theoretical shell model calculations is given. This is followed by the physical insight added to these findings through the measurement of the g-factor. This insight mainly comes from intuitive ideas and comparison of the experimental g-factors with large scale shell model calculations with different interactions and model spaces. When the experimental data are compared with theoretical predictions, three interactions are used:

1. The USD interaction, as described in the second chapter, is developed starting from the (near to) stable nuclei in the $8 \leq N, Z \leq 20$ region, taking ${}^{16}_{8}O_8$ as an inert core. The remaining nucleons are free to move in the full $\nu(d_{5/2}s_{1/2}d_{3/2})$ and $\pi(d_{5/2}s_{1/2}d_{3/2})$ subshells.

2. The sdpf-sm interaction, introduced in [24], is defined in the full $\nu(d_{5/2}s_{1/2}d_{3/2} - f_{7/2}p_{3/2}f_{5/2}p_{1/2})$ and $\pi(d_{5/2}s_{1/2}d_{3/2} - f_{7/2}p_{3/2}f_{5/2}p_{1/2})$ model space. The parameters of this interaction are derived from more recent measurements performed on more exotic nuclei in this region. Due to computational inadequacy this complete model space without restrictions on the number of excitations can not be used. Unless otherwise mentioned, the model space is restricted to the $\nu(d_{5/2}s_{1/2}d_{3/2} - f_{7/2}p_{3/2})$

and the $\pi(d_{5/2}s_{1/2}d_{3/2})$ orbitals and a maximum of 2 neutrons allowed to excite across N = 20. Calculations for pure intruder configurations are performed with exactly 2 neutrons fixed in the $\nu(f_{7/2}p_{3/2})$ sub-shell. Notice that the sd part of the sdpf-sm interaction is not exactly the same as the USD interaction, since more exotic nuclei were taken into account in the derivation of the former.

3. A third interaction, the SDPF-M interaction using the Monte Carlo Shell Model approach (MCSM), has $\nu(d_{5/2}s_{1/2}d_{3/2}-f_{7/2}p_{3/2})$ and $\pi(d_{5/2}s_{1/2}d_{3/2})$ as valence space. Since the mathematical procedure to obtain the eigenstates is different for the ANTOINE code and the MCSM code, the latter can be used without restriction on excitations from the $\nu(d_{5/2}s_{1/2}d_{3/2})$ to the $\nu(f_{7/2}p_{3/2})$ orbitals.

The first two interactions are implemented in the ANTOINE code, which is freely distributed. So the calculations using these interactions are performed by the author. On the other hand, the results from the MCSM code are taken from several publications, since this code and method are not available.

In some cases, it can be enlightening to investigate the influence of changes of the single particle energies of certain orbits as well as changes in the monopole interaction terms on the g-factor and/or energies of excited levels. Such changes are made throughout this chapter. Notice that these changes are purely informative and should not be taken as the correct way to proceed in order to come to a better shell model interaction for this region.

7.1 ^{30}Al and ^{32}Al

Figure 7.1 shows a comparison between the experimental and theoretical level scheme of ^{30,32}Al using the ANTOINE code. For ^{30}Al a very good agreement is observed for the g-factor and the excitation spectrum with both the USD and the sdpf-sm interaction allowing 2 neutrons to excite across N = 20.

In the case of $^{32}_{13}Al_{19}$, the measured g-factor is slightly higher than both theoretical values. An inversion of the 2^+ and 4^+ state is also apparent in both interactions, while the odd neutron particle - odd neutron hole 4^- level is predicted in reasonable agreement with the experimental value. This observation already indicates that the width of the N = 20 shell gap and the cross-shell proton neutron interaction $(\pi(sd) - \nu(pf))$ for ^{32}Al in the sdpf-sm interaction is rather good. Using the USD interaction this latter state is not observed, since the model space of this interaction is limited to the sd-shells for protons and neutrons.

Since the ground-state spin of ^{32}Al is fixed at 1^+, due to the large decay rate to the 0^+ ground state of ^{32}Si, the ground state can not be influenced by an odd particle - odd hole configuration with negative parity.

The pure 2p-2h configuration, using the $\nu(f_{7/2}p_{3/2})$ sub shell as valence space, results in $g_{theory} = 0.495$. The fact that the experimental g-factor is slightly higher than the theoretical g-factor within the normal configuration, can thus not be explained by ν(2p-2h) mixing into the ground state of ^{32}Al. A ground-state with some intruder components would probably result in a g-factor between 1.834 and 0.495. This idea is confirmed when looking at the calculations for g_{theory} with allowing 2p-2h excitations: introducing these intruder components in the ground state wave function lowers the g-factor from 1.834 to 1.826. In this case, the decrease is small, showing only a small amount of intruder components according to the sdpf-sm calculations.

Since the only proton-neutron coupling resulting in a pure g-factor higher than the experimental g-factor is $\pi(d_{5/2})\nu(d_{3/2})$, more of this component in the wave function should higher the theoretical g-factor. This idea is confirmed by looking at calculations made in a restricted proton model space: in the full $\pi(sd)$-space $g_{theory} = 1.834$, while in the restricted $\pi(d_{5/2})$-space $g_{theory} = 2.181$, as shown in Figure 7.2. Notice that the contribution of the $\pi(s_{1/2})$ level to the g-factor is negligible since $g_{theory} = 2.227$ in the restricted $\pi(d_{5/2}s_{1/2})$-space.

On the other hand, in explaining the inversion of the 2^+ and 4^+ states in ^{32}Al, the contribution of the $\pi(s_{1/2})$ and $\nu(s_{1/2})$ is important.

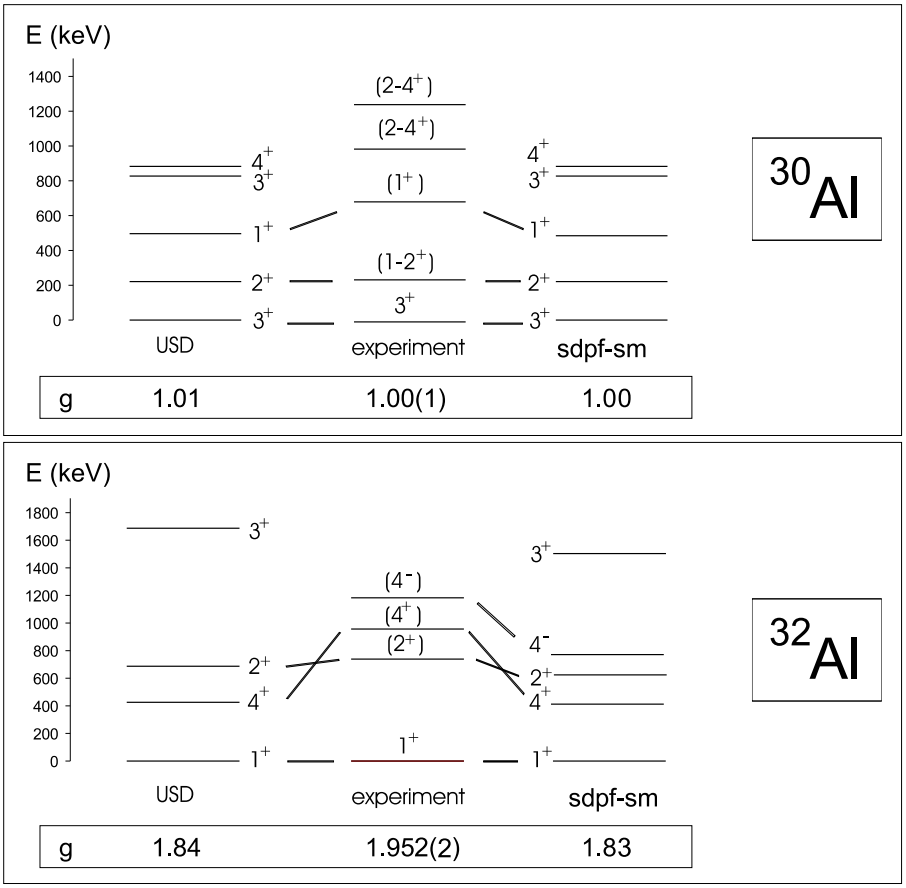

Figure 7.1: Comparison between theory and experiment of nuclear observables of $^{30-32}$Al. A maximum of 2 excitations from $\nu(d_{5/2}s_{1/2}d_{3/2})$ to $\nu(f_{7/2}p_{3/2})$ are allowed in the calculations.

The configurations of the odd-odd ^{32}Al nucleus with 1 neutron (proton) in the $s_{1/2}$ orbit can only couple to a spin 0, 1, 2 or 3 with the proton (neutron) in any sub-shell of the sd-shell. An increase of the amount of such configurations in the ground state and first 2^+ state of ^{32}Al, lowers the energy of the latter relative to the 4^+ state. This idea is confirmed by looking at the dependence of the excitation energies of the 2^+ and 4^+ state on the model space, as shown in Figure 7.2. In going from the restricted proton model space $\pi(d_{5/2})$ to the model space $\pi(d_{5/2}s_{1/2})$, the energy of the 4^+ state is increased by 375 keV. Notice that including the $\pi(d_{3/2})$ orbital hardly changes the excitation energies. This shows indeed that the $\pi(s_{1/2})$ orbital is important for the energy levels, while the g-factor depends crucially on the $\pi(d_{3/2})$ level.

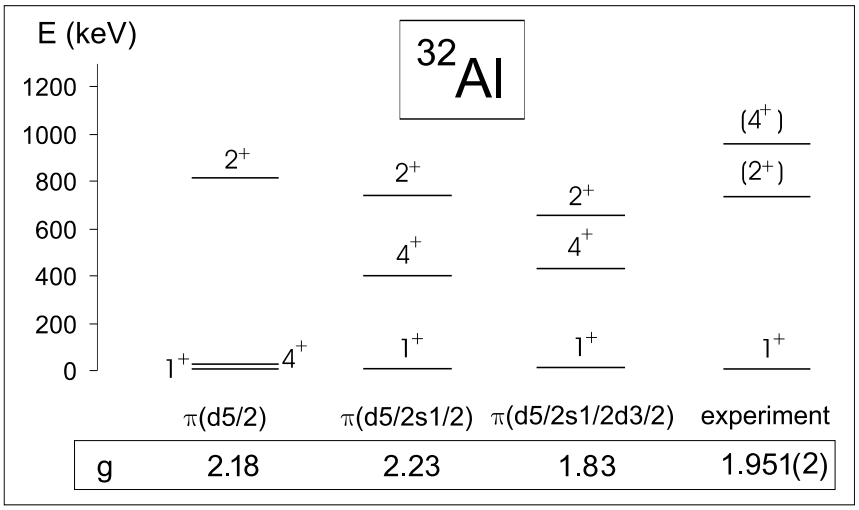

Figure 7.2: Level scheme and g-factor of ^{32}Al calculated with the sdpf-sm interaction in different model spaces for the protons, while the neutrons are restricted to the full sd-shell.

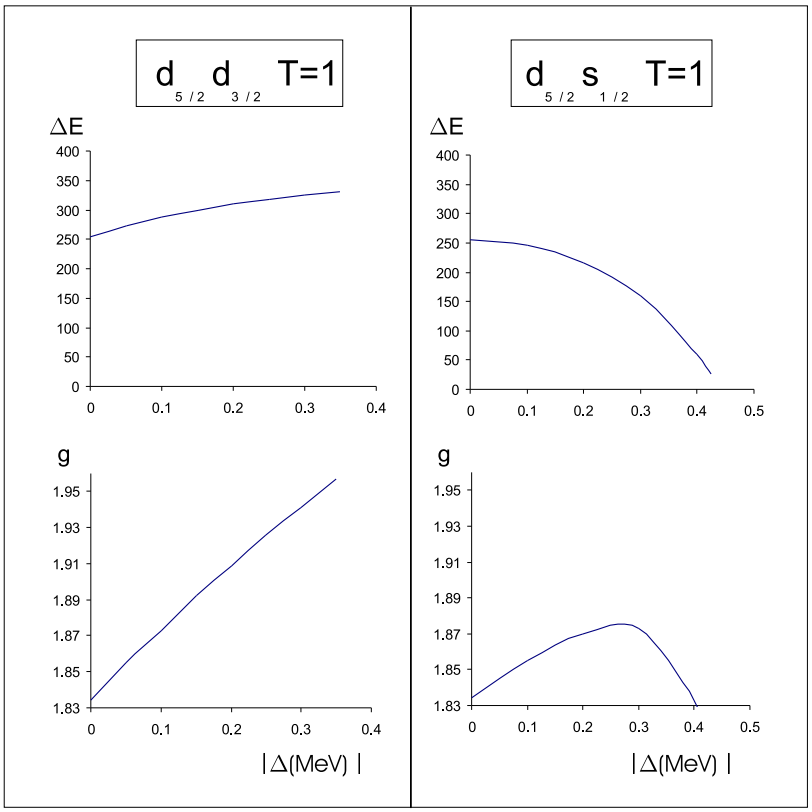

Figure 7.3: Effects of changing monopole terms ($|\Delta|$) on (top) difference in excitation energy (ΔE) of the 2^+ and 4^+ state, (bottom) on ground state g-factor of ^{32}Al.

These ideas can also be confirmed by changing the sdpf-sm interaction slightly. By increasing (=making the shells less attractive) the monopole term

$$\frac{\Sigma_J(2J+1) < d_{5/2}d_{3/2}|V_{d_{5/2}d_{3/2}}|d_{5/2}d_{3/2} >_{J,T=1}}{\Sigma_J(2J+1)} \tag{7.1}$$

with 0.32 MeV, the g-factor is reproduced exactly (see Figure 7.3). In this calculation, the ground state wave function has a 81.0% contribution of the $\pi(d_{5/2})\nu(d_{3/2})$ configuration, while the old code gave 78.5%. Notice that the energy of the first excited 2^+ and 4^+ state only changed 60 keV. Also by increasing the single particle energy of the $d_{3/2}$ orbital by 1.3 MeV, the g-factor can be reproduced.

On the other hand, by decreasing the monopole term

$$\frac{\Sigma_J(2J+1) < d_{5/2}s_{1/2}|V_{d_{5/2}s_{1/2}}|d_{5/2}s_{1/2} >_{J,T=1}}{\Sigma_J(2J+1)} \tag{7.2}$$

with 0.43 MeV, the 2^+ state becomes the first excited state and the 4^+ state the second. Notice that this change of the sdpf-sm interaction hardly changes the g-factor (see Figure 7.3). This switch is also predicted when lowering the single particle energy of the $s_{1/2}$ orbital by 2.0 MeV.

This indicates again that g-factor values and excitation energies depend both on specific parts of the nucleon-nucleon interaction and should both be taken into account when searching for new interactions.

7.2 ^{31}Al and ^{33}Al

Figure 7.4 shows the agreement between theory and experiment for the measured nuclear properties of ^{31}Al. Both the USD and sdpf-sm interaction give a quasi perfect prediction of the ground state g-factor and spins, parities and energies of the first excited states. The first pure 2p-2h intruder state is expected theoretically at 5.461 MeV and consequently does not influence the g-factor of the ground state.

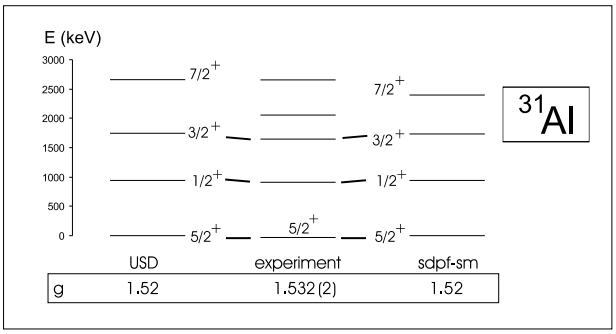

Figure 7.4: Comparison between theory and experiment of nuclear observables of ^{31}Al. In the sdpf-sm calculations, no excitations across N = 20 are allowed.

By adding two neutrons to this completely normal sd-nucleus, one obtains ^{33}Al, a semi-magic nucleus, according to the standard nuclear shell model (SNSM). Due to the magicity, the energies of levels with neutron excitations as a main component of the wave function are expected at high energy. Since the energy gap between the single particle energies of the $\pi(d_{5/2})$ and $\pi(s_{1/2})$ level is several MeV in the SNSM, the first excited proton states of ^{33}Al are expected at high energies as well.

Mittig et al. [71] state that they found an excited state at 730(50) keV in ^{33}Al. They suggest that this state can be the $\nu(2p-2h)$ intruder state, although no experimental evidence exists for that statement. If it were a $\nu(2p-2h)$ intruder, this state would mix with the ground state and change the nuclear properties of the latter. The β-decay of ^{33}Al, measured by Morton et al. [72], does not show such an influence, but this decay does not contradict to some small mixing either.

The USD interaction puts the first excited $1/2^+$ state at $\sim$ 3 MeV. This is an almost pure $\pi(s_{1/2})$ configuration. Also the sdpf-sm interaction restricted to the sd-shell predicts such a state at high energy (see Figure 7.5).

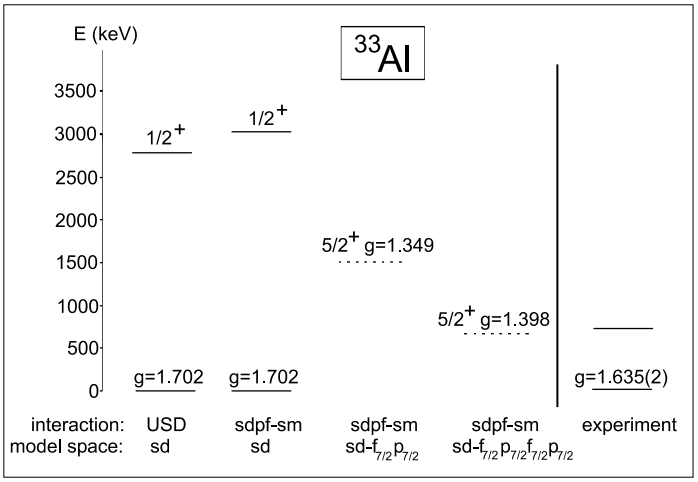

Figure 7.5: Comparison between theory and experiment of nuclear observables of ^{33}Al. The dotted line represents the pure 2p-2h state calculated with the sdpf-sm interaction.

The measured g-factor is significantly lower than the predicted value using the USD interaction or the sdpf-sm interaction without excitations across N = 20. The latter calculations show that the ground state is mainly (91.1%) a $\pi(d_{5/2})^{-1}$ configuration. Increasing this amount would higher the theoretical g-factor, since the Schmidt g-factor is 1.92 for this configuration, which would make the theory in less agreement with the experiment. On the other hand, a calculation with fixing one (or two) protons in the $s_{1/2}d_{3/2}$ sub-shells gives $g_{theory} = 2.59$ (or 1.91). This means that less $\pi(d_{5/2})^{-1}$ configuration (and thus more of the latter two configurations) also results in a higher theoretical g-factor. In conclusion, any change of the sdpf-sm interaction restricted to the sd-shells will not result in a satisfactory agreement between theory and experiment of the g-factor of the ground state of ^{33}Al.

In a second attempt of explaining the g-factor result, the neutron subshells above N = 20 are taken into account. The energy of the first pure 2p-2h neutron intruder level, relative to the pure 0p-0h state, was calculated using different model spaces using the sdpf-sm interaction, as shown in Figure 7.5.

Calculations, with the sdpf-sm interaction, in a restricted model space ($\nu(sd)$), give g(^{33}Al) = 1.702. The 2p-2h configuration with the same interaction results in 1.398 and is expected at 647 keV with respect to the 0p-0h state, using the full sd-pf valence space (see Figure 7.5). Intuitively, the real g-factor should be in between these extremes if the ground state wave function has some intruder components. This idea is confirmed by looking at the decrease ($1.702 \rightarrow 1.689 \rightarrow 1.680$) of the ground state g-factor when allowing more ($0 \rightarrow 2 \rightarrow 4$) neutron excitations, and thus having more intruder components in the ground state. These small amounts of intruder mixing are not enough to be in agreement with the experimental g-factor ($g_{exp} = 1.635(2)$). The intruder mixing would be larger if the pure 2p-2h configuration has a lower excitation energy. This indicates that the intruder states calculated with the sdpf-sm interaction using the full neutron valence space are expected too high and consequently not enough intruder mixing for the ground state of ^{33}Al is predicted.

The g-factor of the ground state of ^{33}Al can be predicted correctly by making the interaction between the $\pi(sd)$ shells and the $\nu(f_{7/2}p_{3/2})$ more attractive. This reduces the N = 20 shell gap. Decreasing the following monopole terms with 0.6 MeV

$$\frac{\Sigma_J(2J+1) < d_{5/2}f_{7/2}|V_{d_{5/2}f_{7/2}}|d_{5/2}f_{7/2} >_{J,T=0}}{\Sigma_J(2J+1)} \tag{7.3}$$

$$\frac{\Sigma_J(2J+1) < s_{1/2}f_{7/2}|V_{s_{1/2}f_{7/2}}|s_{1/2}f_{7/2} >_{J,T=0}}{\Sigma_J(2J+1)} \tag{7.4}$$

$$\frac{\Sigma_J(2J+1) < d_{3/2}f_{7/2}|V_{d_{3/2}f_{7/2}}|d_{3/2}f_{7/2} >_{J,T=0}}{\Sigma_J(2J+1)} \tag{7.5}$$

$$\frac{\Sigma_J(2J+1) < d_{5/2}p_{3/2}|V_{d_{5/2}p_{3/2}}|d_{5/2}p_{3/2} >_{J,T=0}}{\Sigma_J(2J+1)} \tag{7.6}$$

$$\frac{\Sigma_J(2J+1) < s_{1/2}p_{3/2}|V_{s_{1/2}p_{3/2}}|s_{1/2}p_{3/2} >_{J,T=0}}{\Sigma_J(2J+1)} \tag{7.7}$$

$$\frac{\Sigma_J(2J+1) < d_{3/2}p_{3/2}|V_{d_{3/2}p_{3/2}}|d_{3/2}p_{3/2} >_{J,T=0}}{\Sigma_J(2J+1)} \tag{7.8}$$

gives perfect agreement between experiment and the calculation, in which only 2 excitations are allowed from the sd-shells to the $f_{7/2}p_{3/2}$ shells. In these calculations ∼30% of the ground state wave function has 2p-2h intruder character, giving a clear indication that ^{33}Al lays on the border of the island of inversion.

To illustrate that the difference between experiment ($g_{exp} = 1.635(2)$) and the sd shell model calculation ($g_{theory} = 1.702$) is not negligible, the experimental and theoretical g-factors of other odd Al-isotopes are presented in Figure 7.6 (top). The difference for ^{33}Al is 4%, indicating that the intruder configurations influence the ground state.

In the Na (Z = 11) chain, the same trend is visible (Figure 7.6 bottom), but more pronounced. The measurement of the binding energy and the quadrupole moment proved that the ground state of ^{31}Na is an almost pure intruder configuration [38]. The experimental g-factor of ^{31}Na (1.537(5)), lowered due to intruder components, is in between the sd-value (1.77) and the intruder value (1.39). Calculations for ^{31}Na, allowing 2 (4) excitations from the sd orbits to the $p_{3/2}f_{7/2}$ orbits, predict a much higher g-factor 1.69 (1.62) than measured (1.537(5)), indicating that the amount of intruder mixing into the ground state derived with the sdpf-sm interaction is again not enough. Because the g-factor of ^{33}Al is pulled down less than in the case of ^{31}Na, the intruder part in the ground state of ^{33}Al is probably smaller than in ^{31}Na, but present.

In [108] and [109] calculations are performed with the MCSM method, using the SDPF-M interaction with the neutrons restricted to $sd - f_{7/2}p_{3/2}$. The experimental g-factor of ^{33}Al is slightly too low (1.55 versus g_{exp}=1.635(2)). The calculation gives a mixed ^{33}Al ground state with 50% intruder and 50% normal components. Since this theoretical value is too low, the real amount of intruder mixing is probably lower than 50%, but present.

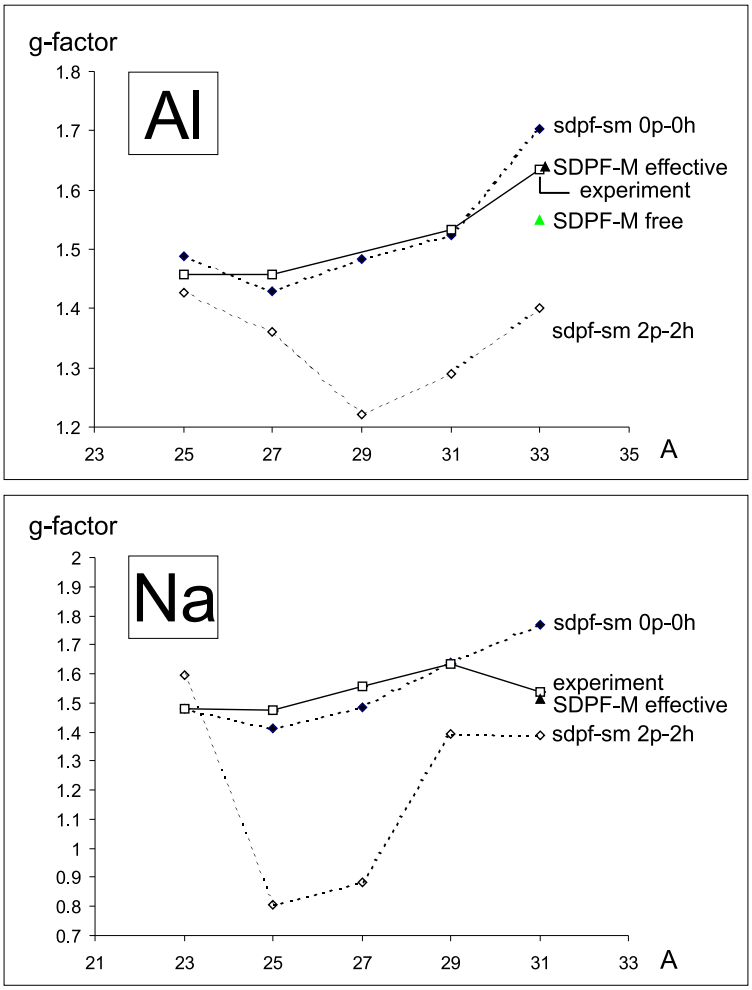

Figure 7.6: Comparison of experimental and theoretical g-factors of Al and Na-isotopes. The sdpf-sm interaction is used with no excitations across N = 20 (sdpf-sm 0p-0h) and with two neutrons fixed in $p_{3/2}f_{7/2}$ (sdpf-sm 2p-2h). The SDPF-M interaction is used to calculate free (SDPF-M free) and effective g-factors (SDPF-M effective).

Up to this point, the g-factor values referred to in this text are free nucleon g-factors. According to Brown [18] and Brandolini [85], experimental g-factors in this region of the nuclear chart (8 < N,Z < 32) are well reproduced without quenching the nucleon g-factors. Utsuno et al. [108] claim that for the SDPF-M interaction, effective g-factors give an overall better prediction of the g-factors in this region. The spin quenching is 0.90 and the correction to the isovector part of g_l is 0.15. Using these effective interactions, very good agreement for the g-factor of ^{33}Al and ^{31}Na is found. If the use of effective g-factors is considered reliable, the ground state wave function of ^{33}Al has 50% intruder components, according to the SDPF-M interaction, and that of ^{31}Na is an almost pure intruder state.

7.3 ^{34}Al

No evidence exists for neutron intruder components in the ground state of ^{34}Al so far. From the β-decay of ^{34}Al and the measurement of B(E2) from the first excited state to the ground state [75], the ground state spin and parity of ^{34}Al are proposed as 4^- [73] [74].

The g-factor does not pin down the spin since the first excited state, with spin 5 and expected at very low energy, has a theoretical g-factor which is very close to the g-factor of the 4^- state, as shown in Figure 7.7. From the g-factor measurement it can be concluded that the 1p-1h 4^+ state is not the ground state, since a g-factor of 1.23 is expected in that case.

Figure 7.8 shows the g-factor result of ^{34}Al together with the other odd proton odd neutron Al isotopes. A clear deviation of 32% from the normal configuration is observed. Since the coupling of $\pi(d_{5/2})\nu(f_{7/2})$, $\pi(s_{1/2})\nu(f_{7/2})$, $\pi(d_{3/2})\nu(f_{7/2})$ to a 4^- state gives a g-factor equal to 0.25, 0.22 and 0.35 respectively, this deviation can not be explained by changing the $\pi(d_{5/2})\nu(f_{7/2})$, $\pi(s_{1/2})\nu(f_{7/2})$ or $\pi(d_{3/2})\nu(f_{7/2})$ monopole. Concerning the $\nu(p_{3/2})$ level, only the monopole term $\pi(d_{5/2})\nu(p_{3/2})$ can influence the ground state g-factor, since a $d_{3/2}$ or $s_{1/2}$ proton can not couple to a 4^- state with a $p_{3/2}$ neutron.

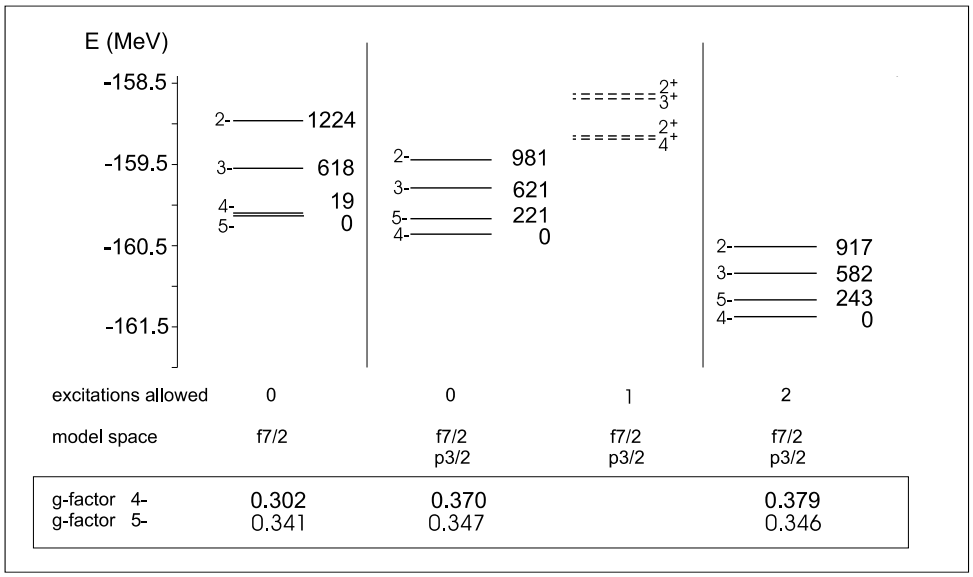

Figure 7.7: Theoretical level scheme of ^{34}Al, using different model spaces and numbers of allowed excitations. The dotted lines represent the 1p-1h states. g_{exp}=0.541(1)

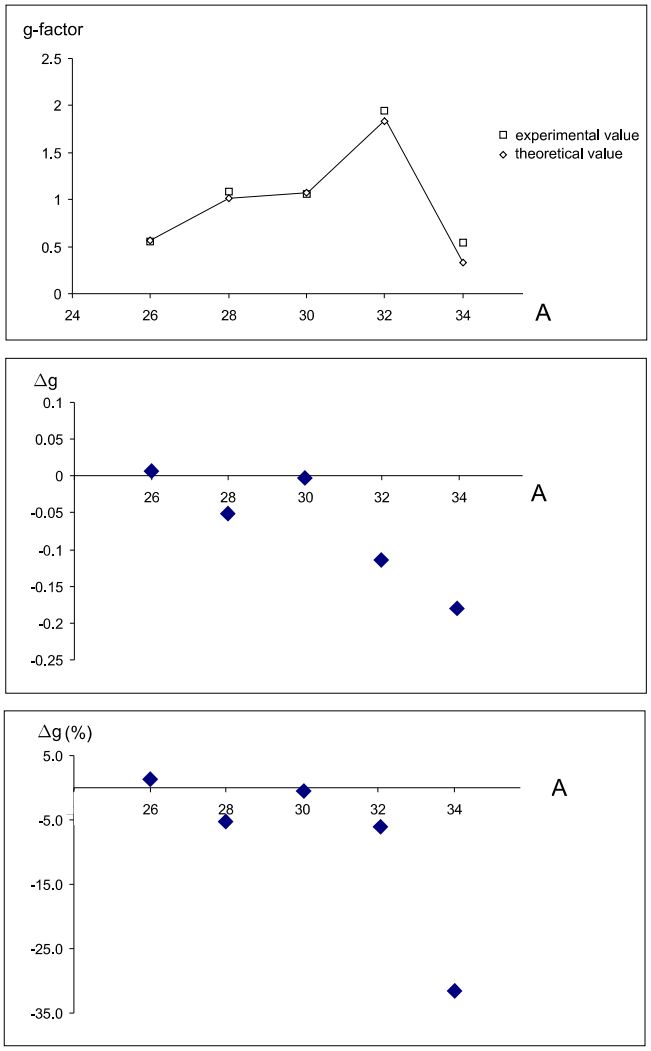

Figure 7.8: (top) Experimental and theoretical g-factors of even Al isotopes, using sdpf-sm interaction in the $\nu(sd - f_{7/2}p_{3/2})$model space and no neutron excitations allowed - (middle) Absolute difference of experimental and theoretical g-factors - (bottom) Relative difference of experimental and theoretical g-factors. In both figures I(^{34}Al) is taken as 4^-.

Such a pure $\pi(d_{5/2})\nu(p_{3/2})$ configuration has a g-factor equal to 0.72, while g($\pi(d_{5/2})\nu(f_{7/2})$)=0.25. Taking into account the $\nu(p_{3/2})$ level increases the theoretical g-factor from 0.302 to 0.370, as shown in Figure 7.7. Increasing the amount of $p_{3/2}$ mixing would result in a theoretical g-factor value closer to the experimental value (0.541(1)).

If this is the correct reason for the slight difference between theory and experiment, it means that the monopole interaction term between $\nu(p_{3/2})$ and $\pi(d_{5/2})$ is not correct. Similar to the change in the interaction from sdpf to sdpf-sm (in which the $\nu(p_{3/2})$-$\pi(d_{3/2})$ and $\nu(p_{3/2})$-$\pi(s_{1/2})$ monopole interaction terms are changed slightly in order to reproduce the $3/2^-$ excitation energy in ^{35}Si, while still reproducing the excitation energy for the other N=21 nuclei: ^{41}Ca, ^{39}Ar and ^{37}S), the monopole term $\nu(p_{3/2})$-$\pi(d_{5/2})$ in the sdpf-sm interaction can be changed to reproduce the g-factor of ^{34}Al and still having perfect agreement between the theoretical and experimental excitation energy of the first $3/2^-$ state in ^{35}Si.

Notice that the ordering of the effective single particle energy of $\nu(f_{7/2})$ and $\nu(p_{3/2})$ for N = 20 nuclei in the SDPF-M interaction is different (see Figure 2.7). This indicates that a calculation with this interaction would result in a wave function with a higher $\nu(p_{3/2})$ component, giving a g-factor closer to the experiment. Remark that it is not known whether this interaction reproduces the spectrum of ^{35}Si as good as the sdpf-sm interaction.

A second way of explaining the observed g-factor is the following. Fixing three neutrons in the $\nu(f_{7/2}p_{3/2})$ shells, results in g = 0.67. The experimental value is higher than the g-factor value for the normal configuration, but smaller than this pure intruder value. This indicates that a mixed ground state could explain the measured g factor result. Allowing 2p-2h intruder states, the theoretical g-factor changes slightly from 0.370 to 0.379, which is not enough to change the theoretical g-factor result to be in agreement with the experimental g-factor. This small g-factor change is due to the fact that the pure 2p-2h configuration is expected at rather high excitation energy as shown in Table 7.1.

Table 7.1: Energy difference between pure 0p-0h and 2p-2h 4^- ground state of ^{34}Al and g-factor of pure 2p-2h state for different valence spaces.

valence space	energy difference (keV)	g-factor
$sd - f_{7/2}p_{3/2}$	2723	0.67
$sd - f_{7/2}p_{3/2}f_{5/2}p_{1/2}$	1544	0.69

If this is the correct reason for the slight difference between theory and experiment, it means that the amount of intruder mixing for ^{34}Al is underestimated by the sdpf-sm interaction and a non negligible amount of intruder components is present in the ground state of ^{34}Al, which proves that the magicity of N = 20 is lost for ^{34}Al. This idea is confirmed by changing the sdpf-sm interaction slightly. The same monopole terms as for the explanation of the g-factor of ^{33}Al (see equations (7.3)-(7.8))have to be changed by -1.3 MeV to get the same theoretical g-factor as the measured value, while it was -0.6 MeV for ^{33}Al.

7.4 ^{35}Si

It was pointed out in the first chapter that $^{35}_{14}$Si is a very interesting nucleus from the point of view of shell model calculations. In its ground state, ^{35}Si has a full $\pi(d_{5/2})$ subshell and one neutron outside the sd-shell.

The first excited $3/2^-$ state (at 910 keV) gives information on the single particle energies of the $\nu(f_{7/2})$ and $\nu(p_{3/2})$ orbital and on the difference of the monopole interaction between $\nu(p_{3/2})$ and $\pi(d_{5/2}, s_{1/2}, d_{3/2})$ and between $\nu(f_{7/2})$ and $\pi(d_{5/2}, s_{1/2}, d_{3/2})$ (see Figure 3.17).

The $3/2^+$ state (at 974 keV) gives an indication of the N = 20 shell gap for ^{35}Si, since it is an odd particle - odd hole intruder state.

Once the energies of these excited states were measured [24] and spin assignments were proposed from the β-decay of ^{35}Al and from lifetime measurements of certain excited states in ^{35}Si, the sdpf interaction was changed to fit the observed energies. This more recent interaction is called sdpf-sm (see Figure 3.17).

In the previous interaction (sdpf), the energy of the $3/2^-$ was expected at 2 MeV, while experimentally it is observed at 910 keV. The sdpf-sm interaction puts it at 952 keV, when omitting excitations across N = 20 and using the full pf model space for the neutrons. The observed low laying $3/2^-$ single-particle state can be interpreted as a reduction of the neutron gap between the $f_{7/2}$ and $p_{3/2}$ shells for ^{35}Si (see Figure 2.7). This reduction can be explained by a decrease of the spin-orbit term, responsible for the energy difference between $f_{7/2}$ and $f_{5/2}$. A weaker spin orbit term brings the $f_{7/2}$ level closer to the $p_{3/2}$ level, which is situated in between $f_{7/2}$ and $f_{5/2}$. Such a higher $f_{7/2}$ level is an enhancement of the magicity of N = 20 for ^{35}Si.

The energy of the $3/2^+$ level was calculated allowing 1 neutron excitation in the full ν(sd-pf) space. The level is predicted at 959 keV above the pure 0p-0h ground state, which is in perfect agreement with the experimental value (974keV).

At the time the sdpf-sm interaction was introduced, it was believed that the restriction of the protons to the sd-shell did not play a crucial role. Later it was noticed by Caurier et al. [110] that excitations across the Z = 20 subshell are needed to explain the isotope shift in the $^{41-47}_{20}$Ca isotopes, and the 2^+ and 3^- excitation energies in $^{40,42,44,46,48}_{20}$Ca. It is mentioned that approximately equal numbers of protons and neutrons are lifted from the sd shell. It is therefore difficult to identify a simple cause, or a definite component of the Hamiltonian, as the driving force of this effect. Including the $\pi(f_{7/2}p_{3/2})$ and $\nu(f_{7/2}p_{3/2})$ shells, the calculations show that for ^{40}Ca an average of 1.10 nucleons are excited to the fp-shells [110].

By decreasing the number of protons in the sd-shell ($Z = 20 \rightarrow Z = 14$), the probability of excitations of protons to the pf shells decreases. We thus expect the nuclear properties of $^{35}_{14}Si_{21}$ to be in better agreement with the ANTOINE calculations than ^{41}Ca, when using the sdpf-sm interaction with a restriction of the protons to the sd part. This is seen in the comparison of the g-factors of the N = 21 isotones in Figure 7.9. Notice that the NMR-method used in this thesis work to obtain the g-factor of ^{35}Si, only gives the absolute value and not the sign. Since the ground state wavefunction is dominated by the $\nu(f_{7/2})$ configuration, with -0.547 as Schmidt g-factor, the sign is proposed to be negative.

Assuming N = 20 and Z = 20 is a magic number, the g-factor of ^{41}Ca should approach the Schmidt g-factor (-0.547). Going away from the shell closure ($Z = 20 \rightarrow Z = 14$), the absolute value of the g-factor decreases, as is shown by the theoretical calculations, not taking into account the fp shells for the protons and forbidding excitations across N = 20. The fact that the g-factor of ^{41}Ca is much lower than this theoretical value is most probably due to proton and/or neutron intruder configurations, because the experimental value (0.466(6)) is in between the normal configuration and a pure 2p2h configuration (pure 2p-2h neutron state: g(^{41}Ca)= -0.43 - pure 2p-2h proton state g(^{41}Ca)= -0.16). Allowing 2 neutron excitations to the $\nu(f_{7/2}p_{3/2})$ sub-shell and 2 proton excitations to $\pi(f_{7/2}p_{3/2})$ gives -0.527, which is indeed closer to the experimental value. Notice that indeed both proton and neutron excitations have to be taken into account, since the g-factor only decreases by 0.0004 (0.0009) when only allowing neutrons (protons), to be excited. When both excitations are allowed, the g-factor is pulled down by 0.0187 due to the $\pi((sd)^{-2}(pf)^2)\nu((sd)^{-2}(pf)^3)$ component.

Also the g-factor of ^{39}Ar is slightly lower than expected (g_{theory}=-0.492 and g_{exp}=-0.454(4)) [111]. For ^{38}Ar and ^{40}Ar, it was already noticed that excitations across the N = 20 and Z = 20 shell gap should be taken into account [112] [110]. This indicates that the slightly different theoretical and experimental value for ^{39}Ar can be due to the restriction of the used model space. Allowing 2 neutron excitations to the $\nu(f_{7/2}p_{3/2})$ sub-shell and 2 proton excitations to $\pi(f_{7/2})$ gives -0.488, which is indeed slightly closer to the experimental value.

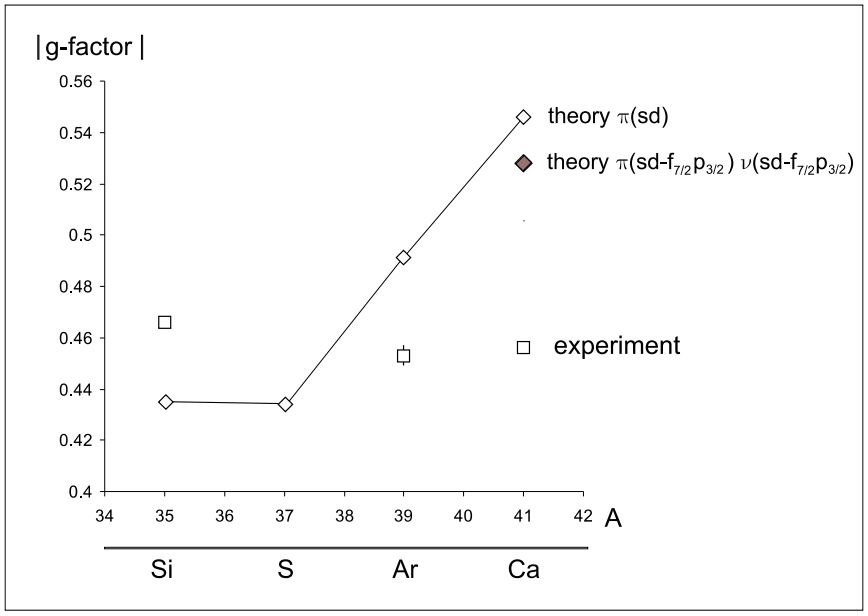

Figure 7.9: Comparison of experimental and theoretical g-factors of N = 21 isotones using the sdpf-sm interaction. 'Theory π(sd)' refers to calculations with the sdpf-sm interaction in which the protons are restricted to the sd-shell and no excitations across N = 20 are allowed. 'Theory π(sd-$f_{7/2}p_{3/2}$)ν(sd-$f_{7/2}p_{3/2}$)' refers to calculations in which the protons are restricted to the sd-$f_{7/2}p_{3/2}$ shells with a maximum of two protons in $f_{7/2}p_{3/2}$ and the neutrons are restricted to the sd-$f_{7/2}p_{3/2}$ shells with a maximum of three neutrons in $f_{7/2}p_{3/2}$.

The small difference between $g_{theory}(^{35}\mathrm{Si})$ and experiment can not be explained by 2p-2h proton or neutron excitations since these would bring the g-factor closer to 0 (pure 2p-2h neutron state: g(^{35}Si)= -0.37 - pure 2p-2h proton state g(^{35}Si)= 0.01). Prohibiting protons in the $\pi(d_{3/2})$ shell changes the theoretical g factor from -0.43 to -0.53, while it stays constant when also the $\pi(s_{1/2})$ level is prohibited. This could indicate that the sdpf-sm interaction underestimates the $\pi(d_{5/2})\nu(f_{7/2})$ component, which means that ^{35}Si has an even larger energy splitting between $\pi(d_{5/2})$ and $\pi(s_{1/2}d_{3/2})$, enhancing the semi-magicity of Si.

7.5 Conclusion

For ^{30}Al and ^{31}Al both the USD interaction and the sdpf-sm interaction give good agreement with the observed nuclear properties. For neither of both isotopes excitations across N = 20 are needed to explain the g-factor. Both nuclei do not belong to 'the island of inversion'.

For ^{32}Al the small deviation between the experimental g-factor and the prediction from the sdpf-sm interaction can not be explained by 2p-2h intruder mixing into the ground state. This difference and the anomaly in explaining the low energy level scheme, could be solved by changing the sd-part of the sdpf-sm interaction slightly. Since the g-factor of ^{32}Al is very sensitive to the energy of the $\pi(d_{3/2})$ level, while the excitation energy of the first 2^+ and 4^+ is more dependent on the $\pi(s_{1/2})$ level, the importance of g-factor measurements for deriving shell model interactions is demonstrated.

By measuring the g-factor, an indication is found, for the first time, that a small, but non negligible portion of the ground state wave function of ^{33}Al is of even particle - even hole intruder nature. The SDPF-M interaction (using free nucleon g-factors) overestimates the intruder components, while the sdpf-sm interaction predicts too few intruder mixing into the ground state. By changing the sdpf-sm interaction until the g-factor is reproduced exactly, the ground state of ^{33}Al is found to consist of $\sim$30% of intruder components.

A large amount of mixing of even particle - even hole neutron intruder states into the ground state of ^{34}Al, is probably the explanation of the measured g-factor result. This result shows, for the first time, that Z = 13 is a true transition number from spherical nuclei (Z=14) to intruder dominated nuclei (Z=12). This transition is thus smoothly and not abrupt.

The physical interpretation of the g-factor results from ^{32}Al, ^{33}Al and ^{34}Al are put in Figure 7.10, showing a gradual transition from nuclei with normal to nuclei with intruder dominated ground states at Z=13.

The experimental g-factor of ^{35}Si is in good agreement with the theoretical value obtained with the sdpf-sm interaction, although better agreement could be obtained by an increase of the $\pi(d_{5/2})\nu(f_{7/2})$ configuration in the ground state of ^{35}Si.

As a general conclusion from these g-factor measurements, we can state that g-factor values give crucial information on certain parts of the residual interaction. In order to derive reliable shell model interactions, it is thus not enough to take into account only the excitation energies when fitting the interaction to experimental data, but also g-factor results should be taken into account.

Z = 14	Si	30	31	32	33	34	35	
Z = 13	Al	29	30	31	32	33	34	
Z = 12	Mg	28	29	30	31	32	33	34
Z = 11	Na	27	28	29	30	31	32	
Z = 10	Ne		27	28	29	30		
Z = 9	F			27		29		
N =		16	17	18	19	20	21	22

Figure 7.10: Part of the nuclear chart around the island of inversion. Nuclear properties of the ground state of nuclei in light (dark) grey can (not) be explained without intruders. The white nuclei are undetermined. A gradual transition from light to dark grey reflects the smooth border of the island of inversion at Z=13.

Chapter 8

Conclusion and outlook

8.1 Conclusion

The main goal of this thesis work is the measurement and interpretation of ground state g-factors of nuclei around the 'island of inversion'. In order to perform NMR measurements, the selected beam needs to be polarised. The amount of polarisation that is destroyed resonantly in the NMR measurements, determines the amplitude of the NMR effect. Since this amplitude and the production rate determines the time to measure the g-factor of a nucleus, a large part of this work was devoted to the aspect of polarisation.

8.1.1 Polarisation: creation

In a first step, the amount of polarisation is investigated for both reaction types (projectile fragmentation and pick-up followed by evaporation of a few nuclei) used to produce the nuclei of interest. It is shown that a simple 'polarisation test', in which the amount of produced polarisation is derived from the asymmetry difference between a low and a high static magnetic field can give an indication on the presence of polarisation, but is not necessarily giving the absolute amount correctly. Instead, the NMR curve should be fit with the correct gaussian line-broadening and RF power to deduce the polarisation that was produced.

The polarisation trend as function of the selected momentum distribution was measured for nuclei produced via fragmentation (^{36}S+^{9}Be $\rightarrow^{32}$Al) and pick up (^{36}S+^{9}Be $\rightarrow^{34}$Al,^{35}Si). These data are in very good agreement with the results from the kinematical code, assuming 'the participant-spectator' model. It is observed that polarisation is maximal at the center of the momentum distribution in case of the pick-up reaction. This is in contrast to the projectile fragmentation reaction, in which the fragments should be selected in the wing of the momentum distribution, to obtain the highest amount of polarisation. The amount of polarisation in both reaction types is similar, or even slightly higher in the pick up case. This shows that the pick-up reaction mechanism (which can be followed by evaporation) is a very good tool to produce nuclei of which the g-factor will be measured via NMR.

A measurement of the polarisation of ^{33}Al produced via a ^{36}S beam on a ^{9}Be target and later by a ^{36}S beam on a ^{184}W target confirmed the inversion of the sign of polarisation when going from near-side to far side reactions, as predicted by the kinematical model.

8.1.2 Polarisation: maintaining

By trying several implantation crystals, Si seemed to be a good host to keep the polarisation. Since the decoupling curve in this crystal saturated around 0.08 T, it was decided to do NMR measurements above this static magnetic field value.

As a last tool to optimize the polarisation, it was verified that fragments observed in the LISE 2000 beam line give significantly less orientation then the ones from LISE. The main reason is the fact that with LISE 2000 a less pure beam is obtained ($\sim$50% compared to >95% in LISE).

8.1.3 Polarisation: destruction

A code, based on the numerical derivation of the Schrodinger equation using the NMR Hamiltonian, was developed to give more insight in finding the optimum conditions to destroy as much polarisation as possible.

The amplitude of the NMR resonance is mainly determined by five factors: lifetime of the observed nucleus, RF strength, inhomogeneous line-broadening, modulation amplitude and modulation frequency. If the lifetime is longer than 1 ms and the RF power around 1 gauss, these parameters hardly influence the amplitude. The modulation frequency should be faster than the life time of the nucleus, but considerably longer than the Rabi oscillations. As long as the inhomogeneous line-broadening is appreciably smaller than the NMR width due to the combination of the RF strength and frequency modulation amplitude, the NMR amplitude is maximal.

The NMR technique can be applied by varying the static magnetic field (B_0) or the applied frequency (ν_{RF}). With the current set-up, the second method can only be used when scanning a small g-factor region. The first method has the disadvantage that half of the measuring time is used for normalisation purposes, while this can be up to a factor 10 less in case of frequency scanning.

8.1.4 g-factor measurements

Knowing the optimal conditions for all parameters involved, successful NMR measurements were performed on five different exotic nuclei. The precision of each measurement is determined both by the statistical error, and the systematic error , with the last dominating, due to the inhomogeneity of the magnetic field over the large beam spot in combination with calibration uncertainties. By measuring the g-factor of ^{32}Al several times in the same run, the statistical error seemed appropriate. The systematic error of 0.11% is deduced by comparing the results of different runs.

The five g-factors are compared with large scale shell model calculations using different interactions. Following conclusions were drawn on each nucleus:

- For ^{30}Al and ^{31}Al both the USD interaction and the sdpf-sm interaction, restricted to the sd shells, give good agreement with the g-factor and other observed nuclear properties. Both nuclei do not belong to 'the island of inversion'.

- For ^{32}Al the small deviation between the experimental g-factor and the prediction from the sdpf-sm interaction can not be explained by 2p-2h intruder mixing into the ground state. This difference and the anomaly in explaining the low energy level scheme, could be solved by changing the sd-part of the sdpf-sm interaction slightly. Since the g-factor of ^{32}Al is very sensitive to the energy of the $\pi(d_{3/2})$ level, while the excitation energy of the first 2^+ and 4^+ is more dependent on the $\pi(s_{1/2})$ level, the importance of g-factor measurements for deriving reliable shell model interactions is demonstrated.

- By measuring the g-factor, it was shown, for the first time, that a small, but non negligible portion of the ground state wave function of ^{33}Al has even particle - even hole intruder character. The SDPF-M interaction (with free nucleon g-factors) overestimates the intruder components, while the sdpf-sm interaction predicts too few intruder mixing into the ground state.

- A large amount of mixing of even particle - even hole neutron intruder states into the ground state of ^{34}Al, is probably the explanation of the measured g-factor result. This result shows, for the first time, that Z = 13 is a true transition number from spherical nuclei (Z=14) to intruder dominated nuclei (Z=12). This transition is thus smoothly and not abrupt.

- The experimental g-factor of ^{35}Si is in good agreement with the theoretical value obtained with the sdpf-sm interaction, although better agreement could be obtained by an increase of the $\pi(d_{5/2})\nu(f_{7/2})$ configuration in the ground state of ^{35}Si.

As a general conclusion of this work, we can state that we do understand in detail the principles of making a polarised beam via projectile-fragmentation and pick-up. The NMR measurements can now be done in an efficient way, both scanning as function of field and frequency. The obtained g-factor results give crucial information on certain parts of the residual interaction and show evidence for a smooth border of the island of inversion as function of Z instead of an abrupt transition from spherical to deformed nuclei. In order to derive reliable shell model interactions, it is thus not enough to take into account only the excitation energies when fitting the interaction to experimental data, but also g-factor results should be taken into account.

8.2 Outlook

Concerning the kinematical model, no drastic deviations from experimental results were observed. A slight dependence of polarisation on the spin of the formed fragment is noticed, although not enough statistics is taken to be conclusive. Since the kinematical model does not take into account the spin, it can not reproduce this trend. In order to draw firm conclusions on the spin-dependence, more NMR measurements should be performed on well produced nuclei, preferable with low Q_β of the daughter nuclei.

Around the 'island of inversion', still several nuclei are interesting to be studied by NMR. The g-factor of the ground state of ^{33}Mg and ^{33}Na or even more exotic nuclei, would give much extra information for theoreticians to retune the interactions used in shell model calculations. Also g-factor measurements of isomeric states, such as the third excited state in ^{32}Al, which could be a 1p-1h intruder state, is needed to pin down the N = 20 shell gap dependence on N and Z.

Apart from the dipole moment, the quadrupole moment is another nuclear observable that is crucial in determining the amount of intruder mixing into certain levels of nuclei around the island of inversion. Since this property is very dependent on the collectivity of the state, it is the

perfect tool to get an extra indication of the intruder components in the ground state of ^{33}Al. The quadrupole moment of ^{34}Al could tell us without any doubt whether the extra $p_{3/2}$ component or the even particle - even hole intruder component is the reason for the deviating experimental g-factor, since the sign of the quadrupole moment of an intruder state is different from a normal spherical state.

Table 8.1: Expected position of LMR resonance of ^{32}Al in different implantation crystals. ANTOINE calculations using the sdpf-sm interaction with different e_p (1.0-1.5)) and e_n (0.5-1.0) results in Q_{theory}=2.5(3)efm^2. $^{(a)}$ calculated values [114] - $^{(b)}$ measured value [115] [116]

	V_{zz} (10^{21}V/m^2)	resonance expected at (gauss)
Al(Al_2O_3)	0.57 $^{(a)}$	150-210
	0.71(1) $^{(b)}$	190-250
Al(Cd)	2.11 $^{(a)}$	560-740
Al(Mg)	0.26 $^{(a)}$	70-90
Al(SiO_2)	0.90 $^{(a)}$	250-320
Al(Zn)	2.47 $^{(a)}$	670-870

Several attempts were made to deduce the quadrupole moment of ^{32}Al via the Level Mixing Resonance (LMR) technique [113] as well as the multiple Nuclear Quadrupole Resonance (NQR) technique [41]. Some of these results together with the positions of the expected LMR resonance are shown in Figure 8.1 and Table 8.1. All attempts failed due to poor crystal qualities. Several Cd, Mg, Al_2O_3 and SiO_2 crystals were tried as implantation host, but no resonance was observed. In SiO_2 and Al_2O_3 a decoupling curve is observed, indicating that those crystals could be appropriate when used at high magnetic fields.

With the LMR technique, the position of the resonance in the field spectrum is fixed by the electric field gradient felt by the implanted nucleus in the host crystal. Using the multiple NQR technique, the resonance is scanned by varying the frequency, which gives some freedom to choose the applied static magnetic field. Using a different magnet that can generate higher fields, could be the tool to measure the quadrupole moment of ^{32}Al, followed by the other isotopes.

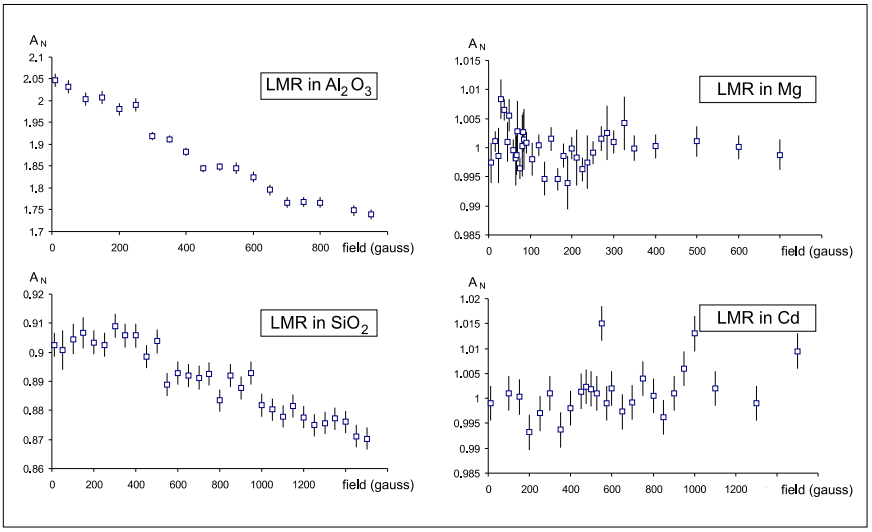

Figure 8.1: Experimental results of LMR experiments on ^{32}Al to deduce the quadrupole moment. A resonance around 200, 285, 80, 650 gauss is expected for the Al_2O_3, SiO_2, Mg and Cd crystal respectively.

Bibliography

[1] Kenneth S.Krane, *Introductary Nuclear Physics*, (John Wiley and Sons, USA, 1988).

[2] Richard F. Casten, *Nuclear Structure from a Simple Perspective*, (Oxford Science Publications, England, 2000).

[3] J.Bron *et al.*, Nucl. Phys. A **318**, 3 335-351 (1979).

[4] P. Van Duppen *et al.*, Phys. Rev. Lett. **52**, 1974 (1984).

[5] P. Van Duppen *et al.*, Phys. Lett. **154B**, 354 (1985).

[6] E. Coenen *et al.*, Phys. Rev. Lett. **54**, 1783 (1985).

[7] C. Thibault *et al.*, Phys. Rev. C. **12**, 644 (1975).

[8] C. Detraz *et al.*, Nucl. Phys. A. **394**, 378 (1983).

[9] C. Detraz *et al.*, Phys. Rev. C. **19**, 164 (1979).

[10] K. Heyde *et al.*, J. Phys. G: Nucl. Part. Phys. **17**,135-143 (1991).

[11] D. Guillemaud *et al.*, Nucl. Phys. A. **436**, 37 (1984).

[12] A. Gillibert *et al.*, Phys. Lett. A. **192B**, 39.

[13] A.J. Wapstra *et al.*, At. Data Nucl. Data Tables **39**, 281.

[14] Y. Utsuno *et al.*, Phys. Rev. C. **70**, 044307.

[15] Kuo *et al.*, Ann. Rev. Nucl. Sci. **24**, 101 (1974).

[16] J. Shurpin *et al.*, Nucl. Phys. A. **408**, 310 (1983).

[17] J.B. McGrory *et al.*, Ann. Rev. Nucl. Sci. **30**, 383 (1980).

[18] B.H. Wildenthal *et al.*, Prog. Part. Nucl. Phys. **11**, 5 (1984).

[19] Warburton *et al.*, Phys. Rev. C. **41**, 1147-1166 (1990).

[20] E. Caurier *et al.*, Phys. Rev. C **58**, 2033 (1998).

[21] J. Retamosa *et al.*, Phys. Rev. C **5**, 1266 (1997).

[22] T. Otsuka *et al.*, Prog. Part. Nucl. Phys. **47**, 319 (2001).

[23] Y. Utsuno *et al.*, Phys. Rev. C **64**, 011301 (2001).

[24] S. Nummela *et al.*, Phys. Rev. C **63**, 044316 (2001).

[25] M. Honma *et al.*, Phys. Rev. C **69**, 034335 (2004).

[26] M. Dufour, A.P. Zucker *et al.*, Phys. Rev. C. **54**, 1641 (1996).

[27] E. Caurier *et al.*, Eur.Phys. J. A **15**, 145-150 (2002).

[28] O.Tarasov *et al.*, Phys. Lett. B **409**, 1-4 64-70 (1997).

[29] D.Bazin and O.Sorlin, computer code LISE, www.nscl.msu.edu/bazin/LISE.html

[30] http://wwwndc.tokai.jaeri.go.jp/nds/proceedings/2000/o03.pdf

[31] E. Khan *et al.*, Phys. Rev. C **66**, 024309 (2002).

[32] B.V. Pritychenko *et al.*, Phys. Lett. B **461**, 322-328 (1999).

[33] Y. Utsuno *et al.*, Nucl. Phys. A. **704**, 50-59 (2002).

[34] U.C. Bergman *et al.*, EPJ **11**, number 3, 279-284 (2001).

[35] Y. Yanagisawa *et al.*, Phys. Lett. B **566**, 84-89 (2003).

[36] N.A. Orr *et al.*, Phys. Lett. B **258**, number 1, 29 (1991).

[37] Y.Utsuno *et al.*, Progress of Theor. Phys. Suppl. **146**, 488 (2002).

[38] M. Keim *et al.*, Hyp. Int. **97/98**, 543-550 (1995).

[39] M. Keim *et al.*, EPJ **8**, 31-40 (2002).

[40] N.A. Orr *et al.*, Phys. Letters B **258**, 29 (1991).

[41] G. Neyens *et al.*, Reports on Progress in physics **66**, number 4, 633 (2003).

[42] G. Hubert *et al.*, Phys. Rev. C **18**, 2342 (1978).

[43] B.V. Pritychenko *et al.*, Phys. Rev. C **66**, 024325 (2002).

[44] V. Tripathi *et al.*, Phys. Rev. Letters **94**, 162501 (2005).

[45] Y. Utsuno *et al.*, Phys. Rev. C **60**, 054315 (1999).
024325 (2002).

[46] B.V. Pritychenko *et al.*, Phys. Rev. C **63**, 011305 (2000).

[47] T. Suzuki *et al.*, Phys. Rev. Lett. **75**, number 18, 3241 (1995).

[48] Z. Radivojevic *et al.*, Nucl. Instrum. Methods Phys. Res. A (to be published)

[49] S. Nummela *et al.*, Phys. Rev. C **64**, 054313 (2001).

[50] D. Yordanov et al., Ph.D. thesis and paper in preparation.

[51] V. Chiste *et al.*, Phys. Lett. B **514**, 233-239 (2001).

[52] B.V. Pritychenko *et al.*, Phys. Lett. B **461**, 322 (1999).

[53] O. Niedermaier *et al.*, Phys. Rev. Lett. **94**, 172501 (2005).

[54] Y. Utsuno *et al.*, Nucl. Phys. A **704**, 50-59c (2002).

[55] H. Mach *et al.*, EPJ A **25**, 105-109 (2005)

[56] G. Klotz *et al.*, Phys. Rev. C **47**,6 2502 (1993).

[57] G. Neyens *et al.*, Phys. Rev. Lett. **94**, 022501 (2005).

[58] F. Marechal *et al.*, in progress

[59] T. Motobayashi *et al.*, Phys. Lett. B **346**, 9 (1995).

[60] W. Mittig *et al.*, Prog. Theor. Phys. Suppl. **146**, 16 (2002).

[61] M. Belleguic *et al.*, Nucl. Phys. A **682**, 136-142c (2001).

[62] B.V. Pritychenko *et al.*, Phys. Rev. C **65**, 061304 (2002).

[63] T. Motobayashi *et al.*, Eur. Phys. Journal **15**, 99-103 (2002).

[64] H. Iwasaki *et al.*, Phys. Lett. B **522**, 227-232 (2001).

[65] H. Sakurai *et al.*, Prog. Theor. Phys. Suppl. **146**, 39-48 (2002).

[66] D. Borremans *et al.*, Phys. Lett. B **537**, 45-50 (2002).

[67] F. Marechal *et al.*, Phys. Rev. C **72**, 044314 (2005).

[68] M. Robinson *et al.*, Phys. Rev. C. **53**, part 4, 53 (1996).

[69] B. Fornal *et al.*, Phys. Rev. C **55**, number 2, 762 (2002).

[70] S. Grevy *et al.*, Nucl. Phys. A **734**, 369-373 (2004).

[71] W. Mittig *et al.*, Eur. Phys. J. A **15**, 157-160 (2002).

[72] A.C. Morton *et al.*, Phys. Lett. B **544**, 274-279 (2002).

[73] P. Baumann *et al.*, Phys. Lett. B **228**, 4, 458 (1989).

[74] S. Nummela *et al.*, Nucl. Phys. A **701**, 410-415c (2002).

[75] B.V. Pritychenko *et al.*, Phys. Rev. C **63**, 047308 (2001).

[76] B.V. Pritychenko *et al.*, Phys. Rev. C **62**, 051601 (2000).

[77] J. Enders *et al.*, Phys. Rev. C **65**, 034318 (2002).

[78] L.K. Fifield *et al.*, Nucl. Phys. A **440**, 531-542 (1985).

[79] L.K. Fifield *et al.*, Nucl. Phys. A **453**, 497-504 (1986).

[80] B. Fornal *et al.*, Phys. Rev. C **49**, number 5, 2413 (1994).

[81] H. Iwasaki *et al.*, Phys. Rev. C **67**, 064315 (2003).

[82] R.W. Ibbotson *et al.*, Phys. Rev. Lett. **80**, 2081 (1998).

[83] B. Castel and I.S. Towner 1990 Modern Theories of Nuclear Moments (Oxford Studies in Nuclear Physics) vol 12, ed P E Hodgson (Oxford: Claredon).

[84] B. A. Brown *et al.*, Ann. Rev. Nucl. Part. Sci. **38**, 29-66 (1988).

[85] F. Brandolini *et al.*, Phys. Rev. C **73**, 024313 (2006).

[86] M. Honma *et al.*, Phys. Rev. Lett. **75**, 1284 (1995).

[87] E. Matthias *et al.*, Phys. Rev. A **4**, 1626 (1971).

[88] C.P. Slichter *et al.*, 'Principles of magnetic resonance', Eds: M. Cardona and P. Fulde and H.-J. Queisser, Springer-Verslag, Berlin, Heidelberg, New York, (1980)

[89] K.S. Krane *Low Temperature Nuclear Orientation*, chapter 2 Eds: H. Postma and N.J. Stone (North-Holland), Amsterdam, (1986)

[90] N. Coulier Ph.D. thesis, IKS KULeuven 1999

[91] K. Asahi *et al.*, Phys. Lett. B **251**, 488 (1990).

[92] H. Okuno *et al.*, Phys. Lett. B **335**, 29 (1994).

[93] K. Turzo *et al.*, in progress

[94] A.S. Goldhaber *et al.*, Phys. Lett. B **53**, 306 (1974).

[95] A.Vitturi *et al.*, Phys. Rev. C **36**, 1404 (1987).

[96] J.M. Daugas *et al.*, Phys. Rev. C **63**, 064609 (2001).

[97] G.A. Souliotis *et al.*, Phys. Rev. C **46**, 1383 (1992).

[98] R. Pfaff *et al.*, Phys. Rev. C **51**, 1348 (1995).

[99] J. Moniz *et al.*, Phys. Rev. Letters **26**, 8 (1971).

[100] J. Korringa, Physica 16 (1950) 601 Phys. Rev. Letters **26**, 8 (1971).

[101] T.Minamisono *et al.*, Phys. Rev. C **14** 376 (1976)

[102] D. Bazin *et al.*, Nucl. Instr. Methods Phys. Res. A **482**, 307 (2002).

[103] www.phy.fju.edu.tw/experiment/electric/003.pdf

[104] www.ganil.fr/lise/lise2000/phys.html

[105] E.K. Warburton *et al.*, Phys. Rev. C **34**, 1031 (1986).

[106] E.K. Warburton *et al.*, Phys. Rev. C **35**, 5 1851 (1987).

[107] W. Hume-Rothery *et al.*, Structure of metals and alloys, Institute of metals (London), 1969.

[108] Y. Utsuno *et al.*, Phys. Rev. C **70**, 044307 (2004).

[109] Y. Utsuno *et al.*, Phys. Rev. C **64**, 011301 (2001).

[110] E. Caurier *et al.*, Phys. Lett. B **522**, 240-244 (2001).

[111] A. Klein *et al.*, Nucl. Phys. A **607**, 1-22 (1996).

[112] D. Rudolph *et al.*, Phys. Rev. C **65**, 034305 (2002).

[113] N. Coulier *et al.*, Phys. Rev. C **59**, 4 1935 (1999).

[114] ab initio calculations performed by V.Vanhoof using the Wien2k code

[115] R.V. Pound *et al.*, Phys. Rev. **79**, 4 685 (1950).

[116] D. Sundholm *et al.*, Phys. Rev. Letters **68**, 7 927 (1992).

Chapter 9

Nederlandstalige Samenvatting

In het dagelijks leven komen we geregeld in contact met één van de vier belangrijkste krachten in de natuur: de zwaartekracht. Ten gevolge van deze kracht valt niet alleen een appel van een boom, maar bewegen de planeten in ons zonnestelsel ook op hun karakteristieke manier. Sinds Sir Isaac Newton is er een mathematiche uitdrukking die deze aantrekking F_{12} tussen twee lichamen met massa m_1 en m_2 beschrijft:

$$F_{12} = \frac{Gm_1m_2}{r^2} \tag{9.1}$$

waarbij G de universele gravitatieconstante is. Deze formule heeft een revolutie teweeggebracht in de wereld van de mechanica en haar belang kan niet overschat worden.

Naast de zwaartekracht is de sterke kracht één van de drie andere basiskrachten. Deze kracht beschrijft de interactie tussen protonen en neutronen, dewelke de bouwstenen zijn van een kern. In tegenstelling tot de zwaartekracht, bestaat er tot op heden geen mathematische uitdrukking voor de sterke kracht. Zelfs met een correcte uitdrukking voor de interactie tussen twee nucleonen, zou men een kern nog niet kunnen beschrijven, wegens het veel-deeltjes probleem en de indicatie voor het bestaan van niet enkel interactiekrachten tussen twee maar ook tussen drie deeltjes.

Een manier om zulk een probleem te omzeilen, is te werken met modellen, zoals daar zijn "het ideale gasmodel" en "het atomair schillenmodel". Ook in nucleaire fysica wordt deze oplossingsmethode met succes gebruikt. Een schillenmodel, naar het evenbeeld van het atomaire schillenmodel, werd opgesteld in de jaren '50. Door gebruik te maken van nucleaire eigenschappen van toen reeds opgemeten kernen, kon men de nodige parameters bepalen voor dit model en zo ook andere eigenschappen van deze en andere kernen voorspellen.

Op een natuurlijke manier komen bepaalde getallen naar voren in dit schillenmodel waarvoor een bepaalde schil volledig gevuld is met protonen of neutronen (vb. 2, 8, 20, ...). Deze getallen worden magisch genoemd en zorgen voor bepaalde specifieke eigenschappen: grote separatie energie van twee neutronen, hoge excitatie energie van eerste aangeslagen niveau,...

Vele jaren heeft dit model zeer goede verklaringen en voorspellingen gedaan aangaande allerhande eigenschappen van kernen verspreid over bijna de ganse kernkaart. Meer dan een halve eeuw na de introductie van dit model wordt het nog steeds gebruikt, doch zijn er een aantal plaatsen op de kernkaart waar zich problemen voordoen [1-4]. Eén van die regio's is het zogenaamde "eiland van inversie", een neutronrijk gebied rond N = 20 en Z = 10-12 waarbij de magiciteit van het getal 20 in het gedrang komt. Ten gevolge van metingen van massa, spin, magnetische en quadrupoolmomenten, heeft men ontdekt dat kernen zoals ^{32}Mg en ^{31}Na, de magische eigenschappen verwacht voor een N = 20 kern, niet bezitten [5-10].

Aangezien voor magische getallen de schillen boven de laatstgevulde schil verschillende MeV hoger liggen, worden voor deze kernen toestanden, gedomineerd door excitaties naar deze schillen, niet verwacht op lage energie. Deze excitatietoestanden zijn de zogenaamde 'indringtoestanden'. Om de eigenschappen van laaggelegen excitatieniveaus, en zelfs de grondtoestand, van kernen rond ^{32}Mg en ^{31}Na, te verklaren, moet men deze extra schillen wel in rekening brengen. Men ziet in de schillenmodelberekeningen [11-15] dat deze indringtoestanden vaak

dominerend zijn over de normale toestanden, wat wijst op drastische reductie van de N = 20 energiekloof en dus een verlies van magiciteit van N = 20 voor deze kernen.

Zelfs 30 jaar na de eerste indicatie voor het verdwijnen van de magische schillensluiting N = 20, wordt er nog steeds intensief onderzoek verricht in dit gebied. Tot op heden is de afbakening van het eiland van inversie nog niet experimenteel bepaald. Aangezien deze grenzen, zowel in N als in Z door verschillende interacties gebaseerd op het schillenmodel en ontwikkeld door verschillende befaamde theoretische groepen, verschillend worden voorspeld, is dit onderzoek van cruciaal belang.

In dit werk wordt gepoogd de grens in protongetal te bepalen. Reeds van meerdere Mg (Z=12) kernen heeft men aangetoond dat de grondtoestand sterk beïnvloed wordt door indringtoestanden. Daarnaast zijn er ook reeds vele studies gebeurd van Si (Z=14) kernen, maar allen wijzen op een normale magische N = 20 schillensluiting voor al deze isotopen [16-24]. De indringtoestanden worden ten laagste op 1 MeV excitatie-energie verwacht. Over de Al (Z=13) kernen is er nog veel minder experimentele informatie, maar tot op heden is nog geen bewijs geleverd voor één van de Al-isotopen dat de magische schillensluiting grotendeels verdwijnt voor dit proton getal. Aan de hand van metingen van g-factoren door middel van de β-Nucleaire Magnetische Resonantie techniek (β-NMR) van verschillende Al-isotopen, wordt nagegaan of er bijmenging van de indringtoestanden aanwezig is in de grondtoestand van deze kernen. Daarnaast werd ook de g-factor van ^{35}Si opgemeten, om enerzijds eventueel nogmaals te bevestigen dat voor Z = 14 de magiciteit van N = 20 blijft bewaard. Anderzijds is deze kern van groot belang voor schillenmodelberekeningen. Aangezien de grondtoestand een bijna pure $\nu(f_{7/2})$ configuratie is (omdat de protonen de volledige $d_{5/2}$ schil vullen), krijgt men onder andere uit de excitatie-energie van de $3/2^+$ toestand (gevormd door een excitatie van $\nu(d_{3/2})$ naar $\nu(f_{7/2})$) extra informatie over de N = 20 energiegap. Om deze informatie correct te kunnen afleiden moet men onder andere weten hoe zuiver de golffunctie van de grondtoestand van ^{35}Si is.

Aangezien de g-factor een eigenschap is van een kern die zeer veel informatie levert over de laatste (ongepaarde) nucleonen van een kern, is dit de ideale eigenschap van deze kernen om op te meten en te interpreteren.

Aangezien de hoeveelheid polarisatie (= een specifieke niet-isotrope verdeling van de m-toestanden) afgebroken tijdens een β-NMR experiment, cruciaal is voor de amplitude van het β-NMR signaal en aldus de haalbaarheid van het experiment, werd veel aandacht besteed in dit werk aan productie, behoud en afbraak van polarisatie.

Een code, gebaseerd op een kinematisch model, werd in detail uitgewerkt om de productie van polarisatie in fragmentatie en pick-up reacties te beschrijven. Dit model werd exhaustief getest voor beide reactiemechanismen. Belangrijk hierbij op te merken is dat de polarisatie in een pick-up reactie het maximum bereikt in het centrum van de momentumdistributie, waarbij dit voor een projectiel-fragmentatiereactie enkel in de flank van de momentdistributie is. Daarnaast is het nog vermeldenswaardig dat de pick-up reactie gevolgd mag worden door de evaporatie van enkele nucleonen, zonder dat de hoeveelheid gecreëerde polaristie aanzienlijk daalt, waardoor zeer veel kernen op eenvoudige wijze kunnen aangemaakt en gepolariseerd worden met dit reactiemechanisme.

Naast de productie werd er ook bestudeerd hoe het behoud van de polarisatie te maximaliseren. Experimenteel heeft men bepaald dat een kubisch Si kristal goed de polarisatie van geïmplanteerde Al-isotopen behoudt en dit reeds bij een magneetveld van 0.08T.

Ten slotte werd er nog een mathematische afleiding uitgewerkt van een NMR experiment met frequentiemodulatie. Hieruit leert men dat bepaalde beperkingen optreden voor de levensduur van de opgemeten kern, het vermogen van het radio-frequente signaal en de modulatiesnelheid, opdat de polarisatie maximaal wordt afgebroken.

De meting van de g-factor van ^{31}Al, bevestigde de reeds voordien geopperde conclusie voor deze kern: er zijn geen indringtoestanden nodig om de nucleaire eigenschappen van deze kern te beschrijven.

Voor ^{32}Al was er reeds een probleem in het verklaren van de volgorde van de eerste excitatieniveaus van deze N = 19 kern. De g-factor wijkt ook lichtjes af van de verwachte "normale" waarde, waarbij men N = 20 magisch veronderstelt. Zowel de experimentele g-factor als de excitatieniveaus kunnen verklaard worden door de gebruikte schillenmodelinteractie lichtjes aan te passen, maar tevens de schillensluiting van N = 20 te behouden. Wederom is er dus geen verkleining van de energiekloof N = 20 nodig om theorie en experiment te laten overeenstemmen.

De meting van de g-factor van de grondtoestand van ^{33}Al leverde een verrassend grote afwijking ten opzichte van de theoretische, normale, waarde. Aangezien deze afwijking in de richting is van de g-factor van een pure inmengingstoestand, is dit een eerste indicatie voor een Z = 13 kern, dat opmenging met indringtoestanden zich voordoet in de grondtoestand.

In het geval van ^{34}Al is de afwijking nog groter: 0.541(1) ipv 0.376. Eveneens is het verschil in de richting van een pure inmengingstoestand. Dit wijst er op dat de grondtoestand van ^{34}Al sterk kan beïnvloed zijn door indringtoestanden. Deze meting toont aan dat Z = 13 een transitiegetal is tussen de normale, sferische kernen en het eiland van inversie. Daarnaast leert dit resultaat ons dat deze overgang niet abrupt is, maar geleidelijk.

Tenslotte werd de g-factor van ^{35}Si opgemeten. Deze waarde is in goede overeenkomst met de normale theoretische waarde, hetgeen opnieuw bevestigt dat geen Z = 14 kern sterk wordt beinvloed door indringtoestanden. Deze g-factor waarde toont aan dat de grondtoestand van ^{35}Si inderdaad een vrij zuivere $\nu(f_{7/2})$ toestand is, in tegenstelling tot andere N = 21 isotopen zoals ^{41}Ca, die worden beïnvloed door zowel proton als neutron indringtoestanden.

Naast de g-factor resultaten, zouden quadrupoolmoment metingen in deze regio van de kernkaart zeer nuttige extra informatie kunnen opleveren. Aangezien de kernen die een sterke indringcomponent bevatten, zeer vervormd zijn, kan het quadrupoolmoment van onder andere ^{33}Al en ^{34}Al een nieuwe indicatie zijn voor de geleidelijke transitie van normale naar sterk vervormde kernen bij Z = 13.

[1] P. Van Duppen *et al.*, Phys. Rev. Lett. **52**, 1974 (1984).
[2] P. Van Duppen *et al.*, Phys. Lett. **154B**, 354 (1985).
[3] E. Coenen *et al.*, Phys. Rev. Lett. **54**, 1783 (1985).
[4] J.Bron *et al.*, Nucl. Phys. A **318**, 3 335-351 (1979).
[5] M. Keim *et al.*, Hyp. Int. **97/98**, 543-550 (1995).
[6] B.V. Pritychenko *et al.*, Phys. Rev. C **63**, 011305 (2000).
[7] M. Belleguic *et al.*, Nucl. Phys. A **682**, 136-142c (2001).
[8] V. Chiste *et al.*, Phys. Lett. B **514**, 233-239 (2001).
[9] N.A. Orr *et al.*, Phys. Lett. B **258**, number 1, 29 (1991).
[10] T. Motobayashi *et al.*, Phys. Lett. B **346**, 9 (1995).
[11] E. Caurier *et al.*, Phys. Rev. C **58**, 2033 (1998).
[12] J. Retamosa *et al.*, Phys. Rev. C **5**, 1266 (1997).
[13] T. Otsuka *et al.*, Prog. Part. Nucl. Phys. **47**, 319 (2001).
[14] Y. Utsuno *et al.*, Phys. Rev. C **64**, 011301 (2001).
[15] S. Nummela *et al.*, Phys. Rev. C **63**, 044316 (2001).
[16] S. Nummela *et al.*, Nucl. Phys. A **701**, 410-415c (2002).
[17] H. Iwasaki *et al.*, Phys. Rev. C **67**, 064315 (2003).
[18] B.V. Pritychenko *et al.*, Phys. Rev. C **62**, 051601 (2000).
[19] B. Fornal *et al.*, Phys. Rev. C **49**, number 5, 2413 (1994).
[20] J. Enders *et al.*, Phys. Rev. C **65**, 034318 (2002).
[21] L.K. Fifield *et al.*, Nucl. Phys. A **453**, 497-504 (1986).
[22] R.W. Ibbotson *et al.*, Phys. Rev. Lett. **80**, 2081 (1998).
[23] S. Nummela *et al.*, Phys. Rev. C **63**, 044316 (2001).
[24] W. Mittig *et al.*, Eur. Phys. J. A **15**, 157-160 (2002).